# Experimental study and improvement of mass transfer in vertical bubble columns

Nicolas Souzy

N° d'ordre 2014-ISAL-201-2014 Année 2014

# THÈSE

**Experimental study and improvement of mass transfer in vertical bubble columns**

Présentée devant

**l'Université Claude Bernard Lyon 1**

pour obtenir

**le GRADE de DOCTEUR**

École doctorale :

**Mécanique, Énergétique, Génie Civil, Acoustique**

Spécialité :

**MÉCANIQUE des FLUIDES**

par

**Nicolas SOUZY**

**Ingénieur**

Thèse soutenue le 14 octobre 2014 devant la Commission d'examen

**Jury**

| | | |
|---|---|---|
| Anne-Marie BILLET | Professeur | Rapporteur |
| Fabrice ONOFRI | Directeur de recherche CNRS | Rapporteur |
| Romain VOLK | Maître de Conférences | Examinateur |
| Mahmoud EL HAJEM | Maître de Conférences | Examinateur |
| Michel LANCE | Professeur | Directeur de thèse |
| Jean-Yves CHAMPAGNE | Professeur | Co-directeur |

LMFA - UMR CNRS 5509 - Université Claude Bernard Lyon 1
43, boulevard du 11 Novembre 1918, 69622 Villeurbanne cedex (FRANCE)

# UNIVERSITÉ CLAUDE BERNARD - LYON 1

| | |
|---|---|
| **Président de l'Université** | M. le Professeur François-Noël GILLY |
| **Vice-président du Conseil d'Administration** | M. le Professeur Hamda BEN HADID |
| **Vice-président du Conseil des Études et de la Vie Universitaire** | M. le Professeur Philippe LALLE |
| **Vice-président du Conseil Scientifique** | M. le Professeur Germain GILLET |
| **Secrétaire Général** | M. Alain HELLEU |

# LES DIRECTEURS DES COMPOSANTES SANTÉ

| | |
|---|---|
| **Faculté de Médecine Lyon Est - Claude Bernard** | M. le Professeur J. ETIENNE |
| **Faculté de Médecine et de Maïeutique Lyon Sud - Charles Mérieux** | Mme la Professeure C. BURILLON |
| **UFR d'Odontologie** | M. le Professeur D. BOURGEOIS |
| **Institut des Sciences Pharmaceutiques et Biologiques** | Mme la Professeure C. VINCIGUERRA |
| **Institut des Sciences et Techniques de la Réadaptation** | M. le Professeur Y. MATILLON |
| **Département de formation et Centre de Recherche en Biologie Humaine** | Mme. la Professeure A-M. SCHOTT |

# LES DIRECTEURS DES COMPOSANTES ET DEPARTEMENTS DE SCIENCES ET TECHNOLOGIE

| | |
|---|---|
| **Faculté des Sciences et Technologies** | M. F. De MARCHI |
| **Département Biologie** | M. le Professeur F. FLEURY |
| **Département Chimie Biochimie** | Mme C. FELIX |
| **Département GEP** | M. H. HAMMOURI |
| **Département Informatique** | M. le Professeur S. AKKOUCHE |
| **Département Mathématiques** | M. G. TOMANOV |
| **Département Mécanique** | M. le Professeur H. BEN HADID |
| **Département Physique** | M. J.-C. PLENET |
| **UFR Sciences et Techniques des Activités Physiques et Sportives** | M. Y.VANPOULLE |
| **Observatoire de Lyon** | M. B. GUIDERDONI |
| **Polytech Lyon** | M. P. FOURNIER |
| **Ecole Supérieure de Chimie Physique Electronique** | M. G. PIGNAULT |
| **Institut Universitaire de Technologie de Lyon 1** | M. C. VITON |
| **Institut Universitaire de Formation des Maîtres** | M. A. MOUGNIOTTE |
| **Institut de Science Financière et d'Assurances** | M. N. LEBOISNE |

# Acknowledgements

The experimental work presented in this Ph.D. thesis has been carried out in the Laboratoire de Mecanique des Fluides et d'Acoustique (LMFA) of Lyon directed by Michel Lance, professor at University Claude-Bernard Lyon 1. I would like to express my gratitude to all those who gave me the possibility to complete this thesis in this laboratory. I want to thank my supervisors Michel Lance, Jean-Yves Champagne for their support and kindness. My gratitude goes to Mahmoud El Hajem for his useful comments which helped to organise and enrich the issues addressed in this thesis. I am deeply indebted to Pierre Valiorgue whose help and stimulating suggestions guided me during the first part of this work.

I thank the reviewers: Anne-Marie Billet, professor at the École nationale supérieure des ingénieurs en arts chimiques et technologiques (ENCIASET) of Toulouse, and Fabrice Onofri, directeur de recherche CNRS at the Institut Universitaire des Systèmes Thermiques Industriel (IUSTI) of Aix-Marseille, for the interest they have shown in my work. I am also grateful to Dr Romain Volk of the Ecole Normale Superieure (ENS) of Lyon, who agreed to be member of the jury.

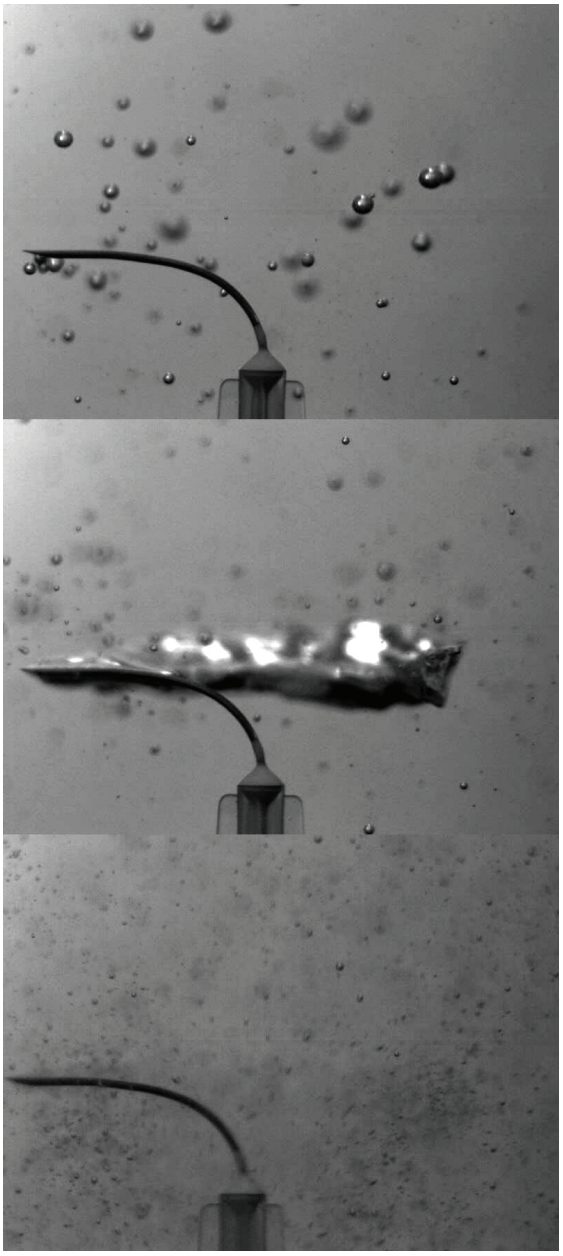

# Abstract

## Résumé long

Les colonnes à bulles sont utilisées depuis longtemps en minéralurgie et en traitement des eaux pour capturer différents types de particules. Plus récemment, c'est leur capacité d'échange qui a été utilisée pour produire des réactions chimiques entre phase gazeuse et phase liquide. La colonne à bulles à dépression étudiée lors de cette thèse de doctorat permet de dissoudre du dioxyde de carbone dans de l'eau. Cette eau riche en carbone constitue un milieu idéal pour la culture de micro-algues. La production de ces micro-algues est aujourd'hui un enjeu dans de multiples domaines puisqu'elles peuvent être destinées à un usage médicinal, alimentaire, ou encore énergétique sous forme de bio-carburant. Il est donc important de comprendre les phénomènes et paramètres en jeu avant de réaliser une augmentation d'échelle.

Ce manuscrit de thèse est composé de cinq chapitres regroupés en 3 parties traitant successivement des colonnes à bulles, des Générateurs de Micro-Bulles, puis de la Fluorescence Induite par Plan Laser.

Dans le **premier chapitre**, après une introduction sur les principales fonctions et applications des colonnes à bulles, les lois physiques du transfert de masse et de la contamination ont été abordées d'un point de vue théorique. Les limites de l'étude sont définies à la fin du chapitre.

Le **chapitre 2** présente la colonne à bulles à dépression du LMFA ainsi que les résultats obtenus antérieurement. Lors de cette thèse, une expérience de désaturation a été menée pour quantifier l'amélioration des échanges gaz-liquide lorsque la colonne est en fonctionnement. Le circuit de gaz de la colonne a été modifié pour réaliser une étude en boucle fermée, comparable au fonctionnement d'un ensemble de colonnes montées en série. Un modèle théorique associé à cette configuration a été implémenté et met en évidence l'importance de l'aire interfaciale gaz-liquide lors du transfert de masse dans les colonnes à bulles. Ainsi, l'échange moléculaire entre un volume donné de dioxyde de carbone et l'eau peut être amélioré par la formation de bulles plus petites, menant à une plus grande interface gaz-liquide.

C'est l'objet de la deuxième partie. Le **chapitre 3** présente les divers phénomènes physiques s'appliquant aux bulles, ainsi que les nombres adimensionnels associés. Un État de l'Art des Générateurs de Micro-Bulles (MBG) est ensuite exposé, présentant des systèmes utilisant divers phénomènes tels que la cavitation, l'électrolyse, ou le cisaillement.

Un nouveau Générateur de Micro-Bulles a été conçu et caractérisé. Ce diffuseur de micro-bulles rotatif est capable de produire un nuage de bulles dont les diamètres peuvent être modifiés via une vitesse de rotation conrôlée par potentiomètre électrique. Le débit de gaz est indépendant de la vitesse de rotation, et un débit d'eau n'est pas requis pour le fonctionnement du système. Les travaux expérimentaux associés sont présentés dans le **chapitre 4**, et attestent que le prototype est capable de produire des micro-bulles ayant un diamètre moyen $D_{bubble} = 0.252\ mm$. Ces résultats prometteurs nous ont encouragés à faire une déclaration officielle avant dépôt de brevet. L'installation d'un tel dispositif dans les colonnes à bulles devrait conduire à une augmentation significative de l'aire interfaciale gaz-liquide, et donc du transfert de masse.

Enfin, la troisième partie de cette thèse traite de la Fluorescence Induite par Plan Laser (PLIF), une technique optique non intrusive permettant d'obtenir expérimentalement des coefficients de transfert de masse $k_l$. Afin d'obtenir une meilleur précision lors de la mesure de champs de scalaires, deux traitements d'image de PLIF prenant en compte les variations de l'extinction de la fluorescence due au pH ont été développés dans le **chapitre 5**. Le premier traitement a lieu durant la calibration. Il est montré que la méthode proposée doit être appliquée lorsque le produit de la variation du coefficient d'extinction, de la longueur du chemin parcouru par le laser et de la concentration du fluorophore devient grand, comme par exemple pour les expériences dans de grands réservoirs. L'influence des variations du coefficient d'extinction a été évaluée sur une mesure de concentration de $CO_2$ lors d'un cas test dans le sillage d'une bulle en ascension libre dans une colonne d'eau. Le second traitement d'image concerne les cas où le gradient scalaire s'étend sur une large zone. Quand la distance de la région de mesure où les variations de pH sont observées augmente, les variations du coefficient d'extinction vont affecter localement l'intensité de la lumière incidente, et donc les mesures. Ces variations sont dues à la dépendence du coefficient d'extinction vis-à-vis du pH. Une correction du traitement d'image prenant en compte les variations de l'atténuation de la lumière incidente a été proposée. La nécessité de cette correction a été illustrée par un cas test dans le sillage d'un nuage de bulles en ascension libre dans une colonne d'eau.

# Résumé court (<1700 caractères)

Les colonnes à bulles sont utilisées en minéralurgie et en traitement des eaux pour capturer différents types de particules. Leur capacité d'échange bénéficie aujourd'hui d'un regain d'intérêt pour assurer la production de micro-algues destinées à un usage médicinal, alimentaire, ou énergétique : les concentrations d'oxygène et de dioxyde de carbone peuvent être contrôlées grâce à la considérable aire interfaciale gaz-liquide dans la colonne à bulles. Une étude expérimentale en boucle fermée a été menée pour simuler le passage du gaz dans une succession de colonnes en série. Le modèle théorique associé confirme le rôle critique du diamètre des bulles lors du transfert de masse. Un générateur de micro-bulles (MBG) innovant a été conçu et testé. Le prototype est capable de produire des micro-bulles d'un diamètre moyen $D_{bubble} = 0.252\ mm$. L'invention a été officiellement déclarée. Le dernier chapitre a pour objet l'amélioration des méthodes de traitement de Fluorescence Induite par Plan Laser (PLIF), qui permettent d'obtenir les coefficients de transfert de masse $k_l$. La première correction présentée prend en compte les variations de l'extinction de la fluorescence due au pH pendant la calibration et a été évaluée sur une mesure de concentration de $CO_2$ dans le sillage d'une bulle en ascension libre dans une colonne d'eau. La seconde correction proposée doit être appliquée quand la distance de la région de mesure où les variations de pH sont observées augmente. La nécessité de cette correction a été illustrée par un cas test dans le sillage d'un nuage de bulles en ascension libre dans une colonne d'eau.

**MOTS-CLEFS:** Colonne à bulles verticale, aire interfaciale gaz-liquide, générateur de micro-bulles, transfert de masse de $CO_2$, correction de traitement d'image, PLIF.

# Short abstract (<1700 characters)

Bubble column are involved in many industrial fields ranging from chemical industry to mineral processing. It recently became an industrial stake for the production of micro-algae intended for medicinal use, food or energy: the oxygen and carbon dioxide concentrations can be controlled via the efficient mass transfer induced by the significant gas-liquid interfaciale area into the bubble column. Firstly, experimental closed-loop study has been carried out to simulate the passage of gas in a succession of columns in series. The associated theoretical model confirms the critical importance of the bubble diameter for mass transfer. Therefore, an innovative Micro-Bubble Generator (MBG) has been designed and tested. The prototype is able to produce micro-bubbles of average diameter $D_{bubble} = 0.252\ mm$. The invention has been officially declared. The last chapter aims at improving data treatment methods for Planar Laser-Induced Fluorescence (PLIF), which enables to obtain experimentally mass transfer coefficient $k_l$ through concentration measurements. The first presented correction takes into account variations of the fluorescence extinction due to pH during the calibration step, and has been evaluated on $CO_2$ concentration measurement in the wake of a free rising bubble. The second proposed correction should be applied when the length in the measurement region over which pH variations are observed increases: variations of the extinction coefficient will affect the local incident light intensity and therefore the measurements. The need for this correction has been illustrated on a test case in the wake of a cloud of free rising bubbles.

**KEYWORDS:** Vertical bubble column, gas-liquid interfacial area, Micro Bubble Generator, $CO_2$ mass transfer, data treatment correction, PLIF.

# Contents

# List of Figures

# List of Tables

# Part I

# Bubble columns

# Chapter 1

# State of the art

*Les colonnes à bulles sont utilisées depuis longtemps en minéralurgie et en traitement des eaux pour capturer différents types de particules. Plus récemment, c'est leur capacité d'échange qui a été utilisée pour produire des réactions chimiques entre phase gazeuse et phase liquide. La colonne à bulles à dépression étudiée lors de cette thèse permet de dissoudre du dioxyde de carbone dans de l'eau. Cette eau riche en carbone constitue un milieu idéal pour la culture de micro-algues. La production de ces micro-algues est aujourd'hui un enjeu dans de multiples domaines puisqu'elles peuvent être destinées à un usage médicinal, alimentaire, ou encore énergétique sous forme de bio-carburant. Il est donc important de comprendre les phénomènes et paramètres en jeu avant de réaliser une augmentation d'échelle. Après une introduction sur les principales fonctions et applications des colonnes à bulles, les lois physiques du transfert de masse et de la contamination sont abordées d'un point de vue théorique. Les limites de l'étude sont définies à la fin de ce chapitre.*

# Abstract

Bubble columns have been used for decades in mineral processing and water treatment to capture different types of particles. More recently, their exchange capacity has been used for producing chemical reactions between gas phase and liquid phase. The vacuum bubble column studied in this thesis can dissolve carbon dioxide in water. This carbon enriched water is an ideal culture medium for producing micro-algae. These micro-algae are a source of raw materials for multiple fields since they may be intended for medicinal use, food, or energy in the form of biofuel. Thus it is important to understand the phenomena and parameters involved before scale up. After an introduction to the main features and applications of bubble columns, the physical mass transfer and contamination are discussed from a theoretical point of view. The limitations of the study are defined at the end of this chapter.

# Nomenclature

### Latin symbols

| | |
|---|---|
| $a$ | Gas-liquid interfacial area per unit volume, $[\frac{\mathrm{m}^2}{\mathrm{m}^3}]$ |
| $A_i$ | Gas-liquid interfacial area, $[m^2]$ |
| $C$ | Concentration, $[\frac{\mathrm{mol}}{\mathrm{m}^3}]$ |
| $\overline{c}$ | Average concentration, $[\frac{\mathrm{mol}}{\mathrm{m}^3}]$ |
| $c'$ | Fluctuation part of the concentration, $[\frac{\mathrm{mol}}{\mathrm{m}^3}]$ |
| $D$ | Diffusion coefficient, $[\frac{\mathrm{m}^2}{\mathrm{s}}]$ |
| $j$ | Diffusion flux, $[\frac{\mathrm{mol}}{\mathrm{m}^2.\mathrm{s}}]$ |
| $H_c$ | Henry constant, $[\frac{L.Pa}{mol}]$ |
| $k_l$ | Mass transfer coefficient, $[\frac{\mathrm{m}}{\mathrm{s}}]$ |
| $N$ | Amount of substance, $[mol]$ |
| $P$ | Pressure, $[Pa]$ |
| $p$ | Partial pressure of the gas in the gas phase, $[Pa]$ |
| $P_T$ | Total pressure in the medium, $[Pa]$ |
| $R_g$ | Gas constant, $[\frac{\mathrm{J}}{\mathrm{K}\cdot mol}]$ |
| $T$ | Absolute temperature, $[K]$ |
| $U$ | Velocity, $[\frac{\mathrm{m}}{\mathrm{s}}]$ |
| $\overline{u}$ | Average velocity, $[\frac{\mathrm{m}}{\mathrm{s}}]$ |
| $u'$ | Fluctuating part of the velocity, $[\frac{\mathrm{m}}{\mathrm{s}}]$ |
| $V$ | Velocity, $[\frac{\mathrm{m}}{\mathrm{s}}]$ |
| $\overline{v}$ | Average velocity, $[\frac{\mathrm{m}}{\mathrm{s}}]$ |
| $v'$ | Fluctuating part of the velocity, $[\frac{\mathrm{m}}{\mathrm{s}}]$ |

| | |
|---|---|
| $W$ | Velocity, $[\frac{\mathrm{m}}{\mathrm{s}}]$ |
| $\overline{w}$ | Average velocity, $[\frac{\mathrm{m}}{\mathrm{s}}]$ |
| $w'$ | Fluctuating part of the velocity, $[\frac{\mathrm{m}}{\mathrm{s}}]$ |
| $x$ | Molar fraction in the gas phase, [ ] |

**Subscripts**

| | |
|---|---|
| $sat$ | Saturation of the concentration. |

## 1.1 Some applications

The injection of gas bubbles within a column of liquid has various applications. Buoyancy creates a movement of the liquid due to bubbles rising. These installations took the name of "Airlift" and the first publications about this process appeared in the early 20th century [24].

Pumping water using air bubbles was quickly exploited, especially to create a flow in a liquid highly charged in particles (for archaeological excavations or in the case of water treatment plant). The method found new applications in industry in the late 20th century in aquaculture production and development of micro-algae (see Section 1.1.3).

The airlift (see Section 1.2) is a multi-function system that is able to achieve simultaneously:
- the mass transfer, i.e. the transfer of elements from the liquid phase to the gas phase and vice versa. The transfer from the gas to liquid phase is called absorption, while the extraction of gas out of the liquid is called stripping ;
- the function of pumping the liquid which is driven in the column by the gas bubbles ;
- the carrying to the surface of the particles suspended in the water and captured by the rising gas bubbles, which enables skimming [17, 30].

Each function depends on some parameters that will increase or decrease their effectiveness, such as the gas flow, the type of injection, the column geometry, etc. Their influence is discussed in Section (2.1.3).

### 1.1.1 Flotation

One of the first applications of bubble columns was the mineral flotation process. This technology consists in selectively separating hydrophobic materials from hydrophilic. After crushing and grinding rocks, the mineral is mixed with water to form a pulp. The mineral selectivity is done by adding specific surfactants to the pulp, modifying the chemical properties of the desired mineral. The bath contain-

ing the pulp is then aerated. Generated bubbles capture hydrophobic materials while rising to the surface, forming a froth. The froth is highly concentrated and removed regularly for further refining if necessary.

While first mines were relatively rich in minerals, it is now necessary to extract and refine huge volumes of rocks to supply the modern world's needs in valuable minerals. Increasing rareness and demand forced the extraction of more complex minerals requiring flotation process advancement.

The flotation process is able to treat small products (1 to 10 $\mu m$) as well as particles up to 500 $\mu m$ [12]. It is based on the superficial properties of particles like wetting. Flotation is a 3 phase system: solid-liquid-air. The physical and chemical properties of the particles and the capture mechanism are linked to the noteworthy properties of water.

A water molecule is an isosceles triangle with an angle of 104.45° at the oxygen atom. The electro-negativity of the oxygen atom combined with the electro-positivity of the 2 hydrogen atoms creates a permanent dipole momentum of 1.83 *Debyes*. The polarity attracting other molecules may form 1 to 4 electrical bonds called hydrogen bonds. This explains many of the properties of water, such as solvent action, cohesion, surface tension and adhesion. Under standard temperature and pressure, water molecules are grouped in tetrahedral structures.

When a solid is immersed in water, the ionized molecules of water are attracted by the atoms, molecules or ions present on the surface of the crystal lattice.

In chemical reactions, water can act as either an acid or a base by decomposition:

$$\begin{cases} H_2O = H^+ + OH^- \\ H_3O^+ = H^+ + H_2O \end{cases} \tag{1.1}$$

The study of the hydrophilic characteristics of a material can be done by measuring experimentally the value of the contact angle between the separating surfaces of solid-liquid or solid-gas: a high wetting between water and a solid will result in an angle close to 0, whereas an air bubble bonded to an immersed wall will have a high-value contact angle. One can add collector agents that will increase capture during the flotation process, by covering the target particles with a wettable film (i.e. hydrophilic). For very thin particles, the probability of collision and adhesion to a rising bubble is low. On the other hand, bigger particles may encounter bubbles more often, but the friction forces can become higher than the adhesion forces. Therefore, particles with extremely high or low size will result in poor yield [12].

The flotation process is efficient if one can select the particle captured. Selectivity can be increased by knowing the nature of the particle and understanding

its behaviour along with rising bubbles. A flotation machine has to fill these conditions:
-absorption of collector agents (in case particles are not hydrophobic) ;
-continued suspension of particles in the liquid ;
-homogeneous dispersion of the bubbles and the agents ;
-particle adhesion to air bubbles ;
-rise of the bubbles after capture ;
-form a foam on the surface that should be a quiet area.

The foam is regularly collected from the quiet area and decanted to separate water from the particles. The flotation process can be used for the decontamination of organic pollutants in fish farming, or to harvest micro-algae (1.1.3).

Bubble columns have been used for decades for flotation process in the mineral industry. New applications are now studied: bubble columns can help to solve modern problems like the greenhouse effect by accelerating $CO_2$ sequestration.

### 1.1.2 $CO_2$ sequestration

Carbon dioxide exists in Earth's atmosphere as a trace gas. As a greenhouse gas, it absorbs and emits radiations contributing to the increase in the average earth surface temperature.

The burning of fossil fuels since the Industrial Revolution (1750) has contributed to an increase in the atmospheric concentration of carbon dioxide of 40%. The laboratory of Mauna Loa observed for first time (in 55 years of measurements) a $CO_2$ concentration reaching 400 parts per million (i.e. 0.04%) in May 2013 [23].

The increase of $CO_2$ since 1850 has been reviewed and analysed by Knorr [20]. Variations in atmospheric $CO_2$ concentration on different time-scales can be observed on GRID-Arendal website [19]. It is currently assumed that $CO_2$ is a key factor in the anthropogenic global warming. To avoid dramatic climate change, ecological movements have been encouraged to control carbon dioxide emissions [38, 35].

The carbon cycle is naturally regulated by biological sequestrations of various types, like photosynthesis or ocean acidification. To enhance carbon sequestration, it is possible to store it in underground reservoirs. The first large-scale Carbon Capture and Storage (CCS) project was operative in 1996 on a Statoil-Hydro offshore plant of Sleipner, in Norway. The dissolution of carbon dioxide in deep water is a solution to $CO_2$ sequestration. But while it is a natural source of ocean acidification, the injection of large quantities in deep sea may alter marine ecosystem equilibrium. Indeed dissolution of carbon dioxide in water results in carbonic acid, as given in Equation (1.2):

$$\begin{cases} CO_2 + H_2O = H_2CO_3 \\ H_2CO_3 = HCO_3^- + H^+ \\ HCO_3^- = CO_3^{2-} + H^+ \end{cases} \tag{1.2}$$

Geo-engineering techniques like iron fertilization and urea fertilization in oceans encourage phytoplankton growth, which also participates in removing carbon from the atmosphere [3, 29]. The reforestation and protection of peat bogs provides natural carbon storage.

Biofuels contain energy from geologically recent carbon fixation. As reported in [34], one can consider 3 generations of biofuels:
-sugar, starch, or vegetable oil. They can be used directly after easy transformations ;
-lignocellulosic biomass or woody crops, agricultural residues or waste produced from sustainable feedstock. They are harder to extract but have better rates and are more environmentally friendly ;
-algal fuels photobioreactors (or PBR). They are not yet profitable.

In addition, if the biomass growth fixes carbon that has been captured before (e.g. micro-algae fixing captured carbon dissolved in water), it results in $CO_2$ sequestration. Increasing the concentration of $CO_2$ in the water enables optimized development of micro-algae in photobioreactors by photosynthesis. In 2011, Zimmerman et al. [40] observed that "daily $CO_2$ uptake clearly is correlated directly with the average daily light intensity".

Ultimately, bio-energy with carbon capture and storage (BECCS) has the ability to result in negative emissions of $CO_2$.

Micro-algae are one of the most studied alternatives to petroleum. This microscopic organism can be found in fungi, slime or lichens. It is attracting more and more scientists and entrepreneurs who seek alternative products that don't compete with agricultural land and food production.

### 1.1.3 Micro-algae

A modern application for bubble columns is the culture of micro-algae for the production of bio-fuels. Indeed, bio-fuels are one of the most promising ways to replace fossil fuels.

Micro-algae are rich in sugars, pigments, vitamins, fats, proteins and antioxidants. They can be used as food in fish-farming, as well as medicine like spiruline [32]. As bio-fuel, they offer excellent performance compared to terrestrial plants. They produce about 10 times more liters of oil per hectare than palm [6], having an oil content up to 80% of their dry biomass. In addition, micro-algae do not require fertile floor space, and are generally fast growing.

Economic and environmental interests are numerous: the $CO_2$ from industrial production is valued as consumed by algae, which when mature can almost directly be used as fuel. Once profitable, large scale production could be considered, without massive deforestation or competition with food crops.

In [6], Chisti estimates the price of algal-oil at \$2.80/L, which has to be compared to "the average price of petrodiesel in 2006 [that] was \$0.49/L with a 73% contribution from crude oil and 27% contribution from refining".

The application of the bubble columns is of great interest in the production of micro-algae. Coupled with a meandering pool "raceway", it provides three functions necessary for the development and harvesting of micro-algae: water flow, mass transfer and harvesting [2].

Figure 1.1: Horizontal pipe photobioreactor.

Open reactors (e.g. raceway ponds) are the easiest way to obtain quickly large amounts of micro-algae for biofuel production, but growth conditions cannot be controlled precisely, limiting the number of species to the most resistant and those with the highest growth rates. Closed systems (see Figure 1.1) have then been adopted by companies like Microphyt [25, 26]. They allow better control of the culture conditions and avoid external contaminations [40].

Nowadays, however, levels of productivity are generally low compared to the high cost operation of the facilities. Serious performance problems still have to

be solved [11, 22]. In [6], producing a kilogram of microalgal biomass has been estimated at $2.95 for photobioreactors and $3.80 for raceways.

A review of the various designs of enclosed photobioreactors and open systems has been written by Kunjapur and Eldridge [21]. For optimal configuration, the authors propose a combination of open and closed systems. A hybrid solution is presented in this document, in Section (2.3). The vacuum bubble column has been partially closed, i.e. the gas circuit is in a closed loop while the water tank is still in contact with the atmosphere. The re-injection of gas prevents harmful gas emissions into the atmosphere, and maximizes the speed of growth of algae by injecting more carbon in the column (2.3.2).

In 2008, a vertical vacuum bubble column has been patented by INSAVALOR and IFREMER [18]. It is now developed by COLDEP company [7], in collaboration with LMFA and IFREMER, in order to create a system of waste water treatment and a solution for production and concentration of biomass from marine micro-algae. IFREMER worked also with the ARDA (Association Réunionnaise de Développement de l'Aquaculture, i.e. Association of the Aquaculture Development of Reunion) to develop experimental fish farms using a bubble column for the recirculation [2].

Collaborations established with LMFA (Laboratoire de Mécanique des Fluides et Acoustique, i.e. Laboratory of Fluid Mechanics and Acoustic) on this project aimed at enhancing the knowledge of bubble columns and simulate specific cases of functionality on the column installed in the laboratory [28]. During this thesis, experiments have been performed in order to improve the characterization of this type of column.

The singularity is that the water column is created by a depression at the top of the bubble column instead of an over-pressure at the bottom. This vacuum column was first focused on aquaculture production and development in closed aqueous medium (for example micro-algae or fish). It is a multifunctional system able to achieve simultaneously:
- the material transport, that is to say the function of pumping liquid from a pool of algae cultivation, which is driven in the column by the gas bubbles ;
- the mass transfer, i.e. the transfer of elements from the liquid phase to the gas phase and vice versa. In the case of algae production or fish farming, mass transfer is used to control the rate of oxygen and carbon dioxyde in the water ;
- the carrying to the surface of the particles suspended in the water and captured by the rising gas bubbles [17, 30]. In algae production ; it enables harvesting through skimming. In fish farming, it enables skimming of organic waste carried to the top of the column.

As discussed previously (1.1.3), micro-algae could be used as a biofuel, provided that scale-up production becomes possible. Various solutions have been

designed to accelerate the cultivation of micro-algae, such as the development of recirculation systems using bubble columns as pictured in Figure (1.2).

Figure 1.2: A bubble column linked to a raceway for micro-algae culture.

## 1.2 Airlift and bubble column flow regimes

An airlift column, involves a two-phase flow, i.e. a transport phenomenon and exchange between the liquid phase and the gas phase (e.g. gas bubbles). Minimally, it is modelled as a column in which a wall is introduced to drive the flow of liquid and gas phases as in Figure (1.3). A gas injection system is in one of the compartments. Gas injection enables modification of the apparent density and expansion of the diphasic fluid, causing the flow of the liquid phase that was initially stationary. An airlift system is schematically divided into four compartments (see Figure 1.3):
- Compartment 1: ventilated area where fluids move in an upward motion ;
- Compartment 2: change of flow direction over the first compartment, liquid descends to compartment 3 as a portion of the gas escapes through the top of the column ;
- Compartment 3: generally unventilated portion where the liquid phase moves in a downward motion. Gas bubbles transported by the movement of the liquid can be found in this compartment. They can hinder downward flow circulation by trying to go to the top of column. In certain conditions, this phenomenon can lead to a backward flow airlift ;

- Compartment 4: change of direction of the liquid, back to the first compartment, or discharged into an external system (e.g. algae pool).

Compartments 1 and 3 are the expected locations of airlift functions. Gas flow is generally injected between compartments 1 and 4, and compartment 2 can be built for the collection of particles.

The hydraulic operation of the airlift is dependent on key criteria such as the geometry of the column, the type of the diffuser and the nature of the fluids. The choice of these parameters dictates the flow regime as well as the functional efficiencies of the system. Their influence is presented in Chapter 2.1.3.

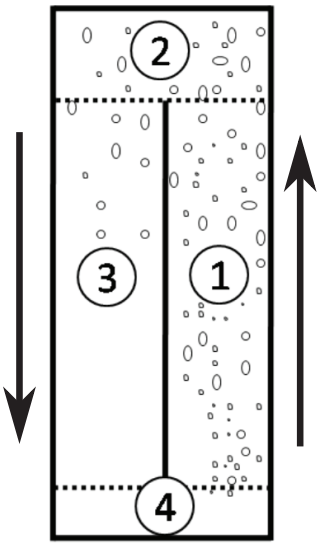


Figure 1.3: Airlift compartments.

In two-phase systems, different flow regimes can be established, depending on the form of bubbles and flow conditions of gas and liquid phases. The main schemes are presented in Figure 1.4. For vertical columns, one can distinguish:
- bubbly flow, often regarded as a uniform flow. For low liquid and gas flow rates, it corresponds to gas bubbles dispersed in the continuous liquid phase. In the case of very high liquid flow rates, the flow becomes a finely dispersed bubble flow in which the turbulence of the liquid phase results in a dispersion of the gas phase and in homogeneous fine spherical bubbles ;
-the intermittent flow (or heterogeneous flow), for which the gas bubbles get closer to each other, creating collisions and coalescence of bubbles. It creates a succession of pockets of gas and liquid phase plugs called slug flow. By further increasing the gas velocity, the gas pockets are increasingly large but easy to deconstruct.

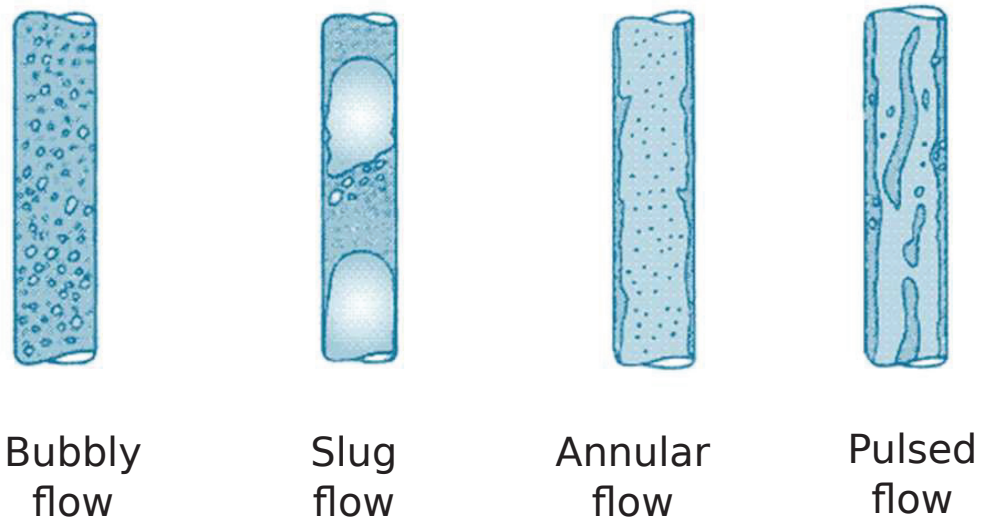


Figure 1.4: Flow regimes in a vertical column.

This leads to a chaotic flow regime, called churn flow in Taitel [33] ;
-the ring-type separated phase flow (or annular flow), which is characterized by a continuous flow of gas, while the liquid forms a homogeneous film on the wall. This regime corresponds to high gas velocities ;
-the dispersed annular flow (or pulsed flow), which also corresponds to a flow of dispersed phases but for a gas velocity so high that it locally tears off the parietal liquid film, forming a dispersion of droplets in a highly turbulent gas stream.

## 1.3 Physics of mass transfer in bubble columns

In order to properly characterize the gas-liquid mass transfer one must know:
- the conditions of equilibrium between phases (depending on the solute, the existing phases, and the conditions of pressure and temperature) ;
- the local conditions of turbulence ;
- the local conditions of contamination ;
- the distribution of the bubble size and the gas fraction in the column (depending on the mode of injection of the gas bubbles and flow) that will affect the value of the interfacial area.

Since mass transfer is based on the coexistence of two phases, it is necessary to establish the equilibrium conditions. Henry's law determines the thermodynamic equilibrium of a diphasic system. The concentration $C$ $(mol/m^3)$ of dissolved gas in the liquid phase is proportional to the partial pressure $p$ $(Pa)$ of the gas in the

gas phase :

$$p = Hc \times C \tag{1.3}$$

where $H_c$ $(L.Pa/mol)$ is the Henry constant depending on the solute, the solvent and the temperature.

Assuming that the gases do not react with each other, Dalton's law enables to compute the partial pressure p of a solute in the gas phase:

$$p = P_T \times x \tag{1.4}$$

where x is its molar fraction in the gas phase, and $P_T$ $(Pa)$ the total pressure in the medium.

Once this state of equilibrium is defined, one must characterize the actual state, and thus the deviation from the equilibrium. The model considering a double film, based on Fick's law is a rather simple model, where the transfer flow per unit of exchange area is proportional to the concentration gradient of the solute:

$$j = -D\nabla C \tag{1.5}$$

where $j$ $(mol/(m^2 \cdot s))$ is the "diffusion flux", measuring the amount of substance that will flow through a small area during a small time interval, $D$ $(m^2/s)$ is the diffusion coefficient or diffusivity and $C$ $(mol/m^3)$ (for ideal mixtures) is the concentration. The negative sign in front of equation (1.5) indicates that the flow of solute transport goes from the highest concentrations to the lowest.

Taking into account the conservation of mass and the Reynolds decomposition leads to:

$$\begin{cases} U = \overline{u} + u' \\ V = \overline{v} + v' \\ W = \overline{w} + w' \\ C = \overline{c} + c' \end{cases}$$

where $\overline{u}$, $\overline{v}$ and $\overline{w}$ are the time average velocities $(m/s)$, and $u'$, $v'$ and $w'$ are the fluctuating parts. $\overline{c}$ is the average concentration and $c'$ $(mol/m^3)$ is the fluctuation of the concentration.

Assuming that the process is horizontally homogeneous as in stratified flows, the differential equation of the global gas flow can be written as:

$$j = -D\frac{\delta \overline{c}}{\delta z} + \overline{c'w'} \tag{1.6}$$

where $z$ indicates the vertical direction. The first term on the right determines the process of molecular diffusion, and the second term, the mass transport in

the turbulent vertical direction. The term of mass transfer turbulence $c'w'$ is the correlation term that combines the information from the fluctuation rate of turbulence and concentration.

The local molecular mass gas flux $j$ through the interface can also be expressed as follows:

$$j = k_l \times (C_{sat} - C) = k_l \times (p/H_C) \tag{1.7}$$

where $k_l$ $(m/s)$is the liquid side mass transfer coefficient, $C$ is the local molar concentration in the bulk of the fluid, and $C_{sat}$ is the saturation concentration which is evaluated using the Henry constant $H_c$ and the partial pressure $p$.

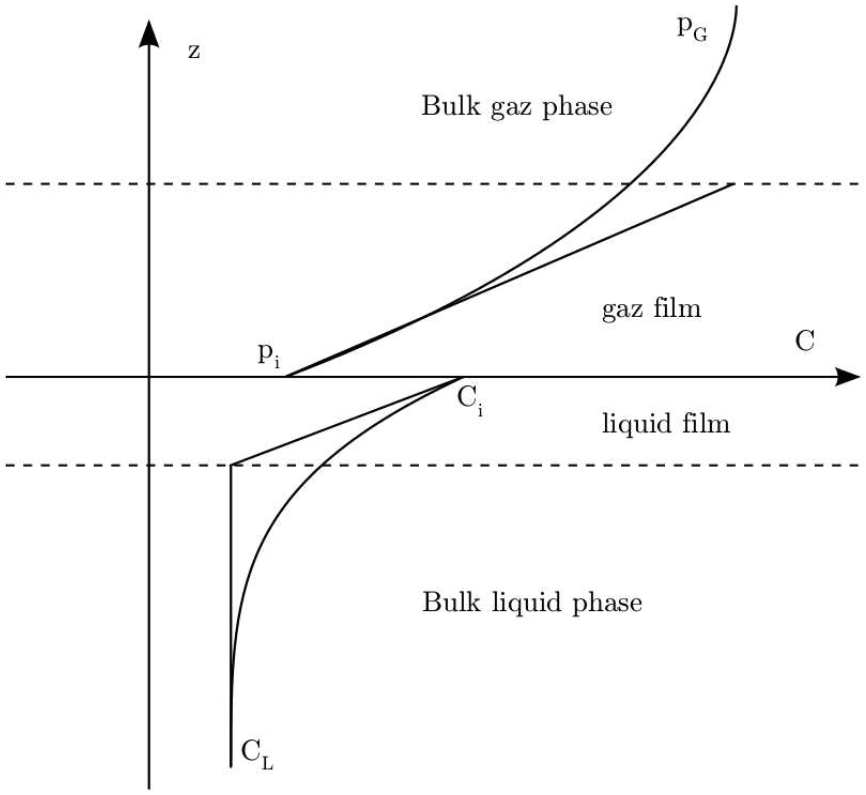


Figure 1.5: Representation of mass transfer using gas-liquid film theory.

In order to take into account the interfacial area, the volumetric mass transfer coefficient $k_l a$ is usually evaluated. The $k_l a$ $(/s)$ is the product of the liquid side mass transfer coefficient $k_l$ with the specific interfacial area per unit volume $a$ $(m^2/m^3)$.

$$k_l a = k_l \times a \tag{1.8}$$

For our work, the pressure $P_T$ at gas-liquid interface in the medium is considered constant, but its variations with the level of water could be taken into account for more precision. $C$ and $C_{sat}$ are assumed to be equivalent to the average value for each experiment. Finally, the $k_l$ of the solutes are considered independent of each other.

In addition, the following relationship is the expression of the molecular loss rate:

$$\frac{dn}{dt} = -A_i \times j = -A_i \times k_l \times (C_{sat} - C) \tag{1.9}$$

where $A_i$ describes the exchange interface. The negative sign corresponds to the decrease of the molar amount of gas in the bubble. This quantity can be expressed by the ideal gas law:

$$P \times V = n \times R_g \times T \tag{1.10}$$

where $V$ is the volume of gas ($m^3$), $N$ is the amount of substance ($mol$), $R_g$ is the gas constant (8.314 $J.K^{-1}mol^{-1}$), $P$ is the pressure ($Pa$), $T$ is the absolute temperature ($K$).

Increasing the gas flow and decreasing the size of the bubbles leads to an increase in the gas hold-up and the coefficient $k_la$, by increased turbulence and surface of exchange. The calculation of the exchange coefficient $k_la$ is possible, but mainly depends on the system configuration, as shown by Hebrard and Roustan in [15]. An extensive review of the different techniques for mass transfer determination is presented in Vasoncelos *et al* [37].

As pointed out by Valiorgue [36], not considering either duration of transfer, or evolution of concentration, or variations of the interfacial area does not allow for fine predictions of mass transfer. It is possible to take into account variations due to surfactants that can contaminate the gas-liquid interface.

## 1.4 Boundary layer and contamination of the interface

The liquid mass transfer depends on the contamination of the interface. In reality, most of the fluids are contaminated by impurities, particles, or surfactants [17]. Thus the surface of the bubble is contaminated, and the movements are stopped by those particles [8, 10]. In [4], Brumley and Jirka show that the use of tap water can create a contaminated surface.

In addition to the complex interactions between molecular diffusion and turbulent transport, one must consider organic films or microfilm from floating particles. When a gas-liquid interface is covered by an element that does not transfer

to the other phase (i.e. organic or chemical surfactants), greater shear stress is created and therefore it decreases the turbulent fluctuations (i.e. Eddies) in the neighbourhood of the interface. On the surface of the bubble, turbulent transport disappears since the vortices do not penetrate the air-water interface. Thus, in the immediate vicinity of the boundary, the molecular diffusion is the only mechanism of transport.

For severely contaminated interfaces, hydrodynamic relationships are similar to those of a transport at the solid-liquid interface [10, 39]. Frossling [14] presented a simple models for the theoretical determination of mass transfer coefficients with rigid interface. The predictions based on the models of Danckwerts [9], Higbie [16], and Fortescue and Pearson [13] are available for clean interfaces.

Effect of contaminants on oxygen mass transfer coefficients in bubble column has been investigated in Vasoncelos *et al* [37]. The associated model includes a time parameter that takes into account the surface transition from mobile to rigid as the bubble rises.

Schmidt and Schneider [31] measured the transfer coefficient between gas and seawater to know the characteristics of this exchange in the Baltic Sea. To ensure that seawater samples were comparable, after careful filtering, they measured the surface tension with the Wilhelmmy plate method [27].

Asher and Pankow [1] studied in detail the effects of the film by measuring the mass transfer of $CO_2$ in the water with different surface conditions using the Laser Induced Fluorescence (LIF) non-intrusive method, based on fluorescence emissions depending on pH (see Chapter 5). Different surface conditions were created by various cleaning processes of the liquid surface and the creation of organic monolayers. The experimental results show that the transfer rate is very sensitive to the cleanliness of the interface. The experiments of Chaumat and *al.* [5] also demonstrate that surface tension is a critical parameter that deeply modifies coalescence and mass transfer in bubble columns.

Therefore, Eddies and exchange transfer rate at the interface depend on the state of the transfer surface. Given that the smallest amount of surface active components can influence surface tension, precautions for preparation and cleaning equipment have a very important role. For repeatable results, it is essential to use defined cleaning methods and to control water quality on each experimental setup.

## 1.5 Conclusion

Three applications of bubble columns have been presented: flotation, carbon dioxide sequestration and micro-algae photosynthesis. Columns have a large amount of parameters that influence the physical phenomena involved, like contamina-

tion and turbulence in the flow regime. The vacuum bubble column of the LMFA laboratory was first dedicated to micro-algae culture, using the three functions described in Section 1.1.3. The study in this thesis has been focused on the phenomenon of mass transfer taking place at the interface of a two-phase medium. The liquid phase is either tap water or demineralized water. The gas phase is carbon dioxide, atmospheric air or a mixture of both. Nitrogen has been used in some experiments to modify dissolved gas equilibrium in the water.

Chapter 2 presents the equipment and the results of the experimental studies carried out on the vacuum bubble column of the LMFA. The results confirm the link between the size of the bubble and mass transfer. These conclusions led to Part 2 on Micro-bubble generation, and Part 3 where an optical technique is developed in order to obtain experimental $k_l$ mass transfer coefficient.

# Bibliography


[1] Asher, W., Pankow, J.: The interaction of mechanically generated turbulence and interfacial films with a liquid phase controlled gas-liquid transport process. Tellus B, 38B **5**, 305–318, (1986)

[2] Barrut, B.: Study and optimization of a vacuum airlift: Application to aquaculture. Université Montpellier 2, Ph.D. Thesis (2011)

[3] Boyd, P.W. *et al.*: Mesoscale Iron Enrichment Experiments 1993–2005: Synthesis and Future Directions Science **315**, 612 (2007)

[4] Brumley, B.H., Jirka, G.H.: Near-surface turbulence in a grid-stirred tank. Journal of Fluid Mechanics, **183**, 253–263 (1987)

[5] Chaumat, H., Billet-Duquenne A.M., Delmas, H.: Hydrodynamics and mass transfer in bubble column: Influence of liquid phase surface tension. Chemical Engineering Science **62**, 7378–7390 (2007)

[6] Chisti, Y.: Biodiesel from microalgae. Science Direct, Biotechnology Advances **25** 294–306 (2007)

[7] Coldep: [Online]
http://www.coldep.com/

[8] Cuenot, B., Magnaudet, J., Spennato, B.: The effects of slightly soluble surfactants on the flow around a spherical bubble. Journal of Fluid Mechanics, **339** 25–53 (1997)

[9] Danckwerts, P.V.: Gas-liquid reactions. N.Y./N.Y.: McGraw-Hill (1970)

[10] Davies, J.T.: Turbulence phenomena. N.Y./N.Y.: Academic Press (1972)

[11] Dunahay, T., Benemann, J., & Roessler, P.: A look back at the US Department of Energy's Aquatic Species Program: Biodiesel from algae. Golden: National Renewable Energy Laboratory **328** (1998)

[12] Formanek, V.: Quelques aspects theoriques, techniques et economiques du procede de flottation. Minemet Recherche (1978)

[13] Fortescue, G. F. and Pearson, J. R. A.: On gas absorption into a turbulent liquid. Chemical Engineering Science **22**, 1163–1176 (1967)

[14] Frossling, N.: Ubber die verdunstung fallenden tropfen (Evaporation of falling drops). Gerlands Beitage zur Geophysik, (52) 170–216 (Griffith (1960) Mass transfer from drops and bubbles. Chemical Engineering Science, **12** 198–213)(1938)

[15] Hébrard, G., Roustan, M.: Les différents types de contacteur gaz-liquide. Transfert gaz-liquide dans les procédés de traitement des eaux et des effluents gazeux, Tech& Doc, Lavoisier (2003)

[16] Higbie, R.: The rate of absorption of a pure gas into a still liquid during a short time of exposure. Transactions of the American Institute of Chemical Engineers, **31** 365–389 (1935)

[17] Huang, Z.: Efficacité de Capture dans les Procédés de Flottation. Université de Toulouse, Thesis (2009)

[18] INSA, IFREMER: Process and installation for treating an aqueous effluent for the purpose of extracting at least one dissolved gaseous compound therefrom; Application to aquaculture in a recirculated aqueous environment. Patent: WO 2008006950 PCT/FR2007/000920 (2008)

[19] IPCC Third Assessment Report "Climate Change 2001": [Online] //www.grida.no/publications/other/ipcc_tar/?src=/climate/ipcc_tar/wg1/fig3-2.html
GRID-Arendal, United Nations Environment Programme (Accessed on August 2013)

[20] Knorr, W.: Is the airborne fraction of anthropogenic $CO_2$ emissions increasing? Geophysical Research Letters **36**, L21710,(2009)

[21] Kunjapur, A.M., Eldridge, R. B.: Photobioreactor Design for Commercial Biofuel Production from Microalgae. Industrial & Engineering Chemistry Research, **49** (8), 3516–3526 (2010)

[22] Li-Beisson, Y., & Peltier, G.: Biocarburants : le défi des microalgues. Dossier Pour la Science **N°73** (2011)

[23] Mauna Loa Observatory: [Online]
http://www.esrl.noaa.gov/gmd/ccgg/trends/weekly.html
Earth System Research Laboratory (Accessed on August 2013)

[24] Miyagi, O.: Theory of air-lift pump with special reference to the slip of air bubbles in water. Journal of the society of mechanical engineers (1923)

[25] Microphyt: [Online]
http://www.microphyt.eu/

[26] Muller-feuga, A.: Photosynthetic reactor for cultivating microorganisms, and method for cultivating microorganisms",
Patent: EP2411500 (2012)
http://www.freepatentsonline.com/EP2411500A1.html

[27] Padday, J.F.: In Surface and Colloid Science New York: Wiley-Interscience, **1**, 110–112 (1969)

[28] Pollutec, Communiqué de presse: [Online]
http://www.universite-lyon.fr/valorisation/communique-de-presse-pollutec-156457.kjsp?RH=valooff

[29] Salleh, A.:Urea 'climate solution' may backfire. [Online]
http://www.abc.net.au/science/articles/2007/11/09/2085584.htm
ABC Sience (2007)

[30] Sarrot, V., Huang, Z., Legendre, D.: Experimental determination of particles capture efficiency in flotation. Chemical Engineering Science **62** 7359–7369 (2007)

[31] Schmidt, R., Schneider, B.: The effect of surface films on the air-sea gas exchange in the baltic sea. Marine Chemistry, **126**, 56–62, 9 (2011)

[32] Simpore, J., Kabore, F., Zongo, F. *et al.*: Nutrition rehabilitation of undernourished children utilizing Spiruline and Misola Nutrition Journal **5**(3) (2006)

[33] Taitel, Y., Bornea, D., Dukle, A.E.: Modelling flow pattern transitions for steady upward gas-liquid flow in vertical tubes AIChE Journal **26**(3), 345–354 (1980)

[34] Tampier, M.: A Sober Look at Biofuels From Algae. [Online]
http://www.biodieselmagazine.com/articles/3313/a-sober-look-at-biofuels-from-algae/
Biodiesel Magazine (2009)

[35] United Nations: Kyoto Protocol, 11 December 1997. [Online] http://unfccc.int/kyoto_protocol/items/2830.php

[36] Valiorgue, P.: Mass transfer in intermittent horizontal gas-liquid flow and application to photobioreactors. Université Lyon 1, Ph.D. Thesis (2012)

[37] Vasconcelos, J.M.T., Rodriguesa, J.M.L., OrvalhoaS, C.P., Alvesa, S.S., Mendesb, R.L., Reis, A.: Effect of contaminants on mass transfer coeffcients in bubble column and airlift contactors. Chemical Engineering Science **58**,1431–1440 (2003)

[38] Volk, T.: $CO_2$ rising: the world's greatest environmental challenge. Cambridge, MA: MIT Press (2008)

[39] Whitman, W.G.: Preliminary experimental confirmation of the two-film theory of gas adsorption. Chemical and Metallurgical Engineering **29**, 146–148 (1923)

[40] Zimmermana, W.B., Zandib, M., Bandulasena, H.H.C. *et al.*: Design of an airlift loop bioreactor and pilot scales studies with fluidic oscillator induced microbubbles for growth of a microalgae Dunaliella salina. Elsevier applied energy **88**(10), 3357–3369 (2011)

# Chapter 2

# Global characterization of the vacuum bubble column

*Ce chapitre présente tout d'abord la colonne à bulles à dépression du LMFA ainsi que les résultats obtenus antérieurement. Lors de cette thèse, une expérience de désaturation a été menée pour quantifier l'amélioration des échanges gaz-liquide lorsque la colonne est en fonctionnement. Le circuit de gaz de la colonne a été modifié pour réaliser une étude en boucle fermée, comparable au fonctionnement d'un ensemble de colonnes montées en série. Enfin, un modèle théorique associé à cette configuration a été implémenté et est expliqué à la fin de ce chapitre. Ce modèle met en évidence l'importance de l'aire interfaciale gaz-liquide pour le transfert de masse.*

# Abstract

This chapter first presents the vacuum bubble column of the LMFA and the results previously obtained. During this Ph.D. thesis, an experiment of desaturation has been carried out to quantify the improvement of the gas-liquid exchange when the column is in operation. The gas circuit has been modified for a closed-loop study, similar to the functioning of a set of columns in series. Finally, an associated theoretical model has been implemented and is explained at the end of the chapter. This model highlights the importance of the gas-liquid interfacial area for mass transfer.

# Nomenclature

### Greek symbols

| | |
|---|---|
| $\gamma_L$ | Laplace coefficient, [ ] |

### Latin symbols

| | |
|---|---|
| $A_i$ | Gas-liquid interfacial area, $[m^2]$ |
| $C$ | Concentration, $[\frac{\text{mol}}{\text{m}^3}]$ or $[\frac{\text{kg}}{\text{m}^3}]$ |
| $D_{bubble}$ | Bubble diameter, $[m]$ |
| $k_l$ | Mass transfer coefficient, $[\frac{\text{m}}{\text{s}}]$ |
| $m_{transfered}$ | Mass of $CO_2$ transferred during one passage, $[kg]$ |
| $P$ | Pressure, $[Pa]$ |
| $p$ | Partial pressure of the gas in the gas phase, $[Pa]$ |
| $P_T$ | Total pressure in the medium, $[Pa]$ |
| $V$ | Volume, $[m^3]$ |
| $\delta T$ | Time taken by a bubble to rise through the water column, $[s]$ |

### Subscripts

| | |
|---|---|
| 0 | Reference condition, |
| *overpressure* | Medium in high pressure condition, |
| *sat* | Saturation of the concentration, |
| *underpressure* | Medium in low pressure condition. |

## 2.1 LMFA Column description

### 2.1.1 Equipment

The bubble column studied in this thesis has been developed under co-patent of INSA and IFREMER [6] and is exploited by COLDEP. The water column is created by a depression at the top of the bubble column.

This solution is simple to implement and requires less energy than a water level difference achieved using overpressure [2]. The operation is done in two steps: the setting of the vacuum pump initiates a vacuum within the column and the water level rises. Once the water level reaches the bicone (see below) (care must be taken to maintain it at constant level), the gas injection system is started: the gas bubbles created at diffusers rise in the column, driving the liquid and creating an upward movement in the airlift as shown in diagram 2.1 from the COLDEP website [4].

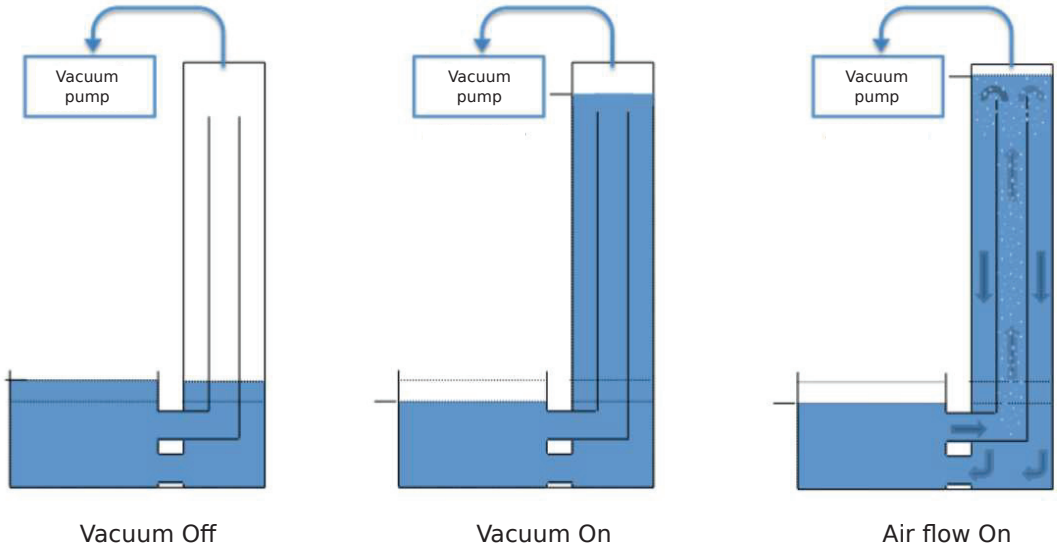


Figure 2.1: Bubble column start-up.

#### General description

The system pictured in Figure 2.2 consists of two concentric cylindrical tubes (outer tube 0.250 $m$ in diameter, inner tube 0.160 $m$) connected at the base to a

tank of 2 $m^3$ capacity. The gas injection in the inner tube forms bubbles that drive up water present in the inner tube. Once at the top of the column, the majority of bubbles escape into the bicone (described below) while water goes down in the outer tube, before returning to the tank.

### The bicone

Once the level of depression has been established at the top of concentric tubes, the bicone (see Figure 2.3) is the system able to harvest the foam formed by the presence of suspended substances. These are driven upward by the bubbles and come to form a compact foam at the surface. This foam falls inside the bicone and is transferred by gravity into the harvest tank. The bicone also serves to regulate the level of water in the column. If the level exceeds the top of the column, the excess of water is drawn into the harvest tank.

### Vacuum pump

It is used to create the depression at the top of the column. The model used at INSA is a LX0030A Busch liquid-ring vacuum pump. Sealing is created by a water film which requires the installation of a sub-tank. This sub-tank will be modified when operating in closed circuit (see Section 2.3). Note that the vacuum pump is not directly connected to the bicone: an intermediate tank is installed between the two elements in order to prevent water being sucked up by the vacuum pump. A manometer and a valve installed on the tank regulates the depression level.

### Measuring instruments

The column is designed with various access points provided for following instrumentation:
- an electromagnetic Bürkert flow-meter on the water inlet tube of the column. This flow-meter allows measurements of instantaneous flow rate and volume of water flowing through the aspiration tube ;
- 19 pressure taps in the outer or inner tube of the column, allowing measurements by differential pressure gauge. They are distributed every 30 centimeters between 45 and 585 centimeters ;
- 5 access points for an optical probe. These sensors are placed in the inner tube, allowing void fraction measurements ;
- gas flow is controlled by flow-meters and manometers along the input gas circuit ;
- a $CO_2$ sensor InPro 5000/12/120 de METTLER-TOLEDO Analyse Industrielle is immersed in the tank, allowing measurements of the temperature, the partial pressure, the concentration and saturation of the dissolved carbon.

Figure 2.2: Bubble column of the LMFA.

Figure 2.3: Bicone for foam harvesting at the top of the column.

### 2.1.2 Gas injection systems

Homogeneous dispersion of the bubbles can be done in various ways:
-through a porous membrane ;
-through porous aerator in plastic, ceramic or wood ;
-using venturi effect ;
-using the rising velocity of the bubble and perforated metal sheets ;
-mechanical agitators shearing bubbles in turbulences or with a rotor-stator device ;
-air dissolution by overpressure, followed by decompression.

In the LMFA bubble column, gas injection is performed by diffusers that can be connected to gas cylinders, mobile compressor, or laboratory compressor. The air is always filtered to take off any oil droplets.

Various types of diffusers have been used depending on the size and quantity of the desired bubbles, under a given pressure and flow rate:
- 'open pipe ' diffusers (large bubble diameters from 0.5 $cm$ to 3.0 $cm$) ;
- micro-bubble diffusers (bubble diameters of hundreds of microns), which are generally made of porous ceramic. They generate the greatest head losses. One ceramic diffuser is beneath the inner tube, and two other thinner ceramic diffusers are mounted directly inside the inner tube.

Bubble size is a key factor to increase mass transfer in a bubble column. Therefore the diffuser choice is important, and it is necessary to examine the various existing diffusers. Among common diffusers, wood and ceramic diffusers produce the smallest bubbles (see Figure (2.4)). A study of these diffusers has been performed, determining the mean diameter of produced bubbles.

An aquarium filled with 15 $L$ of tap water has been used in the experiment pictured in Figure (2.5). The studied diffuser (wood or ceramic) was connected by a tube to a syringe. This syringe was fixed to a syringe pump Lambda Vit-Fit (selected speed: 0.8 $mm/min$). Using a high speed FASTCAM Photron SA4 12-bits camera, coupled with a NAVITAR Lens Zoom 6000, clear images of micro-bubbles in motion (660 to 120 $\mu m$) have been recorded. The camera has been placed in front of the tank, so as to capture images just above the diffuser. The aquarium bulk was highly illuminated by LED bulbs. The resolution is $1024\times1024$ for all shots. The acquisition frequencies range from 1000 to 3000 $fps$. Before each recording, an optical pattern has been placed in the tank in the plan of the diffuser, and an image was taken in order to calibrate the recorded area. The resulting scale was found to be 15 $\mu m/pix$.

It has been observed that the wood diffuser produces larger bubbles in fresh water than the ceramic diffuser (average diameters: 0.54 $mm$ v.s. 0.25 $mm$). In salted water (33 $g/L$), the difference is less marked between the two diffusers: the wood diffuser gives an average bubble diameter of 0.18 $mm$, v.s. 0.15 $mm$ for

Figure 2.4: Ceramic and wood diffusers.

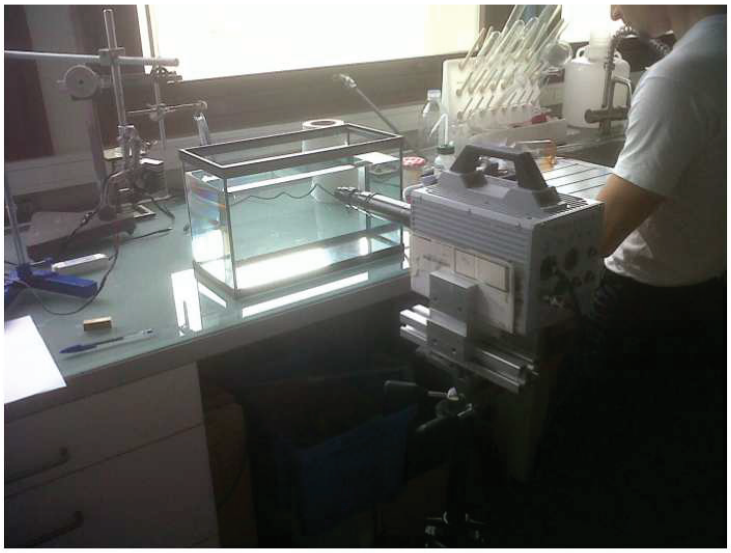

Figure 2.5: Experimental setup for the measurement of bubble diameters generated by wood and ceramic diffusers.

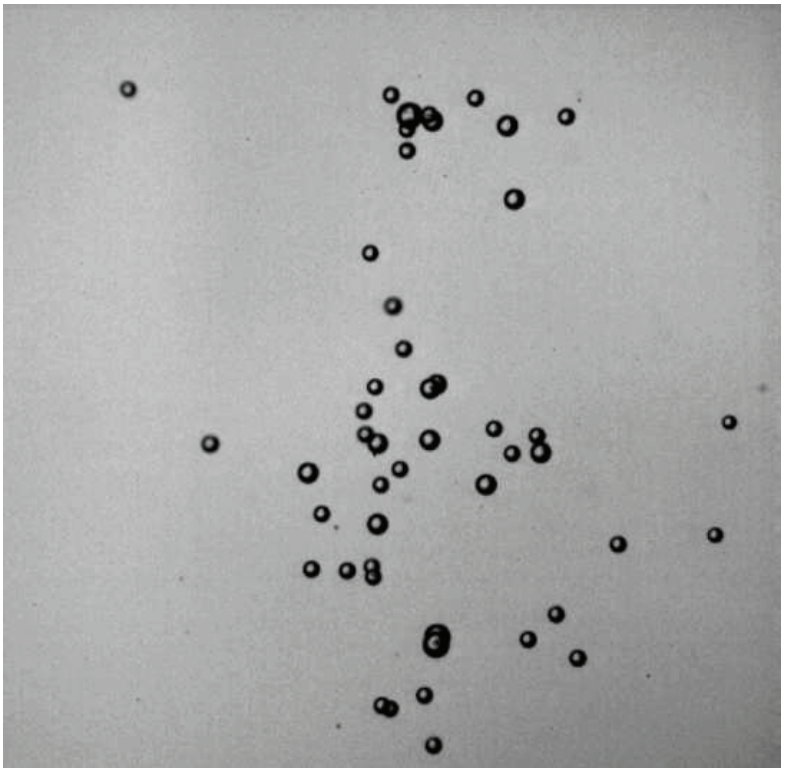

Figure 2.6: Free rising bubbles from a ceramic diffusers in tap water, using a FASTCAM Photron SA4 camera at 3000fps, coupled with a NAVITAR Lens Zoom 6000. The average bubble diameter is 0.25 $mm$.

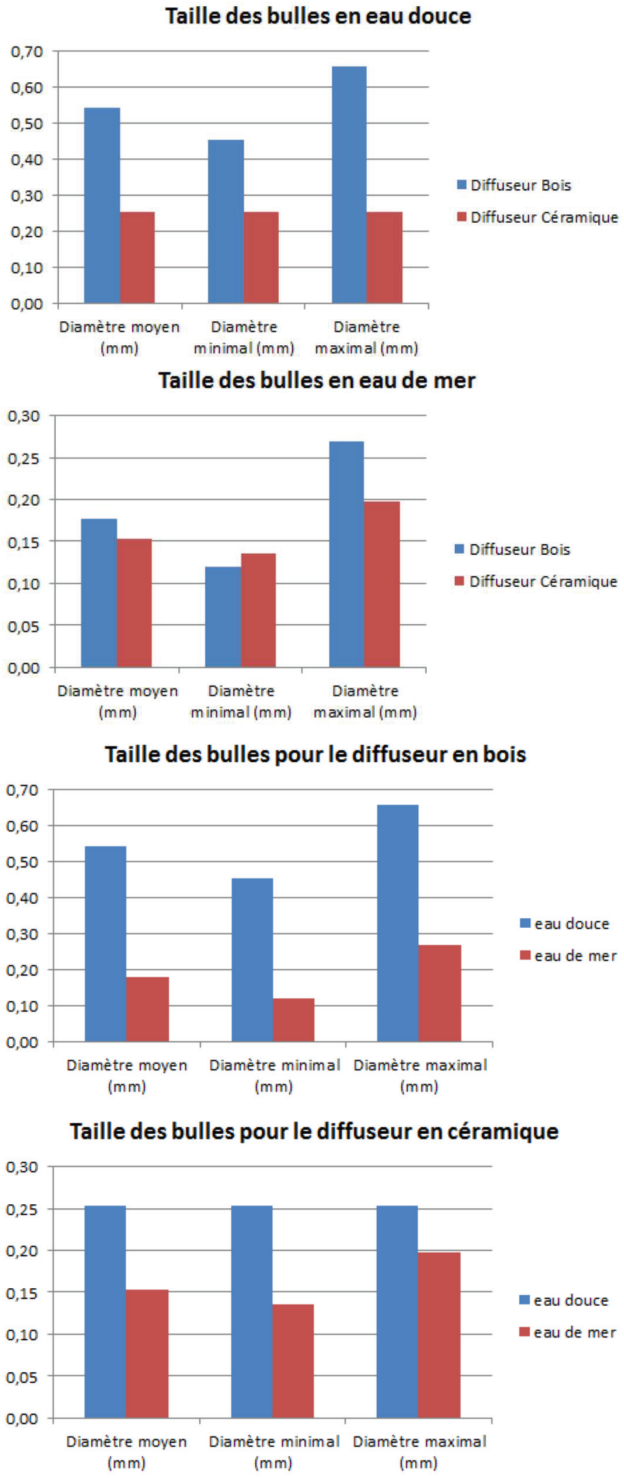


Figure 2.7: Bubble diameters in fresh or salted water with ceramic and wood diffusers, from [5].

the ceramic (see Figures (2.6) and (2.7)). For all these experiments, gas flow rate was kept very low in order to avoid bubble collision and overlapping on recorded images. In a more conventional use, bubble coalescence results in larger bubble diameters.

This quick experiment confirms that salinity plays an important role on the bubble size. In salted water, the phenomenon of bubbles coalescence is decreased because of the salt which is a surfactant, resulting in more fine bubbles and hence a larger exchange surface than in freshwater. The experiments presented in this work are limited to freshwater. For more information, one can read the article of Asher et al. [1]: "On the differences between bubble-mediated air-water transfer in freshwater and seawater".

### 2.1.3 Influence of the parameters

This section is a quick compilation of works made since 2008 on the LMFA vacuum bubble column by Narvaez,C. [7], Barrut, B. [2], Dabernat, R., Soare, C., Festaud, J., Truchet, F. [5] and the present author. It gives the general evolution of the functions of the column, depending on the studied parameters.

#### Influence of the type of injected gas

The characteristics of density and surface tension varies from one element to another. Therefore, changing the gas may affect bubble size, rising velocity, and the flow. Tests have been conducted with compressed air, pure nitrogen and pure $CO_2$.

The flow differences between the 3 gases are presented in Figure (2.8). In the case of a column whose main function would be pumping, air and nitrogen seem more reasonable choices as they are more economic than pure $CO_2$.

#### Influence of gas flow

A higher flow rate of injected gas increases the amount and size of bubbles, which has a positive effect on the mass transfer coefficient and accelerates the exchanges (see Section 2.1.3).

The liquid flow rate is expected to enhance as well (see Figure (2.8)). As pictured in Figure (2.9), increasing the gas flow enhances the liquid flow rate, independently of the type of diffuser used. Gas flow has been tested from 1 to 140 $L/min$, a flow rate that ensures no appearance of counter-airlift effect.

A phenomenon of counter-airlift may appear in certain conditions as the flow increases: bubbles in the external tube (downward flow) become bigger and finally rise up to the top of the column (see Figure (2.10)). When appearing, this

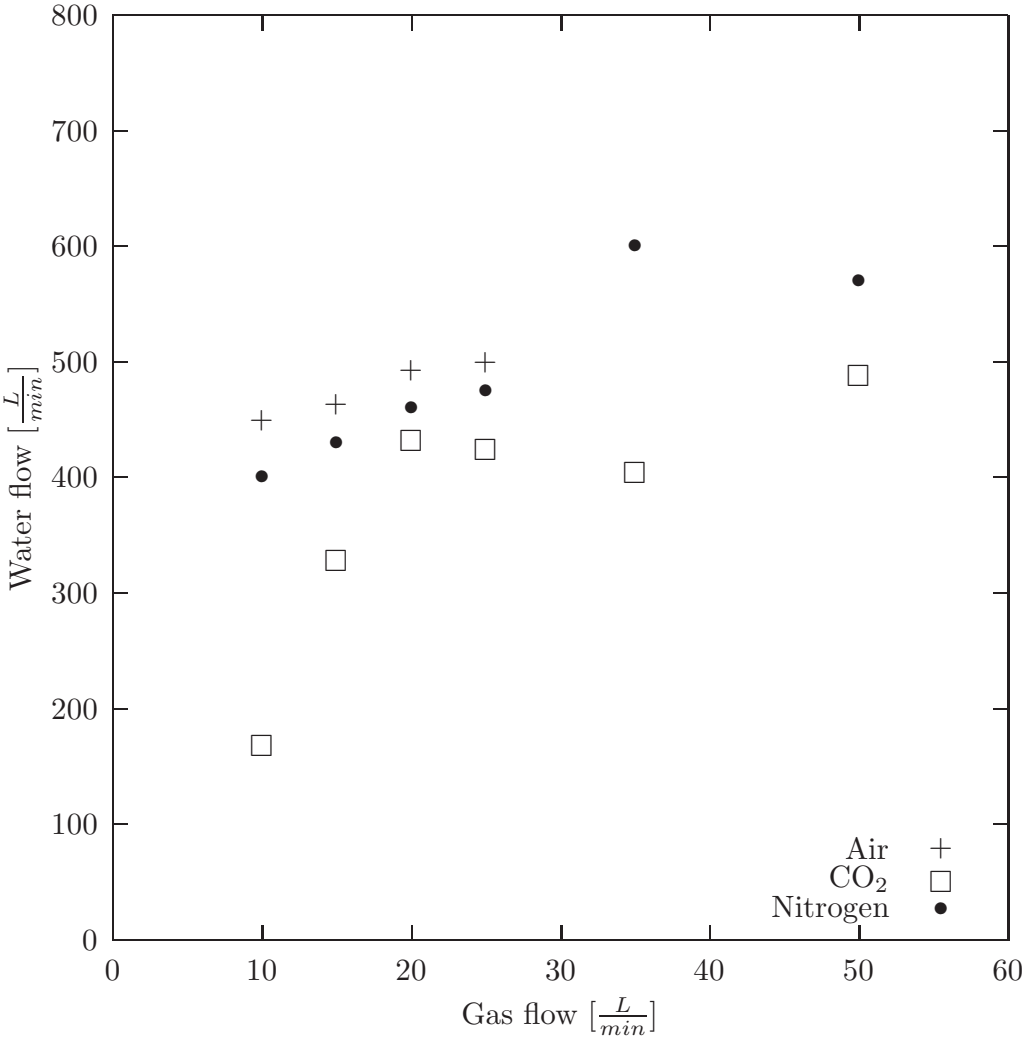


Figure 2.8: Water flow rate versus gas flow rate using 3 different gases and a ceramic diffuser.

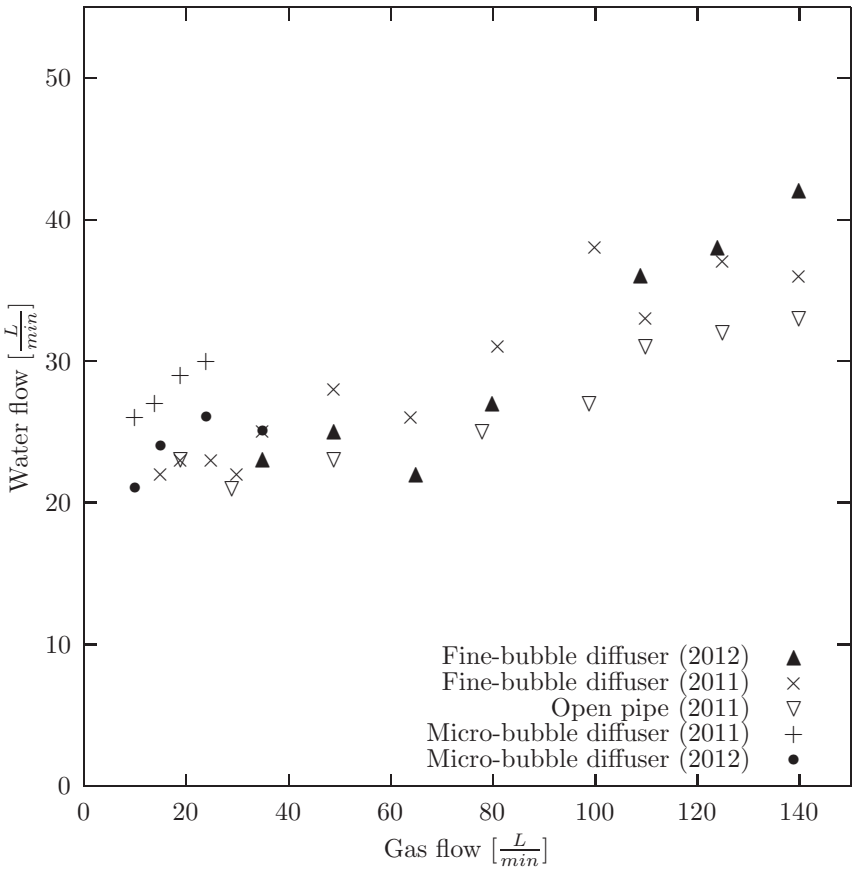


Figure 2.9: Water flow versus air flow using different diffusers.

phenomenon can temporarily slow down the liquid flow in the external tube.

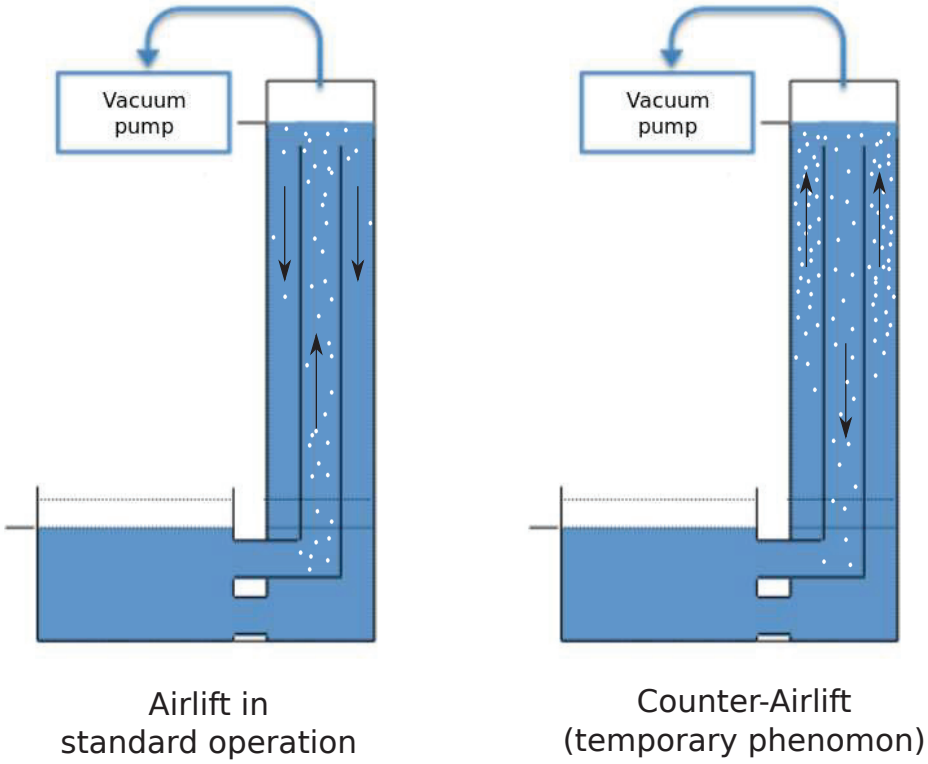


Figure 2.10: Counter-airlift phenomenon.

### Influence of the diffuser type

Bubble size is a parameter that will depend on various conditions like the injection pressure, the inlet flow rate, and the type of used diffuser. As reported in Figure (2.9), experiments have been carried out to investigate diffuser influence on the water flow, using a micro-bubble diffuser, a fine-bubble diffuser, and an open pipe. The coalescence of bubbles is very high at high injection rates, so the difference in size between the bubbles of a fine-bubble diffuser and micro-bubble diffuser is minimal after a certain height in the column. Thus, few differences were observed between the gas flow rates obtained with the fine bubble diffuser and those obtained using the micro-bubble diffuser.

**Influence of water level**

Depression and the water level inside the column have an influence on the air flow. While rising, the bubble "inflates" due to the external pressure decrease (gas being compressible). Using Archimedes' principle, the buoyant force increases with the increase of bubble volume (compression of the water is neglected). Therefore, rising velocity increases to a limit depending on the friction forces. The size modification also induces a change in the friction coefficient because the cross-section changes. Finally, a larger height difference between the water level in the tank and the top of the column will result in higher bubble rising velocities. Increasing the height of water can increase the flow of liquid and therefore the effectiveness of the pumping function.

**Influence of bubble size**

For a given volume, the void fraction and the total exchange surface is higher in the case of a large number of small bubbles than in the case of a few larger bubbles. A demonstration is given later in Section (3.1.5). Therefore, reducing the average size of the bubbles by changing the diffuser maximizes exchanges between the liquid and gaseous media and increases the $k_l a$ (see equation 1.8).

## 2.2 Desaturation of $CO_2$ in the column

As written previously, the works carried out and presented in this document are focused on mass transfer. In order to quantify the mass transfer between water and carbon dioxide in the vacuum column, two experiments have been performed to study the desaturation of carbon dioxide:
- Stationary desaturation of $CO_2$ in the tank, in fresh water, without operating the column ;
- Desaturation of $CO_2$ with operating column, in fresh water, and air injection.

### 2.2.1 Stationary desaturation

Experimental protocol:
1. Large injection (stripping) of atmospheric air in the column.
Initial conditions after stripping:
$[CO_2]$ : 0.2 $mg.L^{-1}$
Saturation: 2.4%
Temperature: 24°$C$
Pressure: 150 $mbar$
2. Direct injection of large bubbles of $CO_2$ in the tank, using a gas bottle loaded

with 99.7% pure $CO_2$ ;
3. Checking of the $CO_2$ saturation displayed by the probe at the surface ;
4. Once saturation is maximum (about 90%), the gas injection is stopped ;
5. Measurement reading of concentration values ($mg.L^{-1}$), saturation (%), temperature ($°C$) and pressure ($mbar$) up over time, until stagnation.

Overall, the desaturation phenomenon is rather slow. With no movement nor other exchange than the free surface of the tank, the carbon dioxide evaporates very slowly to the atmosphere. $CO_2$ concentration decreases exponentially over twenty days before it finally stagnates. As shown in Figure (2.11), ten days (about 15 000 minutes) are needed to decrease from 1200 $mg.L^{-1}$ to 200 $mg.L^{-1}$. And ten more days are necessary to finally get closer to 30 $mg.L^{-1}$. The free surface of the tank is not large enough to allow a more rapid exchange. The experiment has been repeated with the operating column.

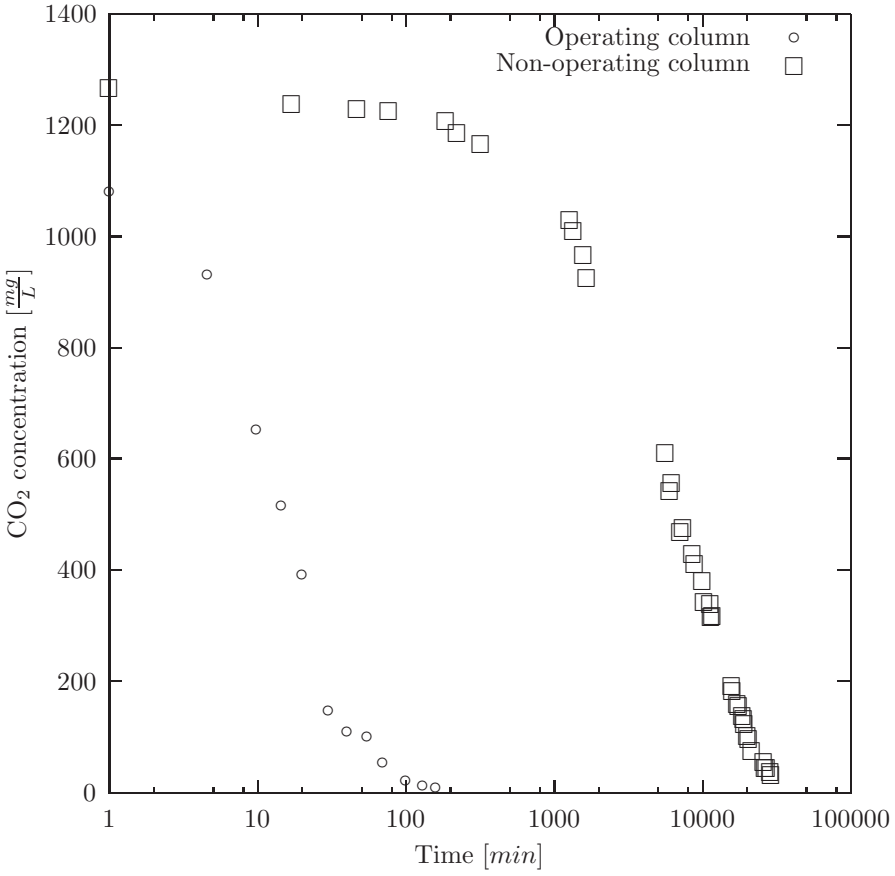


Figure 2.11: Comparison of $CO_2$ desaturation in operating and non-operating column, with time axis in logscale.

### 2.2.2 Desaturation with operating column

Experimental protocol:
1. Large injection (stripping) of atmospheric air in the column.
Initial conditions after stripping:
$[CO_2]$ : 0.4 $mg.L^{-1}$
Saturation: 6.2%
Temperature: 23.8°$C$
Pressure: 155 $mbar$
2. Direct injection of large bubbles of $CO_2$ in the tank, using a gas bottle loaded with 99.7% pure $CO_2$ ;
3. Checking of the $CO_2$ saturation displayed by the probe at the surface ;
4. Once saturation is maximum (about 90%), the gas injection is stopped ;
5. The vacuum column is activated ;
6. Injection of air at 20 $L/min$ through fine bubble diffuser, pressure fixed to 2 bar ;
7. Water level adjustment ;
8. Measurement reading of concentration values ($mg.L^{-1}$), saturation (%), temperature (°$C$) and pressure ($mbar$) up over time, until stagnation.

This time, the exchange is much faster. It takes only 30 minutes to obtain a concentration of carbon dioxide below 200 $mg.L^{-1}$, and after 2:40, there is only 6 $mg.L^{-1}$ of $CO_2$ (see Figure (2.11)). Gas-liquid mass transfer is much faster due to the exchange surface that is larger because of the presence of small bubbles injected into the column.

## 2.3 Closed loop experimental study

In the context of carbon transfer into water for micro-algae culture, the gas used in the column would be in the form of gaseous mixtures which can be released, for example, from chemical or petroleum industries. These mixtures contain a certain percentage of $CO_2$, that may vary, and in which only a fraction will be absorbed by the water during the passage of gas bubbles in the column. In open circuit, the remaining gas is then discharged to the atmosphere at the outlet of the vacuum pump. A study was performed in closed-loop circuit with the following objectives:
- Avoid harmful gas emissions into the atmosphere. Even in cases where $CO_2$ is the only harmful gas present in mixtures, its presence in the confined atmosphere of a laboratory or closed industrial center has to be avoided ;
- Maximize the speed of growth of algae by injecting more carbon in the column.

From an industrial viewpoint, this study of closed-loop circuit operation sim-

ulates the passage of gas in a succession of columns in series.

### 2.3.1 Gas circuit modifications

On our test bench, the gas circuit is closed by connecting the discharge of gas from the vacuum pump to the gas injection system (see Figure 2.12): the initially injected gas can be reused in the circuit, each passage allowing to transfer a little more carbon from gas to water.

Once a vacuum is created and fluid flow is initiated (by injecting compressed air into the diffuser), the injection of gas in the circuit and the establishment of the closed circuit allows the establishment of a self-sustaining system of movement where no gas addition is necessary to maintain the functions of pumping and transfer of the column.

If leaks are neglected in the system, the only exchange with the outside takes place at the surface of the tank. Comparison of the experiments presented above in Section 2.2.2 allows us to neglect this exchange. Note that the reactivation of the electro-valve and its sensor would enable to close the flow leak of the vacuum pump that regulates the water level in the column.

The evolution of $CO_2$ concentration is measured in the tank using the $CO_2$ sensor (described in Section 2.1.1).

Modifications have been performed on the pneumatic circuit to enable closed-loop gas flow. The gas injected into the column must be recovered and injected again. The vacuum pump used is not designed to provide a pressure at discharge (only 0.1 *bar*). Pressure of the discharge gas going back to the injection is insufficient to overcome the head losses in diffusers. A compressor is installed between the discharge outlet of the vacuum pump and the diffusers, in order to counter the head losses of the fine bubble diffuser during the re-injection of the vacuum pump output gas. It re-injects the undissolved gas back in the column, with a maximum pressure of 8 bars. An oil filter and water filter were installed before the compressor inlet to avoid the presence of water and oil in the mobile compressor. We also could replace the vacuum pump with a model capable of providing a pressure sufficient to overcome the head losses in diffusers (more expensive solution).

At the beginning of the airlift start-up, the vacuum is not yet established in the column, and a certain amount of gas is present inside. The establishment of the vacuum requires operation in open circuit for discharging the gas. The passage between the operation in open circuit and closed circuit is easily operated with 3 way valves. The gas flow extracted from the bottle is controlled in flow rate and pressure so as to know the amount of gas injected.

To maintain the vacuum in the column during the gas injection phase, the vacuum pump must continue to work to compensate for the addition of gas that tends to lower the water level in the column. 3 way valves have been installed so

that during the initial phase when the gas cylinder is injected in the column, a portion of the gas passing through diffusers comes from the bottle, while another part has already been injected and sucked by the vacuum pump, and returns to the pneumatic circuit for a new injection.

### 2.3.2 Closed loop experimental study at 20% and 50% $CO_2$

Experiments on the closed-loop column tend to simulate the re-injection of waste gas coming either from fermentation (40% $CO_2$) [9] or from the exhaust of combustion engine (14%$CO_2$) [10].

In the laboratory context, 2 available gas bottles have been chosen for the experiment, containing:
- 20% of $CO_2$ and 80% of nitrogen ;
- 50% of $CO_2$ and 50% of nitrogen.

A known quantity of carbon from the gas bottles mixture has been injected into the closed-circuit column. The concentration of dissolved $CO_2$ has been monitored using the $CO_2$ probe immersed in the tank. During the experiment, it is assumed that:
- temperature is constant ;
- leak rate from the vacuum pump (controlling water height) has no influence on the results ;
- water flow rate is constant.

The operations to turn-on the closed-circuit column are done in four steps:
- the start-up of the vacuum pump initiates a vacuum within the column and the water level rises ;
- once the water level reaches the bi-cone, the gas injection system is started: the gas bubbles created at diffusers rise in the column, driving the liquid and creating an upward movement in the airlift.
- the gas recirculation system is started when the mobile compressor is turned-on. This compressor counters the head losses of the diffusive system (which is around 5 bars) ;
- at $t = 0\ s$ a known quantity of carbon from one of the gas bottles is injected into the closed-loop circuit using Laplace's law.

Under perfect gas hypothesis and using Laplace's law (see Equation (2.1)), one can determine the injected quantity of carbon by knowing the pressure, the flow rate, and the composition of the gas mixture [8]:

$$P_0 \times V_0^{\gamma_L} = P \times V^{\gamma_L} \tag{2.1}$$

where P and $P_0$ are pressures ($Pa$), V and $V_0$ are volumes ($m^3$), and $\gamma_L$ is Laplace's coefficient depending on the gas nature.

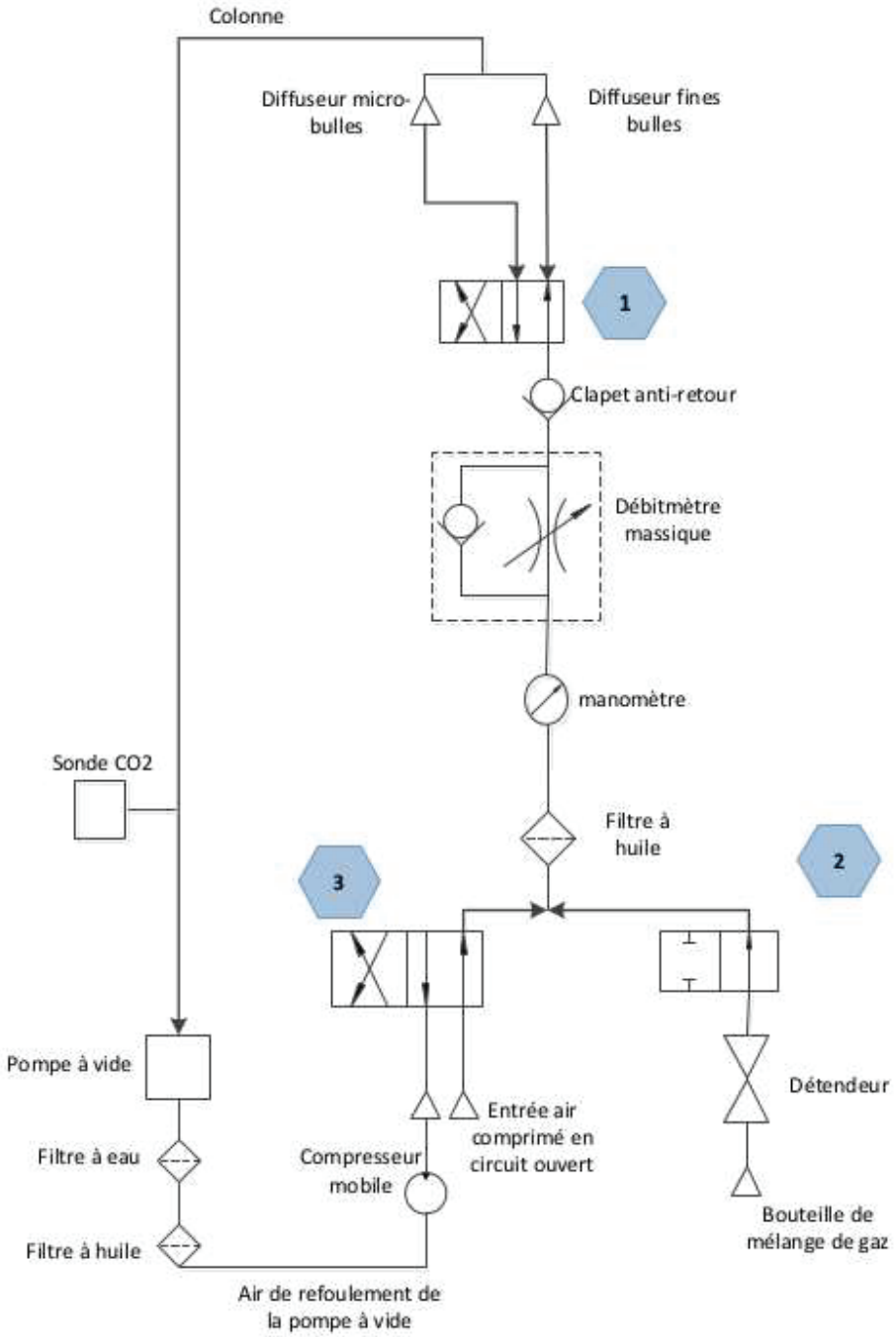


Figure 2.12: Closed loop circuit (from Pahaut [8]).

Experiments have been done at two different gas flow rates: $20L/min$ and 40 $L/min$. In addition to the study of mixtures containing 20% and 50% of $CO_2$, the same experiments have been performed using pure $CO_2$ (99.7%). For these three gas compositions, a volume equivalent to 100 $L$ under atmospheric pressure has been injected. Thus, a known amount of carbon is added to the unknown volume of atmospheric gas already present in the column.

During the first 30 minutes after injection at $t = 0$ $s$, $CO_2$ probe measurements have been reported every minute. Then values have been reported every 10 minutes for 90 minutes. Results are presented in graphs (2.13) and (2.14).

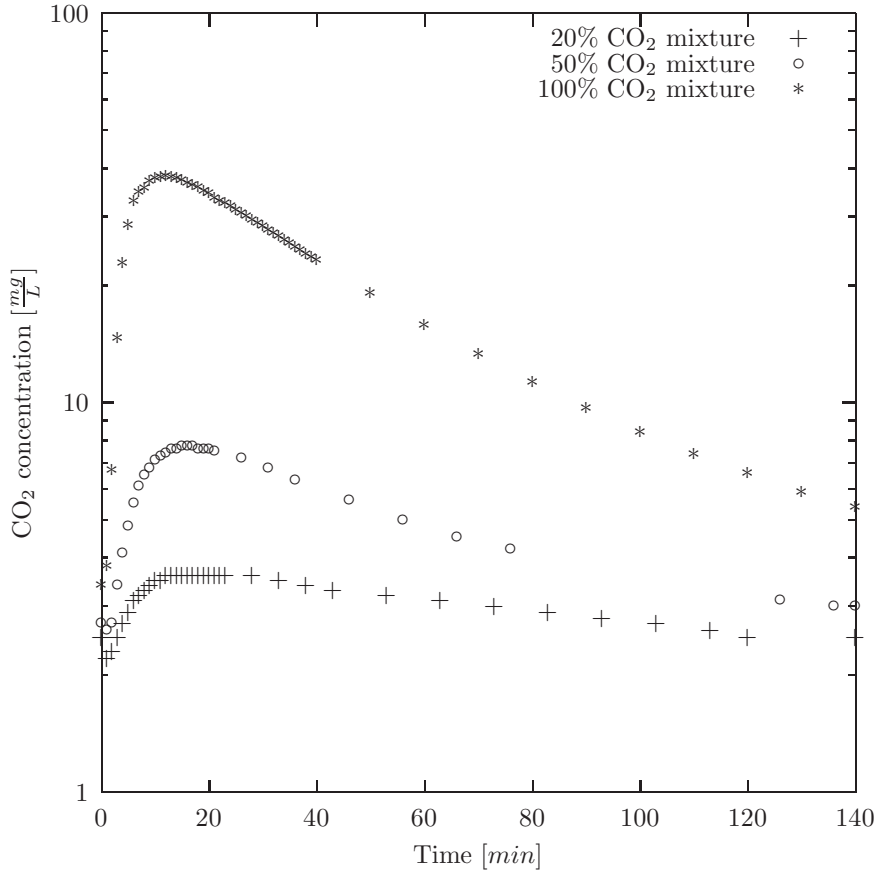


Figure 2.13: Evolution of dissolved $CO_2$ concentration in water at a gas flow rate of 20 $L/min$. The experiment has been performed using gas containing 20%, 50% and 100% of $CO_2$.

Initially, water in the column is in equilibrium with the atmosphere, and the $CO_2$ probe measures a concentration around 2.5 $mg/L$. After the initial carbon

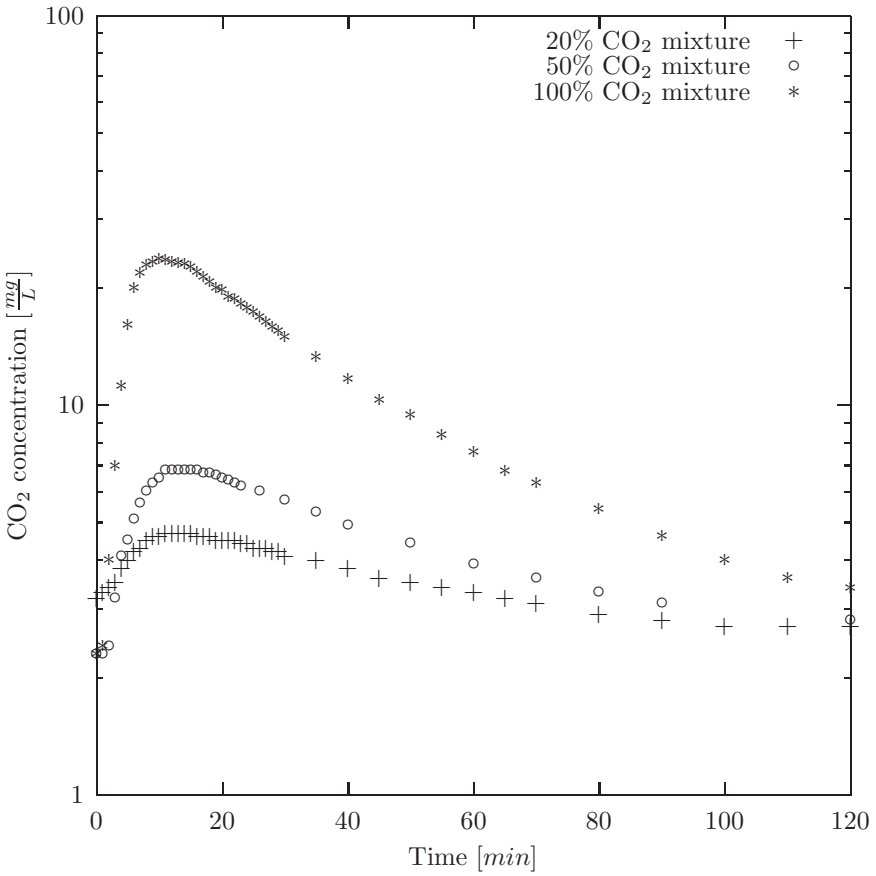


Figure 2.14: Evolution of dissolved $CO_2$ concentration in water at a gas flow rate of 40 $L/min$. The experiment has been performed using gas containing 20%, 50% and 100% of $CO_2$.

| 20 $L/min$ | [$CO_2$]max | [$CO_2$]min | $t_{max}$ (minutes) |
|---|---|---|---|
| 100% | 38.1 | 3.4 | 11 |
| 50% | 7.7 | 2.7 | 15 |
| 20% | 4.9 | 3.5 | 18 |

Table 2.1: Extrema values of dissolved $CO_2$ concentration ($mg/L$) at 20 $L/min$ flow rate.

| 40 $L/min$ | [$CO_2$]max | [$CO_2$]min | $t_{max}$ (minutes) |
|---|---|---|---|
| 100% | 23.7 | 2.3 | 10 |
| 50% | 6.8 | 2.3 | 11 |
| 20% | 4.7 | 3.2 | 11 |

Table 2.2: Extrema values of dissolved $CO_2$ concentration ($mg/L$) at 40 $L/min$ flow rate.

injection at $t = 0\ s$, the carbonate concentration reaches a maximum at $t_{max} = 10$ to 18 minutes (see Tables 2.1 and 2.2). One can note that unlike the previous experiment at 20 $L/min$ gas flow rate, the test at 40 $L/min$ reveals that maximum concentrations are almost reached after a same period $t_{max}$ (10, 11 and 11 minutes). Then carbonate concentration measured by the probe in the tank connected to the column decreases, due to the mass transfer at the surface of the tank. Mass transfer depends on the concentration gradient (see Equation 1.7), thus the decrease slows down as the concentration tends asymptotically to the atmospheric concentration.

The three curves tend to the atmospheric equilibrium concentration of 2.5 $mg/l$. Pure $CO_2$ gas takes longer to reach this value than the other two mixtures. This seems logical since water is loaded with more carbon, thus the dissolved $CO_2$ concentration in the water takes longer to return to equilibrium.

## 2.4 Closed loop theoretical model

In parallel with the experimental closed loop study, a mass transfer model has been implemented for the vacuum bubble column. The aim of the model is to determine how many cycles are necessary to decrease the $CO_2$ concentration to a threshold. Thresholds have been fixed at a $CO_2$ molar fraction of 10% for fermentation gas, and 2% for exhaust gas. For this work, a cycle is defined as one passage of the injected volume of gas in the bubble column.

About forty input parameters are necessary to calculate the number of cycles, including the geometry of the bubble column, water and gas properties, bubble mean diameter and mass transfer coefficient. Parameters have been chosen in order to compare results with the previous experimental study (Section 2.3.2):
- Value of the two gas flow rates: 20 $L/min$ and 40 $L/min$ ;
- Volume of the injected gas under atmospheric pressure: 100 $L$ ;
- Gas composition: 50% $CO_2$ (alias fermentation gas) and 20% $CO_2$ (alias exhaust gas).

It should be noted that this model is based on the evolution of the $CO_2$ mass

contained in the gas phase, whereas the $CO_2$ probe in the previous experiment was measuring $CO_2$ concentrations in the liquid phase.

### 2.4.1 Laws and assumptions of the model

The physics of mass transfer have been described in Section (1.3). The following laws are involved in the proposed theoretical model:
- Henry (equation 1.3) ;
- Dalton (equation 1.4) ;
- Fick (equation 1.5) ;
- Ideal gas (equation 1.10).

Following assumptions have been adopted:
- It is assumed that there is no coalescence between bubbles ;
- The bubble diameter is an average value taken from data of previous works on the INSA bubble column, of the order of cm ;
- Considering renewed water, it is assumed that $CO_2$ concentration in the liquid phase is constant and equal to the $CO_2$ concentration of the gas phase at equilibrium with the atmosphere $C_{sat}$ ;
- It is assumed that $CO_2$ behaves as an ideal gas at constant pressure and constant temperature.

### 2.4.2 Closed loop theoretical study at 20% and 50% $CO_2$

$k_l a$ mass transfer coefficients have been taken from previous works [2, 7] on the INSA bubble column:
- 0.0001 $s^{-1}$ for 20 $L/min$ gas flow rates ;
- 0.0004 $s^{-1}$ for 40 $L/min$ gas flow rates.

In this model, the injected volume of gas has been fixed at 100 $L$ under 1 $atm$. Bubble diameter is also chosen by the user, allowing to consider bubbles created from various diffusers (see Section 2.1.2) It is therefore possible to calculate the volume of one bubble, the number of bubbles, and finally the global interfacial area $A_i$ of all the bubbles in the water column.

The time taken by a bubble to rise through the 5 $m$ water column is determined using the Figure reported in Clift, Grace and Weber [3] giving bubbles rising velocities according to their diameters. For example, for a 0.005 $m$ diameter bubble, the rising velocity has been approximated to 0.25 $m/s$, leading to $\delta T = 20$ $s$ of rising for each passage. This approximated velocity do not take into account the bubble interactions and the hydrodynamic phenomena. The amount of injected $CO_2$ is calculated, depending on the composition of the gas mixture (50% or 20%). After a first passage in the bubble column, this initial quantity

| | 20 $L/min$ | | 40 $L/min$ | |
|---|---|---|---|---|
| $D_{bubble}$ | Cycle | Time(min) | Cycle | Time(min) |
| 0.5mm | 7 | 35 | 4 | 10 |
| 2.75mm | 29 | 195 | 23 | 58 |
| 5mm | 45 | 225 | 27 | 67.5 |

Table 2.3: Cycles necessary to drop the $CO_2$ molar fraction from 20% (representing exhaust gas) to 2%, according to the proposed model. Results are presented for bubbles of diameter 0.5 $mm$, 2.75 $mm$ and 5 $mm$, with a gas flow rate of 20 $L/min$ and 40 $L/min$.

of $CO_2$ is diminished by the carbon transfer from the gas phase into the liquid phase.

After temporal and spatial integration of equation (1.7), the transferred mass is computed using the following formula:

$$m_{transfered} = k_l \times (C - C_{sat}) \times \delta T \times A_i \tag{2.2}$$

where $m_{transfered}([kg])$ is the mass of $CO_2$ transferred during one passage, $k_l$ ($[m/s]$)is the mass transfer coefficient, $C$ ($[kg/m^3]$) is the previous carbon molar concentration, $C_{sat}$ ($[kg/m^3]$) is the carbon molar concentration of the gas phase at equilibrium with the atmosphere, $\delta T$ is the time taken by a bubble to rise through the 5 $m$ water column, and $A_i$ describes the exchange interface of all the bubbles in the water column.

When in equilibrium with the atmosphere, the average carbon concentration in water measured by the Metler Toledo $CO_2$ probe is $C_{sat} = 0.0025\ kg/m^3$ The residuum amount is the initial amount minus the transferred amount. This computation is iterated, reproducing cycles of gas passage in the closed loop bubble column. As the carbon is transferred into liquid phase, the concentration gradient decreases, thus the transferred amount of carbon diminishes at each passage. Diagram 2.15 summarizes the global frame of the model.

In this model, the gas flow rate has no influence on the transferred mass at each passage, but one passage is completed faster as the gas flow rate increases. Increasing the flow rate leads to faster cycles, and therefore one can reach the threshold in a shorter period. Results in Table 2.3 have been presented in Julia Pahaut's report [8], using the model implemented in a '.xls' data-sheet.

Accordingly to theory, the model is highly sensitive to the bubble diameter. For the same volume of gas, smaller bubbles will have a higher interfacial area, leading to a better mass transfer. If small bubbles can be produced by the injection system, it seems interesting to mount a succession of bubble columns in

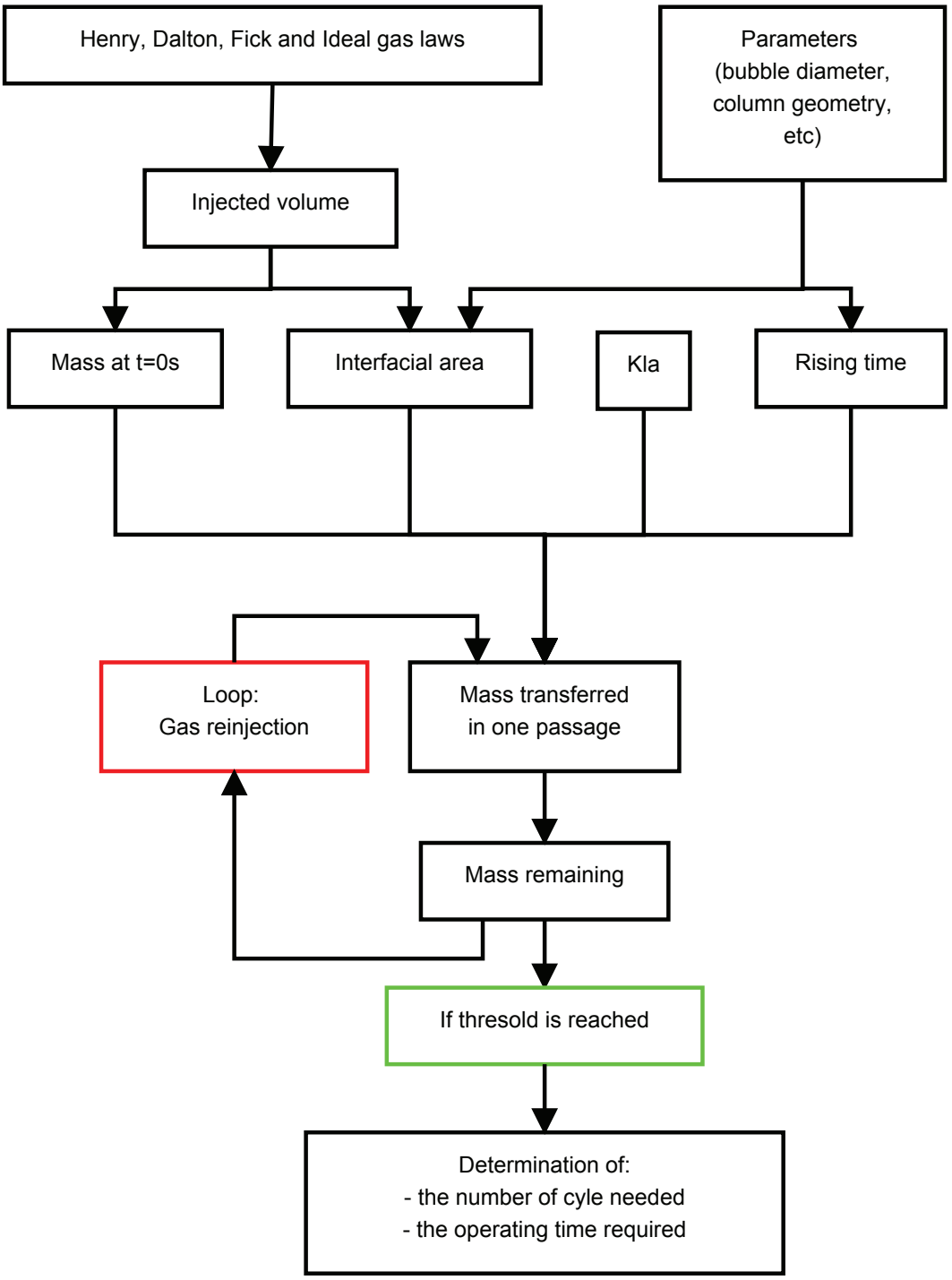


Figure 2.15: Graphical representation of the .xls model for the closed loop theoretical study.

| | 20 $L/min$ | | 40 $L/min$ | |
|---|---|---|---|---|
| $D_{bubble}$ | Cycle | Time(min) | Cycle | Time(min) |
| 0.5mm | 5 | 25 | 3 | 7.5 |
| 2.75mm | 26 | 130 | 16 | 40 |
| 5mm | 31 | 155 | 19 | 47.5 |

Table 2.4: Cycles necessary to drop the $CO_2$ molar fraction from 50% (representing fermentation gas) to 10%, according to the proposed model. Results are presented for bubbles of diameter 0.5 $mm$, 2.75 $mm$ and 5 $mm$, with a gas flow rate of 20 $L/min$ and 40 $L/min$.

series, since the number of column is from 3 to 7 (see Tables 2.3 and 2.4), depending on the gas flow rate and the aimed molar fraction of $CO_2$.

Nevertheless, if the injection system produces bubbles larger than 2 $mm$, the surface area is drastically reduced, thus a large number (16 to 45 according to our simulations (see Tables 2.3 and 2.4)) of columns in series would be necessary. The price of required equipment should be studied carefully, and an estimation of the profitability has to be conducted before scale up.

## 2.5 Conclusion

The desaturation experiment has revealed the efficiency of the bubble column: $CO_2$ has been released into the atmosphere quickly, due to water agitation and the increase of gas-liquid interfacial area. Closed-loop sequestration studies have been carried out, and a related model has been implemented. The experimental investigations and the proposed model reveal the critical importance of the interfacial area for mass transfer in bubble columns. Thus injecting large amounts of gas in the form of small bubbles is a relevant solution. Several devices have been created in order to generate micro-bubbles. Those systems are presented in the following chapter.

# Bibliography


[1] Asher, W.E., Karle, L.M.,Higgins, B.J.: On the differences between bubble-mediated air-water transfer in freshwater and seawater. Journal of Marine Research **55**(5), 813–845 (1997)

[2] Barrut, B.: Study and optimization of a vacuum airlift: Application to aquaculture. Université Montpellier 2, Thesis (2011)

[3] Clift, R., Grace, J., Weber, M.: Bubbles, drops, and particles, vol. 3. Academic press New York (1978)

[4] Coldep: [Online]
http://www.coldep.com/

[5] Festaud, J., Turchet, F.: Étude d'un air-lift. LMFA INSA de Lyon (2012)

[6] INSA, IFREMER: Process and installation for treating an aqueous effluent for the purpose of extracting at least one dissolved gaseous compound therefrom; Application to aquaculture in a recirculated aqueous environment. Patent: WO 2008006950 PCT/FR2007/000920 (2008)

[7] Narvaez, C.: Etude d'un nouveau procédé multifonctionnel de traitement des effluents aqueux : La colonne à dépression. LMFA (2010)

[8] Pahaut, J.: Etude des échanges gazeux dans une colonne à bulles. LMFA INSA de Lyon (2013)

[9] Transition-energetique: Biogaz et biométhane - Débat national sur la transition énergétique. [Online]
www.transition-energetique.gouv.fr/

[10] Zimmermana, W.B., Zandib, M., Bandulasena, H.H.C. *et al.*: Design of an airlift loop bioreactor and pilot scales studies with fluidic oscillator induced microbubbles for growth of a microalgae Dunaliella salina. Elsevier applied energy **88**(10), 3357–3369 (2011)

# Part II

# Micro-Bubbles Generators

# Chapter 3

# Bubbles and Micro-Bubble Generation

*L'aire interfaciale entre la phase gazeuse et la phase liquide est un facteur crucial pour le transfert de masse dans les colonnes à bulles (voir Chapitre 2). L'échange moléculaire entre un volume donné de dioxyde de carbone et l'eau (voir équation 1.2) peut être amélioré par la formation de bulles plus petites, menant à une plus grande interface gaz-liquide. Ce chapitre présente les divers phénomènes physiques s'appliquant aux bulles, ainsi que les nombres adimensionnels associés. Un État de l'Art des Générateurs de Micro-Bulles (MBG) est ensuite exposé, présentant des systèmes utilisant divers phénomènes tels que la cavitation, l'électrolyse, ou le cisaillement.*

# Abstract

As discussed previously in Chapter 2, the interfacial area between the gas phase (i.e. bubbles) and the liquid phase (i.e. water) is a crucial factor for mass transfer in bubble columns. The molecular exchange between carbon dioxide and water (see equation 1.2) can be improved by creating smaller bubbles, leading to a larger gas-liquid interface. This chapter describes the various physical phenomena that apply to bubbles, and the associated dimensionless numbers. A State of the Art Micro-Bubbles Generators(MBG) is then exposed, with systems using various phenomena such as cavitation, electrolysis, or shearing.

# Nomenclature

### Greek symbols

| | |
|---|---|
| $\gamma$ | Surface tension, $[\frac{\mathrm{N}}{\mathrm{m}}]$ |
| $\omega$ | Rotating velocity, $[\frac{rad}{s}]$ |
| $\mu$ | Dynamic viscosity, $[\frac{kg}{m \cdot s}]$ |
| $\nu$ | Kinematic viscosity, $[\frac{m^2}{s}]$ |
| $\rho$ | Density, $[\frac{\mathrm{kg}}{\mathrm{m}^3}]$ |
| $\tau$ | Shear stress, $[Pa]$ |

### Latin symbols

| | |
|---|---|
| $A$ | Area, $[m^2]$ |
| $D$ | Diameter, $[m]$ |
| $D_{bubble}$ | Bubble diameter, $[m]$ |
| $D_{inj}$ | Injector diameter, $[m]$ |
| $Eo$ | Eötvös number, [ ] |
| $F_{centrifugal}$ | Centrifugal forces, $[N]$ |
| $g$ | Gravitational acceleration, $[\frac{\mathrm{m}}{\mathrm{s}^2}]$ |
| $m$ | Mass of a bubble, $[kg]$ |
| $Mo$ | Morton number, [ ] |
| $n$ | Number of sphere, [ ] |
| $Q$ | Flow rate, $[\frac{\mathrm{m}^3}{\mathrm{s}}]$ |
| $R$ | Distance from the rotation axis to the center of gravity of the bubble, $[m]$ |
| $Re$ | Reynolds number, [ ] |
| $U$ | Velocity of the bubble, $[\frac{\mathrm{m}}{\mathrm{s}}]$ |
| $u$ | Velocity of the fluid along the boundary, $[\frac{\mathrm{m}}{\mathrm{s}}]$ |
| $V$ | Volume, $[m^3]$ |

| | |
|---|---|
| $y$ | Distance to the boundary, $[m]$ |

**Subscripts**

| | |
|---|---|
| *big* | Big bubble, |
| $g$ | Gas, |
| $l$ | Liquid, |
| *small* | Small bubble. |

## 3.1 Physics of bubbles

### 3.1.1 Forces applied to bubbles

A bubble may be subjected to various forces. Dynamic pressure forces due to the movement of the bubble in the liquid depend on the characteristics of the flow and the fluid in which this flow occurs (velocity, density and viscosity of the fluid, bubble size). As discussed in Section 1.4, these forces are also sensitive to contamination.

Forces of static pressure (hydrostatic pressure) are applied to the bubble as it is placed within the liquid. The surface tension forces are caused by the presence of an interface between two phases (liquid-gas). In [4], Brennen provides the following explanation:

> "In a pure liquid, surface tension is the macroscopic manifestation of the intermolecular forces that tend to hold molecules together and prevent the formation of large holes. "

In pure water, the surface tension $\gamma$ has a value of $71.97 \times 10^{-3}\ N/m$ at $20°C$ [11]. Adding surfactants (i.e. surface active agents) modifies interfacial tension which can be useful for applications like cleaning, wetting and foaming processes. The surface tension tends to stabilize the spherical shape of the bubbles whereas forces of inertia, gravity and viscosity contribute to deformation.

The upward movement of a bubble is mainly due to the buoyancy force that is equal to the weight of displaced fluid, and thus depends on the gas and liquid densities. It is a vertical force opposed to the gravity weight.

Drag forces are due to fluid resistance (friction) and are opposed to rising motion. In [15], Rastello *et al.* study these drag forces applied to a small bubble spinning in equilibrium in a contaminated fluid.

In the special case of a diffuser in rotation (see Section 4), the bubble that remains attached to the outlet aperture is subject to centrifugal forces $F_{centrifugal}$:

$$F_{centrifugal} = m \times \omega^2 \times R$$

where $m$ is the mass of the bubble (kg), $\omega$ is the rotational velocity (rad/s), and $R$ is the distance from the rotation axis to the center of gravity of the bubble (m).

A bubble is also subjected to shearing forces at the interface between the output aperture and the bubble. For a Newtonian fluid, the shear stress $\tau$ applied at distance y is equal to:

$$\tau(y) = \mu \times \frac{du}{dy} \tag{3.1}$$

where $\mu$ is the dynamic viscosity ($kg/(m \cdot s)$), $u$ is the velocity of the fluid along the boundary (m/s) and $y$ is the distance to the boundary (m).

The kinetic energy given by the motion of a bubble to the surrounding liquid adds a drag force that had been studied by Brennen in [3]. Output gas flow is driven out of the needle and also contributes to the detachment of the bubble.

### 3.1.2 Dimensionless numbers and shapes

Dimensionless numbers are commonly used to characterize phenomena independently from any physical dimension. This enables easy change of scale. It is possible to compute dimensionless numbers to characterize the flow.

As represented by Clift, Grace and Weber [6] in Figure (2.5), bubble shapes can be divided in categories depending on the value of two dimensionless criteria: the Reynolds and Eötvös numbers.

The Reynolds number is the ratio of fluid inertial and viscous forces:

$$Re = \frac{U.D_{bubble}}{\nu}$$

where $U$ is the bubble velocity ($m/s$), $D_{bubble}$ is the bubble diameter ($m$) and $\nu$ is the kinematic viscosity of the liquid ($m^2/s$).

The Eötvös number is the ratio of buoyancy force divided by surface tension force (also known as the Bond number):

$$Eo = \frac{(\rho_l - \rho_g).{D_{bubble}}^2.g}{\gamma}$$

where $\rho_l$ and $\rho_g$ are the liquid and gas densities, $g$ is the gravitational acceleration ($m/s^2$), and $\gamma$ is the surface tension ($N/m$).

The growth of bubble diameter increases Reynolds and Eötvös numbers, leading to regime change. For air bubbles rising freely into water, limits are:
- $Re < 1$ and $Eo < 1$: spherical bubbles ;
- $1 < Re < 1000$ and $1 < Eo < 50$: ellipsoidal bubbles ;
- $Re > 1000$ and $Eo > 50$: bubbles in the form of spherical caps.

In air-water systems, $log(Mo) = -10,6$ where $Mo$ stands for the Morton number which is another dimensionless number used to characterize bubble shapes:

$$Mo = \frac{(\rho_l - \rho_g).\mu^4.g}{\gamma^3.\rho_l^2}$$

Based on Krishna and Van Baten [10], Figure (3.1) shows the Eötvös and Reynolds values of bubbles experimentally observed during this thesis. As predicted, they are positioned along the isovalue line $log(Mo) = -10,6$.

In air-water systems, and under atmospheric pressure, micro-bubbles are spherical. Bubbles of diameter close to 9 $mm$ are bean-shaped, while those with a size around 12 $mm$ are winged. Spherical cap form is adopted by bubbles larger than 20 $mm$. Depending on the shape of the bubbles, the upward trajectory may be different.

### 3.1.3 Bubble movement

The rising of small bubbles is oscillatory. The more the size increases, the more vertical the trajectory is.

Bubbles with a large diameter (more than 20 $mm$) are considered to rise vertically, as explained by Krishna and Van Baten in [10]:

> "When the bubble size increases to 15.5 $mm$, these vertical oscillations of the edges vanish and the bubble moves more or less in a vertical line."

A 2D trajectory is more simple than 3D. Thus, to be compared with 2D numerical models presented in [19], the phenomena experimentally observed in Section 5 involved a large bubble whose trajectory was vertical.

As reported in Clift, Grace and Weber [6], free rising bubble velocity depends on the bubble diameter and the contamination level of the water (see Section 1.4). Experimentally measured rising bubble velocities are reported in Figure (5.8). For small diameters $D_{bubble} < 2\ mm$, velocity increases with increasing diameter for both contaminated and pure water.

Reducing bubble diameter results in lower rising velocity. Thus bubbles need more time to move upward to the top of a bubble column. By dropping the diameter from $D_{bubble} = 2\ mm$ to $0.2\ mm$, the rising velocity is divided by 15, enhancing retention time and therefore mass transfer through the gas-liquid interface.

The diameter of the bubbles generated by an output depends on the injection conditions (inner pressure), the type of diffuser and the fluid properties (surface tension, viscosity, density).

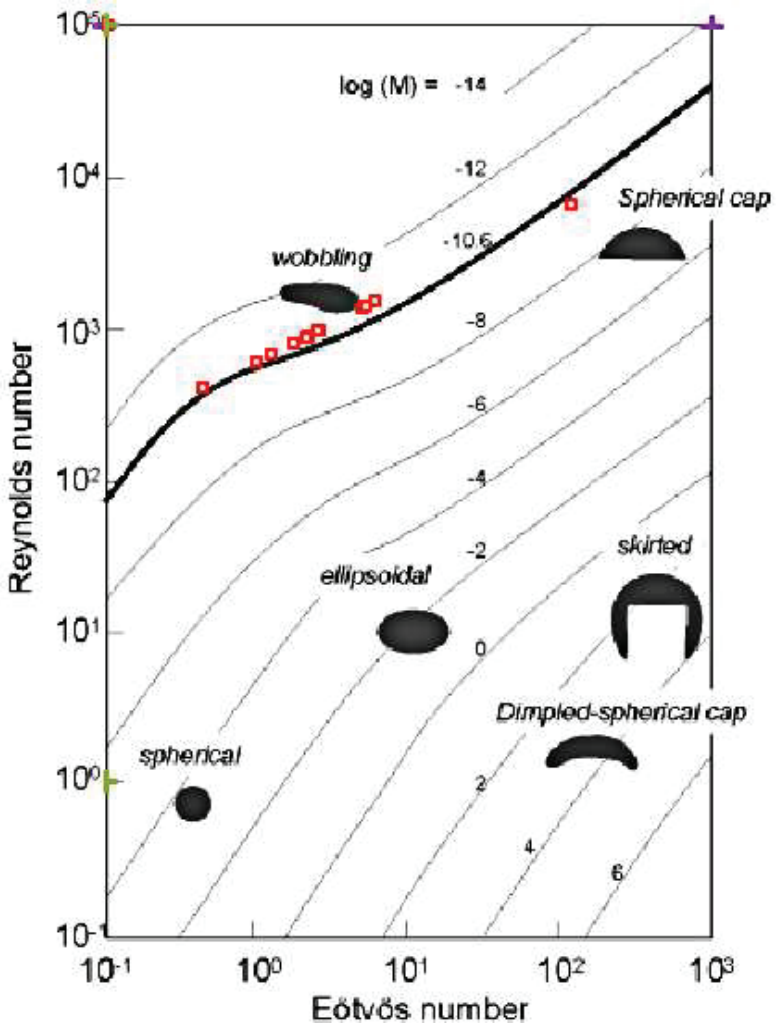


Figure 3.1: Experimental Reynolds and Eötvös numbers of free rising bubbles are shown in red squares. According to theory, they are along Morton's line corresponding to air-water systems. This figure is based on the paper of Krishna and Van Baten [10], representing bubble shapes by region.

### 3.1.4 Bubbling regimes

At low gas flow rate, with a static diffuser in a static medium, bubble sizes are determined by the geometry of the injector, through the diameter of its aperture. From Barrut [2], the balance between surface tension and buoyancy leads to the following formula:

$$D_{bubble} = \sqrt[3]{\frac{6\gamma D_{inj}}{g\Delta\rho}}$$

where $D_{bubble}$ is the bubble diameter $(m)$, $\gamma$ is the surface tension $(N/m)$, $D_{inj}$ is the injector diameter $(m)$, $g$ is the gravitational acceleration $(m/s^2)$, and $\Delta\rho$ is the difference of gas and liquid densities $(kg/m^3)$.

For high-rate gas flows, the bubble diameters in the output aperture are controlled by the balance between buoyancy and inertial forces:

$$D_{bubble} = \left(\frac{36Q_{gas}^2}{g\pi^2}\right)^5$$

where $Q_{gas}$ is the injected gas flow rate $(m^3/s)$.

The structure of the gas flow depends on the shape of bubbles and the intensity of bubbling. In the case of a static bubble generator with several outputs, one can consider three bubbling regimes:
- The unique bubbling regime, which corresponds to low gas flow rates: bubbles are formed one by one from the aperture which has the largest diameter and the bubble generator functions as a generator with one output ;
- The alternating unique bubbling regime, which corresponds to moderate gas flow rate: bubbles pop out alternatively from all ports regardless of their diameter, and increasing the gas flow rate increases the frequency of bubble formation from the various ports ;
- The simultaneous bubbling regime, which corresponds to high-rate gas flows: bubbles appear from all ports simultaneously and coalescence appears if the contact time between bubbles is long enough to break the liquid film [9]. Coalescence of bubbles during their rise may also be important because of a higher probability of collision.

Formation phenomena of bubbles from a diffuser have a direct influence on the flow regimes in a bubble column (see Section 1.2).

### 3.1.5 Small bubbles

As mass transfer is proportional to interfacial surface area (see equation 1.9), larger interfaces will result in higher efficiency for gas/liquid mass transfer in bubble columns.

A unique sphere circumscribed in a cubic volume has a surface 2 times smaller than 8 spheres in cubic arrangement (2*2*2 matrix).

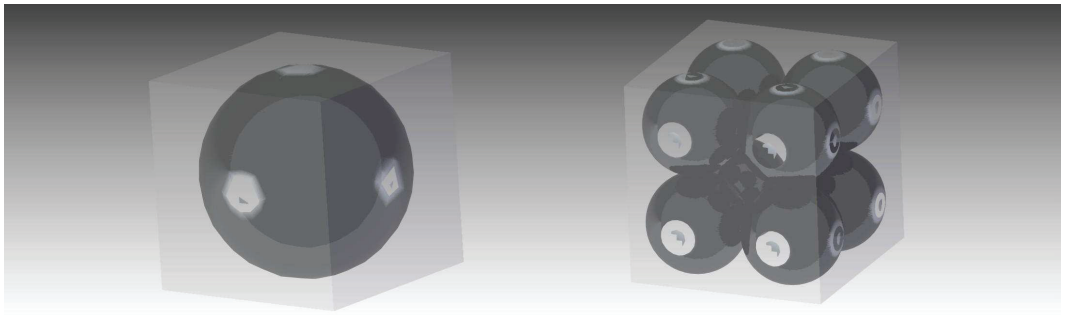

Figure 3.2: A unique sphere circumscribed in a cubic volume and a matrix of 8 spheres in cubic arrangement contained in a cubic volume.

It is easy to show that a n*n*n matrix of small spheres in cubic arrangement has a surface area n times bigger than the unique sphere circumscribed in the same cubic volume:

$$A_{unique\ sphere} = \pi * {D_{bubble}}^2$$

$$A_{n*n*n\ matrix\ of\ small\ spheres} = n^3 * \pi * (\frac{D_{bubble}}{n})^2$$

$$\frac{A_{unique\ sphere}}{A_{n*n*n\ matrix\ of\ small\ spheres}} = 1 : n$$

The art of arrangements in lattices is studied in crystallography [20] and mineralogy [18]. The highest Atomic Packing Factor (APF) for equal-sized atoms is 0.74, obtained for Face-Centered Cubic (FCC) and Hexagonal Close-Packed (HCP) arrangements.

Another way to present the interest of small bubbles can be given. The following demonstration shows that for a same gas volume $V$, bubble diameter ratio $D_{big}/D_{small}$ is equal to bubble area ratio $A_{big}/A_{small}$:

$$V_{big} = \frac{4\pi}{3} * (\frac{D_{big}}{2})^3$$

$$V_{small} = \frac{4\pi}{3} * (\frac{D_{small}}{2})^3$$

At constant volume, the number of small bubbles is:

$$n = \frac{V_{big}}{V_{small}} = (\frac{D_{big}}{D_{small}})^3$$

$$A_{big} = \pi * {D_{big}}^2$$
$$A_{small} = \pi * {D_{small}}^2$$
$$n \times A_{small} = (\frac{D_{big}}{D_{small}})^3 \times \pi * {D_{small}}^2 = (\frac{D_{big}}{D_{small}}) \times \pi * {D_{big}}^2$$
$$n \times A_{small} = (\frac{D_{big}}{D_{small}}) \times A_{big}$$

i.e., at constant volume of gas, the surface area of 1 $mm$ diameter bubbles is 10 times larger than the surface area of 10 $mm$ diameter bubbles.

Therefore, in a defined volume and at a defined void fraction, smaller bubbles will result in larger surface areas, that is to say in improved mass transfer. Void fraction in a gas-liquid flow is defined as the fraction of the volume that is occupied by the gas phase (3D), or the fraction of the channel cross-sectional area that is occupied by the gas phase (2D).

Several authors demonstrate the interest of small bubbles in their respective scope. In [4], Brennen reports that "in water, micro-bubbles of air seem to persist almost indefinitely and are almost impossible to remove completely". For the mineral flotation process [7], Formanek gives the following analysis :

> "Pour un mm volume d'air introduit on a d'autant plus de bulles que celle-ci sont petites. Les bulles seront plus petites et les collisions plus nombreuses si on augmente la turbulence dans la pulpe. La bulle doit etre animee d'une certaine vitesse pour pouvoir franchir et detruire la couche hydratée qui enveloppe le solide. Le temps de contact decroit avec le diam des particules et des bulles. Il y a donc interet à produire des fines bulles. Les petites bulles se deforment moins que les grosses et resistent mieux aux forces d'arrachement dynamiques qui existe dans une machine de flotation. "

Muroyama *et al.* [14] studied micro-bubble mass transfer and found that they had "superior characteristics in terms of physical chemistry and size effects". In [13], Motarjemi and Jameson explain that for higher oxygenation yield, a system producing smaller bubbles is required:

> "[...] existing processes making bubbles greater than 2 $mm$ in diameter are bound to be very inefficient unless the liquid depth is greater than about 10 $m$. The results show clearly that in order to achieve high Oxygen utilization efficiencies, it is necessary to use bubbles which are much smaller than made in established technology"

Therefore, in many fields, it is necessary to generate small bubbles. Several solutions have been proposed to meet this need.

## 3.2 Micro-Bubble Generator state of the art

Micro-Bubble Generators (MBG) operate on the basis of various phenomena. The present author had the opportunity to attend the *16th International Symposium on Applications of Laser Techniques to Fluid Mechanics* from 9 to 12 July 2012, in Lisbon. The Calouste Gulbenkian Foundation welcomed over 250 participants, 200 presentations and a dozen manufacturers. Yet, Micro-Bubble Generators presented were not able to inject large amounts of gas in the form of very small bubbles.

It is possible to create very small bubbles by electrolysis [17] but flow rates are low and electrodes are expensive. Gas dissolved in the medium can be released in micro-bubbles by cavitation, as DynaSwirl MBG which is based on the patent [5] and pictured in Figure (3.3) (bubble diameter from 0.05 to 0.3 $mm$).

Figure 3.3: Picture of the DynaSwirl MBG.

Nevertheless, these systems only extract the dissolved gas from the liquid, while our goal is to sequestrate $CO_2$ in water (see Section 1.1.2).

In recent works [1, 21], fluidic oscillators have been used to inject $CO_2$ in micro-algae bioreactors. These oscillators have no moving parts and are able to produce bubbles of the scale of a pore.

The current diffusers used by COLDEP (see Section 1.1.3) are in porous ceramic. They can produce bubbles whose diameter can get down to 0.46 $mm$ at very low flow rate. Yet at usual flow rate, coalescence creates much bigger bubbles (2.75 $mm$ for new differs), reducing the gas-liquid interfacial area and therefore the mass transfer.

A patent from Sadatomi and Kawahara [16] uses the venturi effect to accelerate the fluid and shear gas into micro-bubbles. This system requires gas flow and

liquid flow. This patent has been enhanced by a screw enabling thin regulation of the chamber space [12].

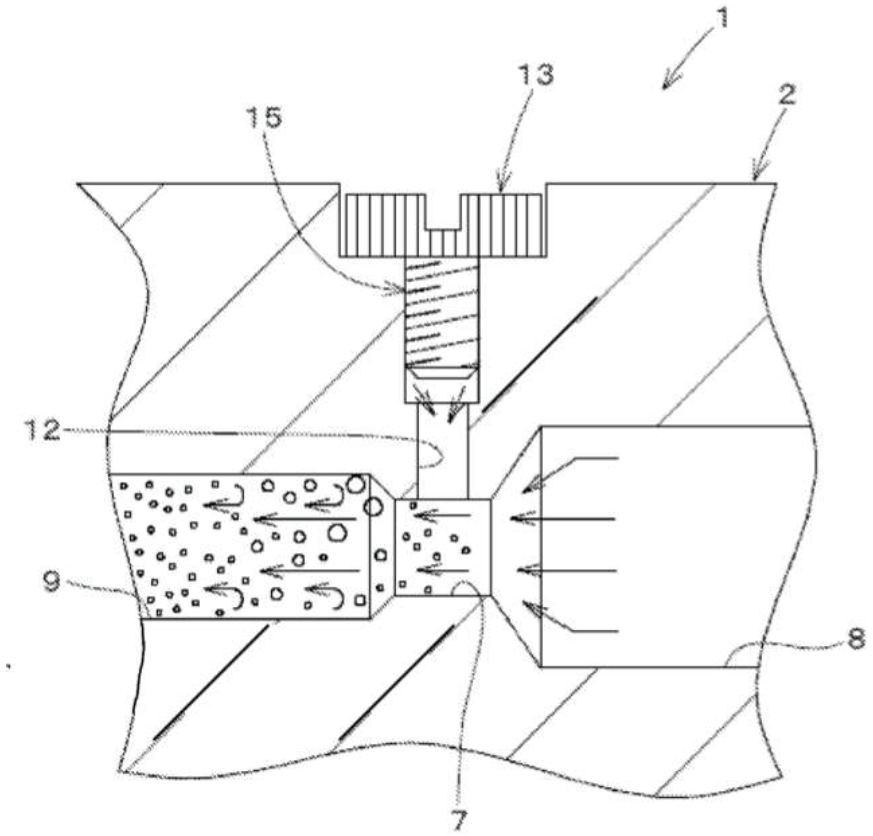


Figure 3.4: Picture of the Venturi MBG from Sadatomi and Kawahara [16].

A US patent published in 1980 [8] mentions a system using a large diffusive disk in rotation. The rotational movement shears bubbles that escape from the crevices of the disk surface, leading to bubble with a diameter $D_{bulle} = 1$ to $3\ mm$.

## 3.3 Conclusion on the need for innovation

In spite of a large number of apparatus, State of the Art reveals a lack of efficient solutions to the production of micro-bubbles. MBG are either expensive, energy consuming, or have low gas flow rate. The following chapter presents the conception and the characterization of a new experimental device designed to produce

small bubbles.

# Bibliography


[1] Al-Mashhadani, M.K.H., Hemaka Bandulasena, H.C., Zimmerman, W.B.: CO2 Mass Transfer Induced through an Airlift Loop by a Microbubble Cloud Generated by Fluidic Oscillation. Industrial & Engineering Chemistry Research, 51 **4**, 1864–1877 (2012)

[2] Barrut, B.: Study and optimization of a vacuum airlift: Application to aquaculture. Université Montpellier 2, Ph.D. Thesis (2011)

[3] Brennen C.E.: A review of added mass and fluid inertial forces, Report Number CR 82.010, Naval civil engineering laboratory (1982)

[4] Brennen, C.E: Cavitation and bubble dynamics. Oxford university press, ISBN 0-19-509409-3 (1995)

[5] Chahine, G.L., Kalumuck, K.M.: Swirling Fluid Jet Cavitation Method and System for Efficient Decontamination of Liquids.
Patent: US 6221260 B1 (2001)
http://www.dynaflow-inc.com/Products/Bubbly/bsep.htm

[6] Clift, R., Grace, J., Weber, M.: Bubbles, drops, and particles, vol. 3. Academic press New York (1978)

[7] Formanek V. : Quelques aspects theoriques, techniques et economiques du procede de flottation. MINEMET RECHERCHE (1978)

[8] Hise, R.E.: Ultra-thin rotating disk gas diffuser (and bubble shearing method employing the same).
Patent: US 173631 (1980)

[9] Huang, Z.: Efficacité de Capture dans les Procédés de Flottation. Université de Toulouse, Ph.D. Thesis (2009)

[10] Krishna, R., Van Baten, J.M.: Simulating the Rise Characteristics of Gas Bubbles in Liquids Using CFD Chemical Engineering Technology **24**(4) (2001)

[11] Lange's Handbook of Chemistry. 10th edition pp 1661–1665 (1967)

[12] Mori, Y.: Micro-bubble generator.
Patent: US 0214436 A1 (2013)

[13] Motarjemi, M., Jameson, G.J.: Mass transfer from very small bubbles - the optimum bubble size for aeration Chemical Engineering Science **33** 1415–1423 (1978)

[14] Muroyama, K. *et al.*: Mass transfer properties in a bubble column associated with micro-bubble dispersions Chemical Engineering Science **100** 464–473 (2013)

[15] Rastello, M., Marie, J-L., Grosjean, N., Lance, M.: Drag and lift forces on interface-contaminated bubbles spinning in a rotating flow. Journal of Fluid Mechanics **682** pp 434–459 (2008)

[16] Sadatomi, M., Kawahara,A.: Fluids mixer and fluids mixing method. patent: JP 173631 (2008)

[17] Satake, S.,*et al.*: Three-dimensional simultaneous measurements of a rising microbubble position and flow surrounding the microbubble by a digital hologram. 16th International Symposium on Applications of Laser Techniques to Fluid Mechanics, Lisbon, Portugal (2012)

[18] Schubnel, H.J.: Je découvre les minéraux. Collection Agir et Connaitre (1978)

[19] Valiorgue, P.: Mass transfer in intermittent horizontal gas-liquid flow and application to photobioreactors. Université Lyon 1, Ph.D. Thesis (2012)

[20] Vinothan *et al.*: Dense Packing and Symmetry in Small Clusters of Microspheres. Science **301** p438–487 (2003)

[21] Zimmermana, WB., Zandib, M., Bandulasena, H.H.C. *et al.*: Design of an airlift loop bioreactor and pilot scales studies with fluidic oscillator induced microbubbles for growth of a microalgae Dunaliella salina. Elsevier applied energy **88**(10), 3357–3369 (2011)

# Chapter 4

# Design and testing of a new Micro-Bubble Generator

*Un nouveau Générateur de Micro-Bulles a été conçu et caractérisé. Ce diffuseur rotatif de micro-bulles est capable de produire un nuage de bulles dont les diamètres peuvent être modifiés via la vitesse de rotation, elle-même contrôlée par un potentiomètre électrique. Le débit de gaz est indépendant de la vitesse de rotation, et un débit d'eau n'est pas requis pour le fonctionnement du système. Les travaux expérimentaux associés sont présentés dans ce chapitre, et attestent que le prototype est capable de produire des micro-bulles ayant un diamètre moyen* $D_{bubble} = 0.252\ mm$. *L'installation d'un tel dispositif dans les colonnes à bulles devrait conduire à une augmentation significative de l'aire interfaciale gaz-liquide, et donc du transfert de masse.*

# Abstract

An innovative Micro-Bubble Generator has been created and characterized. This new rotating micro-bubble diffuser is able to produce a cloud of bubbles. Their diameters can be modified by an electric potentiometer. Gas flow rate is independent of the rotational speed, and water flow is not required to operate the system. Associated experimental works are presented in this chapter, and attest that the prototype can produce micro-bubbles of average diameter $D_{bubble} = 0.252\ mm$. The installation of such device in bubble columns should lead to a significant increase in gas-liquid interfacial area, and thus the mass transfer.


# Nomenclature

### Greek symbols

| | |
|---|---|
| $\alpha$ | Fitting coefficient, [ ] |
| $\beta$ | Fitting coefficient, [ ] |
| $\gamma$ | Surface tension, $[\frac{\mathrm{N}}{\mathrm{m}}]$ |
| $\omega$ | Rotating velocity, $[\frac{rad}{s}]$ or $RPM$ |
| $\nu$ | Dynamic viscosity, $[\frac{m^2}{s]}$ |
| $\rho$ | Density, $[\frac{\mathrm{kg}}{\mathrm{m}^3}]$ |
| $\chi$ | Ratio of the cylindrical wall diameter to the experimental average bubble diameter, [ ] |

### Latin symbols

| | |
|---|---|
| $a_c$ | Centrifugal acceleration, $[\frac{\mathrm{m}}{\mathrm{s}^2}]$ |
| $C$ | Dynamic loading, $[N]$ |
| $C_x$ | Drag coefficient, [ ] |
| $D_{bubble}$ | Bubble diameter, $[m]$ |
| $D_{wall}$ | Internal diameter of the cylindrical wall, $[m]$ |
| $Eo$ | Eötvös number, [ ] |
| $F_a$ | Axial loading, $[N]$ |
| $F_{centrifugal}$ | Centrifugal forces, $[N]$ |
| $F_{drag}$ | Drag forces, $[N]$ |
| $F_{shear}$ | Shear force, $[N]$ |
| $f$ | Acquisition frequency, $[fps]$ |
| $L_{10}$ | Bearing life, $[hour]$ |
| $m$ | Mass of a bubble, $[kg]$ |
| $n_{set}$ | Number of images in which a same bubble rises through the acquisition window, [ ] |

| | |
|---|---|
| $p$ | Ball bearing coefficient, [ ] |
| $Q_{device}$ | Average gas flow rate of the device, $[\frac{\mathrm{m}^3}{\mathrm{s}}]$ |
| $R$ | Radial loading, $[N]$ |
| $R_{horizontal}$ | Measured horizontal radius of the bubble, $[m]$ |
| $R_{vertical}$ | Measured vertical radius of the bubble, $[m]$ |
| $Re$ | Reynolds number, [ ] |
| $R_\omega$ | Rotational Reynolds number, [ ] |
| $r$ | Eccentric distance, $[m]$ |
| $r_{bent}$ | Distance from the tip of the bent needle to the axis of rotation (original axis of the needle), $[m]$ |
| $U_{tip}$ | Needle tip velocity, $[\frac{\mathrm{m}}{\mathrm{s}}]$ |
| $V$ | Volume, $[m^3]$ |
| $v$ | Relative velocity of the bubble in the water flow, $[\frac{\mathrm{m}}{\mathrm{s}}]$ |
| $S_{ref}$ | Projected frontal area of the bubble (reference area), $[m^2]$ |
| $S_{tip}$ | Interface between the needle and the bubble, $[m^2]$ |
| $T_{tip}$ | Surface tension force between the needle and the bubble, $[N]$ |

**Subscripts**

| | |
|---|---|
| $g$ | Gas, |
| $l$ | Liquid. |

## 4.1 Introduction

In order to fulfil the need for micro-bubble generators (see Section 3.1.5), a scientific approach has been conducted. A set of specifications has been established, and with knowledge of the state of the art, a new system has been created that would detach the bubble from the diffuser promptly. A method of inquiry based on empirical observations and measurable data has been carried out and is reported in Section 4.5. Current Section presents the adopted solution, which is able to deliver adjustable amount of energy to overcome the surface tension and release micro-bubbles.

## 4.2 Required functions and specifications

In order to provide a guide line and choose compatible solutions, a list of design specifications and required functions has been written:
- high speed rotating motor and transmission ;
- high speed rotating airflow diffuser ;
- stability ;

- efficient sealing for airflow control ;
- rotating sealing (heat, pressure) ;
- concentric walls with interchangeable diameters ;
- interchangeable diffusers ;
- drain ;
- visual access for camera recordings ;
- corrosion resistance in aqueous and acidic media.

## 4.3 Solutions

The device principle is based on the shearing of bubbles exiting needle aperture. This needle is connected via a transmission tube to a high-speed rotating motor. Gas input is supplied through a chamber that communicates with the transmission tube.

### 4.3.1 Tank

A transparent tank is fixed to an aluminium base (Dural 2017). Sealing is provided by O-rings mounted in static axial compression. Water can be easily removed from the tank by a drain in the aluminium base.

Following Eriks' manufacturer specifications [2], the 2 $mm$ diameter seals are housed in a groove of 1.51 $mm$ depth and 2.90 $mm$ width. The higher pressure being internal, the seals are abutted against the external edges. This type of sealing is used between the chamber and the base, and between the base and the transparent tank.

To prevent corrosion from water and carbonic acids, aluminium parts are anodized, and small parts like screws and bearings are all stainless.

### 4.3.2 Cylindrical walls

Three concentric cylindrical walls of different diameters enable the experimenter to vary the volume in which the system generates flow.

These concentric walls are transparent, 400 $mm$ high and their internal diameters are respectively $D_{wall} = 94\ mm$, 142 $mm$ and 190 $mm$. Speed is maximal at the nucleating place, and minimal on the walls (assuming zero velocity at the wall). Reducing the distance from the nucleating place to the wall increases the velocity gradient, and therefore the shearing (see equation 3.1).

The visual access to the Region Of Interest (ROI) is enabled by transparent walls. A square transparent tank separates water from the outside atmosphere. The camera is perpendicular to the tank wall. The concentric walls are immersed

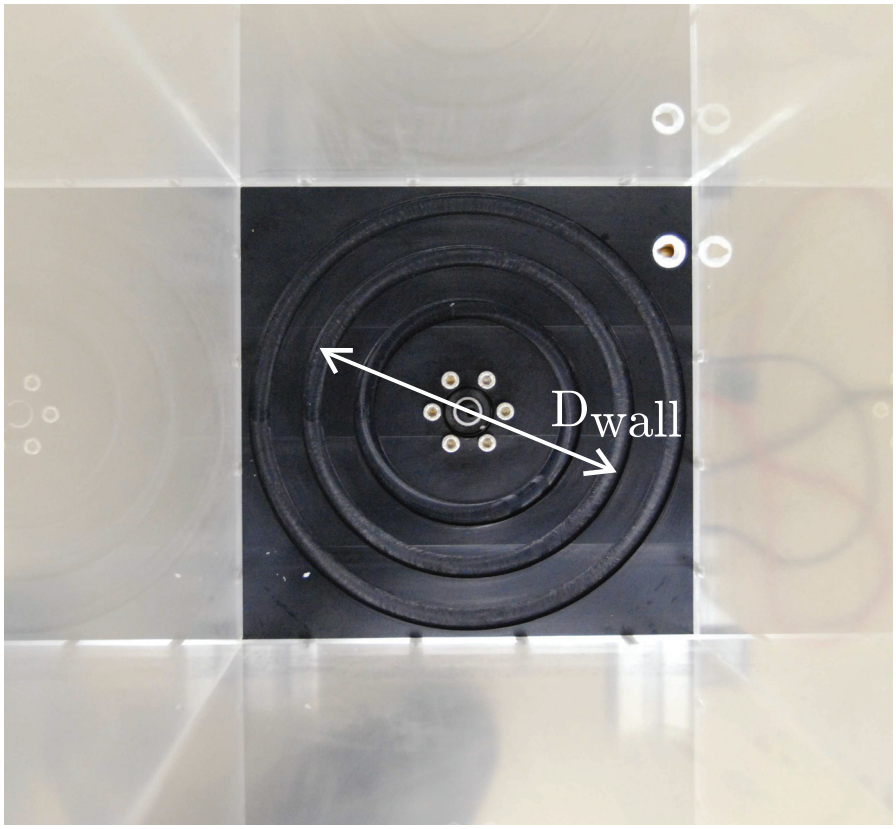


Figure 4.1: Picture of the base of the tank.

in water. Thus, according to the laws of angular deviation, no visual distortion has been observed from the ROI to the acquisition setup.

### 4.3.3 Bearings

To avoid energy loss, stability of the high-speed rotating system is crucial. Concentricity and rigidity of the rotating parts have been taken into account during the design. Pivot link between the tube and the chamber is ensured by 2 sealed bearings, mounted with a 3-point economic type assembly [1]. A spacer on the outer rings separates the 2 bearings. A clearance of 0.1 $mm$ authorizes one degree of freedom to the internal bearing ring. The assembly is clamped by a washer (clearance of 0.5 $mm$) as shown in Figure (24) in Appendix.

Two single row radial ball bearings (referenced 6000-2RS-INOX) have been selected. They have a thickness of 8 $mm$, a 26 $mm$ external diameter and a 10 $mm$ internal diameter. Since the assembly is a rotating hub mounting, bearings are clamped to the bore: external fitting $n7$, internal fitting $g6$.

The rolling element L10 bearing life has been determined using Fisher's law (4.1) from [1], in a worst case scenario where a mass $m$ of 50 $g$ is eccentric of $r = 0.01$ $m$, and rotating at $\omega = 10000$ $rpm$:

$$L_{10} = (\frac{C}{R})^p \tag{4.1}$$

where $p = 3$ for ball bearings, $C = 4620$ $N$ is the dynamic loading ($L_{10} = 1$) given by the manufacturer, and R is the radial loading. Considering no axial loading, $Fa = 0$ $N$ so $R = F_{centrifugal}$ is the worst case, where $F_{centrifugal}$ is a centrifugal force:

$$F_{centrifugal} = m \times \omega^2 \times r \tag{4.2}$$

which results in $L_{10} = 598$ $Mturns = 997$ $hours$ of life. This duration corresponds to the life at which statisticaly 90% of the bearings will still work under these conditions.

Another type of wear is described in [3], which is due to global wear resulting in an increased clearance, which depends on the conditions of the rolling surfaces and the required precision of rotation. In this model, a coefficient characterizes the area in the worst conditions of contact surfaces (e.g. lubrication, impurities). In this case, the use of an electric motor in the worst conditions leads to a service life of 700 hours.

In both cases, the service life of the bearings is sufficient for planned the experiments.

### 4.3.4 Rotating parts

Rotation is directly transmitted to the transmission tube by a thread in the motor shaft. This tube passes through the aluminium base.

Various diffusers can be attached to the rotating tube. The tests have been done with needles having an external diameter of $412 \pm 2$ $\mu m$. In static use, these needles generate bubbles of average size 2.33 $mm$, which is the closest to the average size of the bubbles generated by a ceramic diffuser: 2.75 $mm$.

Needles have been bent to study the effect on bubble shearing. Bending has been done carefully, taking care not to pinch the tube. The needles are beveled. The tip is always above when the needle is attached to the system, as shown in Figure (4.2). Needles used in Section 4.5.4 have their tip at 5 $mm$, 10 $mm$ and 13 $mm$ from the axis of rotation (which is the original axis of the needle). This distance has been called $r_{bent}$.

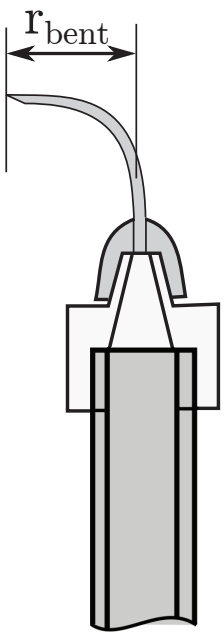


Figure 4.2: Representation of a bent needle connected to the transmission tube.

### 4.3.5 Gas input

Gas pressure can be provided by compressors or gas cylinders. A quick gas plug is set on the side of the chamber. Holes in the spacer and the transmission tube allow for the gas to flow up to the needle.

## 4.4 Retained design and realisation

The whole system has been designed using Solid Edge ST2 software. Drafts of machine parts are gathered in Appendix (.3). Exploded views of the device can be seen in Figure (4.3).

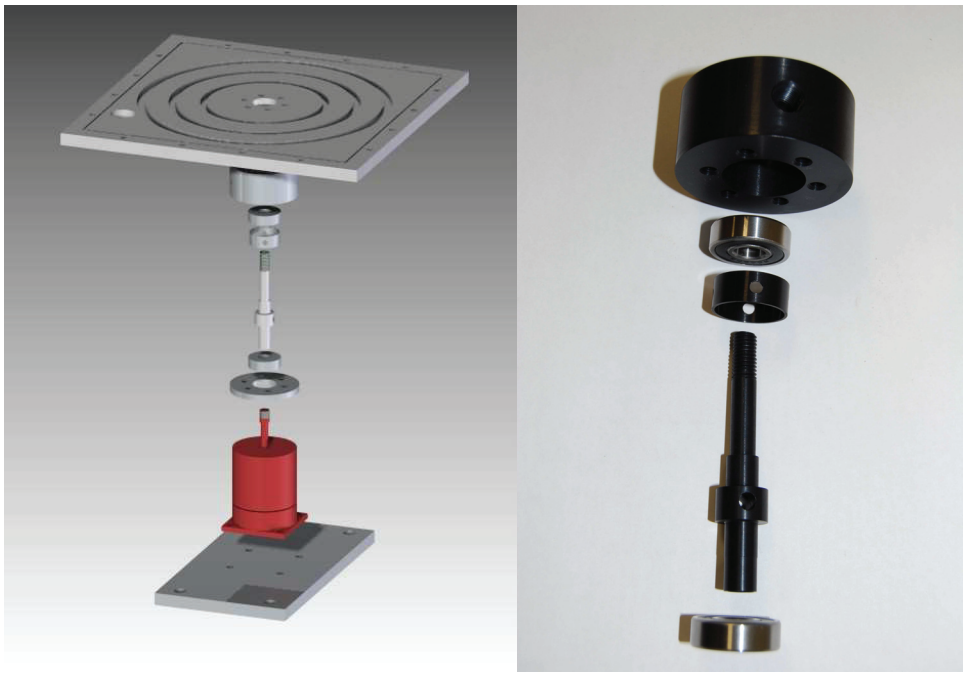

Figure 4.3: Exploded view.

As represented in picture (4.4), the electrical power is supplied by a 24 $V$ SIEMENS generator (23.8 $V$ measured). Shearing can be modified by a potentiometer (referenced: Servo Test Jamara) linked to the high speed rotating electrical motor. A higher angular velocity results in a higher shear stress as explained in equation (3.1). The potentiometer is linked to a Jamara XeTronic 100A controller that transforms Direct Current (DC) to 3-phase Alternating Current (AC). The selected motor is a Jamara A4130/6 (see Figure (4.5)), with the following characteristics:

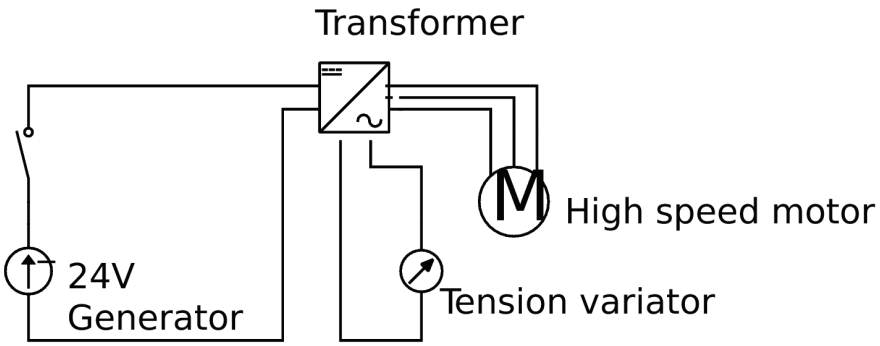


Figure 4.4: Electrical circuit.

Rpm/V: 510 (606 measured)
Internal resistance: 0.051Ω
No-load current: 2.4 $A$
Max A: $70A/60\ S$
Shaft Diameter: 6 $mm$
Dimensions: $50 \times 65\ mm$
Power: 1400 $W$
Application: 6000 $g$
Weight: 400 $g$

Maximum power of the motor is 1400W. Based on the price of electricity used in France in 2013 by EDF (€$0.12/kWh$), one hour of use would cost a maximum of €0.168.

The rotating speed of the motor has been controlled by an optical tachometer. It has been found that the real Rpm/V value of the motor is higher than manufacturer specifications, as shown in graph (4.6):

## 4.5 Experimental study of the system capacities

The system presented in the previous section has been built and tested empirically. The first part of the experimental campaign is focused on the flow study. Then bubble diameters have been measured and analyzed. These tests have been carried out in demineralized water (total hardness $< 17.8\ ppm = 1.56\ \mu S/cm$).

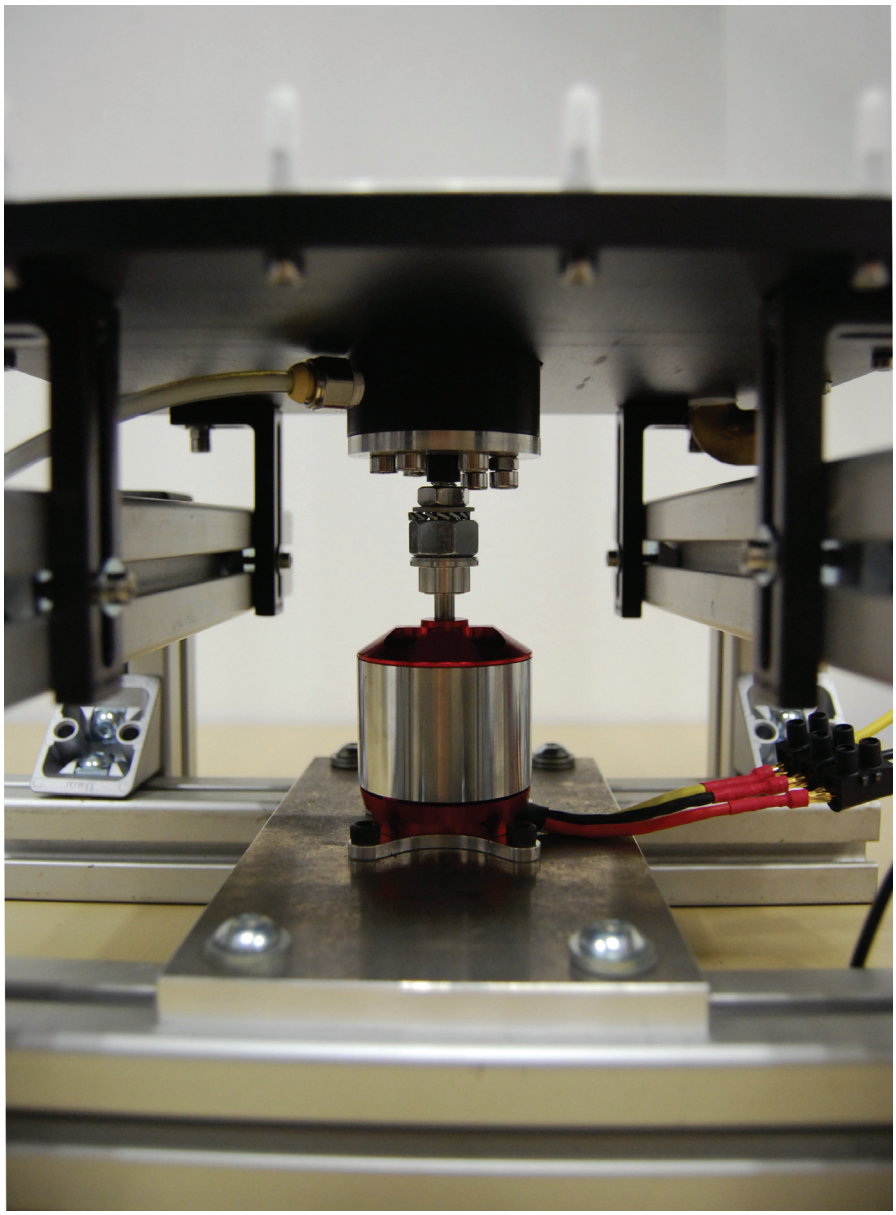

Figure 4.5: Picture of the motor and chamber.

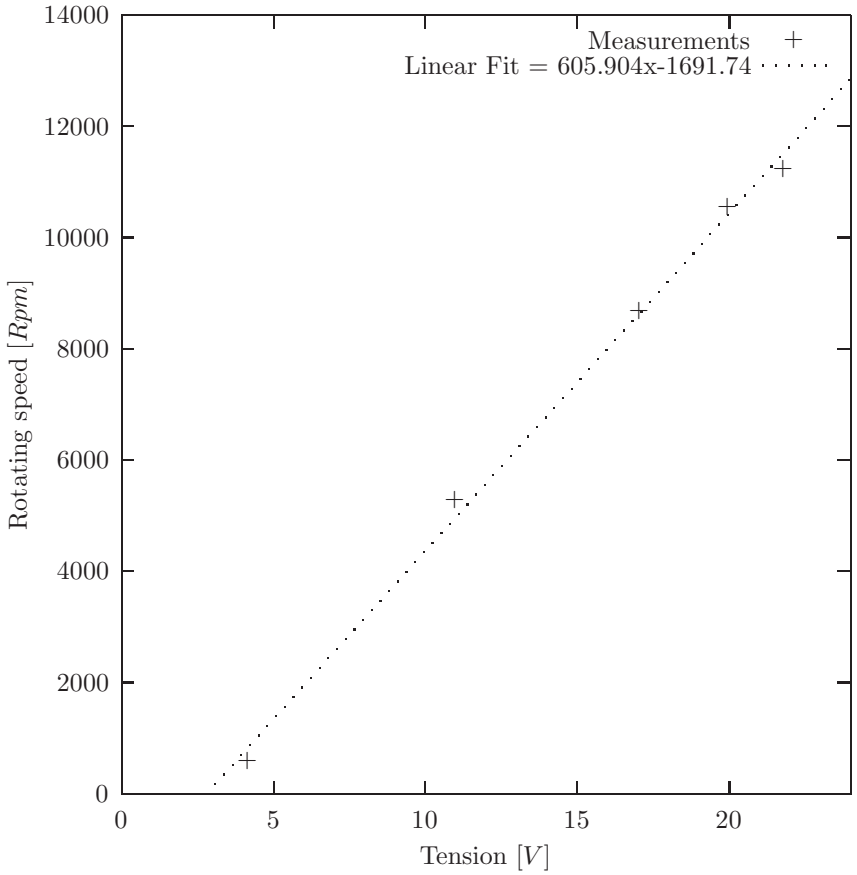


Figure 4.6: Motor rotating velocity (Rpm) versus tension (V). Measurements have been taken in the air, using an optical tachometer.

### 4.5.1 Lasers

Two lasers have been used for the experimental campaign. A frequency doubled, double pulse Nd:YAG laser from Dantec is used for PIV measurements. This light source emits monochromatic 532 $nm$ camera-synchronized pulses, with an energy of 130 $mJ$ (listed class 4 according to NF EN 60825-1).

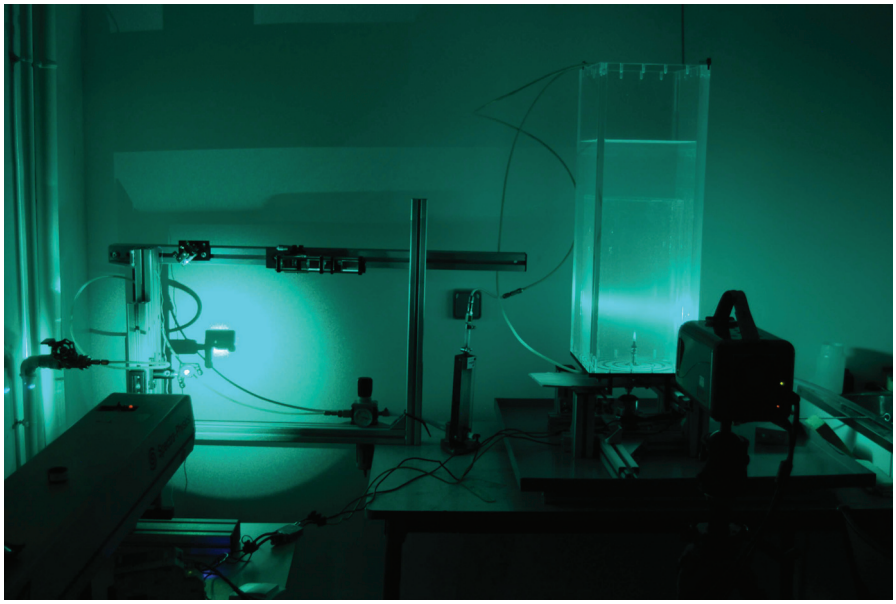

Figure 4.7: Picture of the PIV device.

PLIF and PIV experiments have been carried out with a continuous Argon laser from Spectra-Physics (stabilite 2017-04S). Able to deliver 3.2 $W$ of power, it is also a class 4 light source (skin, eye and fire hazard).

For both lasers, cylindrical lenses create a laser sheet in order to illuminate the observation area, as pictured in Figure (4.8).

### 4.5.2 Camera

The Phantom V12 CMOS camera is able to record up to 6000 single-frames per second at full resolution (1280 $\times$ 800) in 12 bits. The Phantom camera has been used both for PIV flow study (in Section 4.5.3) and bubble diameter study (see Section 4.5.4).

A LaVision scientific CMOS 16 bits camera with 1566 $\times$ 2592 resolution has been employed for PIV measurements when the Phantom V12 was not available.

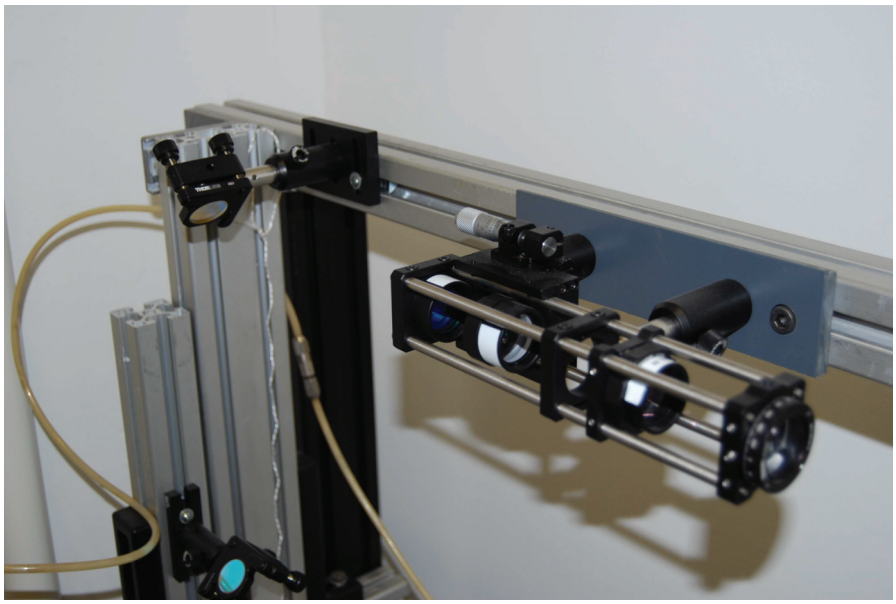

Figure 4.8: The optical system, that includes laser, mirrors, filters, and lenses.

Double-frame acquisition and software compatibility made it convenient for PIV processing.

### 4.5.3 Flow study with operating rotating diffuser

#### Rotation velocity

Electric motor rotation is driven by a potentiometer and controlled by a tachometer as reported in Section 4.4. Table (4.1) resumes the specific velocities (in $RPM$ and $rad/s$) chosen for experiments. Corresponding speeds at the tip of the bent needles are also indicated.

#### PIV flow study

Particle Image Velocimetry (PIV) is based on the analysis of successive image pairs of the fluid seeded with tracers. Knowing the time between images and the displacement of the particles, it is possible to obtain the local velocities of the tracers. If seeding is done correctly (size, density, quantity, etc.), the velocity field of the flow can be obtained using inter-correlation and statistic operations.

In the following PIV experiment, region of interest was contained in a plan illuminated by an Argon laser crossing the middle of the tank (see Figure (4.9)). The software used for PIV treatment was Davis 8.1.2.

| Position | Tension(V) | RPM | rad/s | Speed (m/s) for $r_{bent}$= 5mm | 10mm | 13mm |
|---|---|---|---|---|---|---|
| Min | 4.16 | 780 | 81,681 | 0,408 | 0,817 | 1,062 |
| Pi/4 | 10.99 | 4100 | 429,351 | 2,147 | 4,294 | 5,582 |
| Pi/2 | 17.06 | 8640 | 904,779 | 4,524 | 9,048 | 11,762 |
| Pi | 19.96 | 10460 | 1095,369 | 5,477 | 10,954 | 14,240 |
| 3Pi/2 | 21.8 | 11200 | 1172,861 | 5,864 | 11,729 | 15,247 |

Table 4.1: Velocities chosen for experiments.

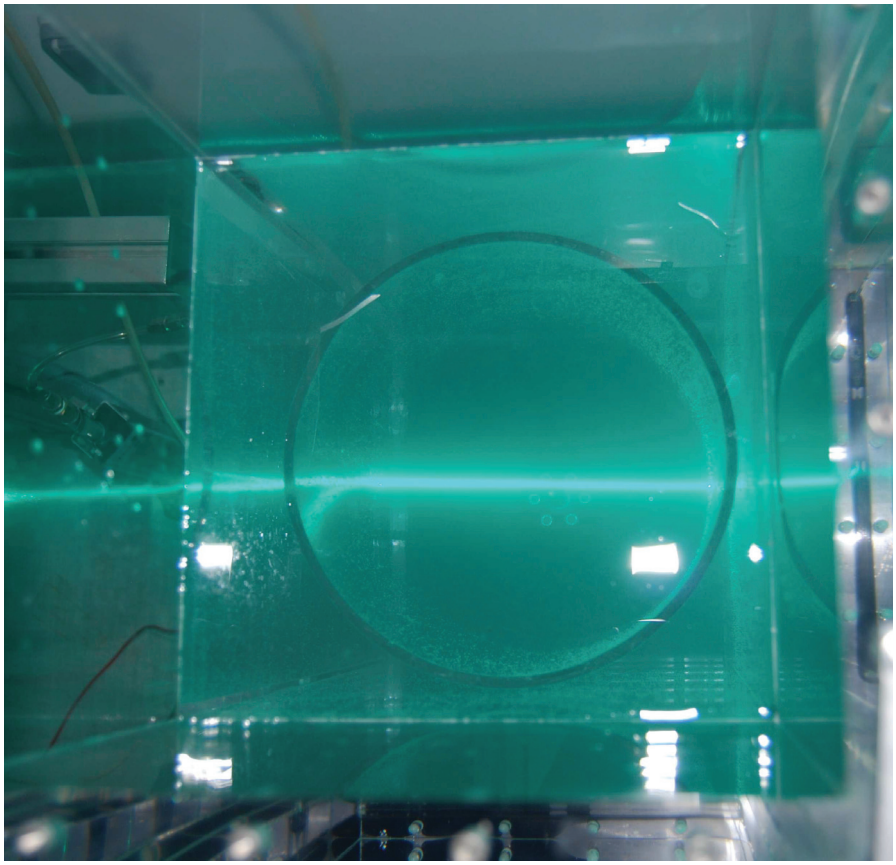

Figure 4.9: Picture of the laser plan.

In order to understand flow behaviour during the operation of the rotating diffuser, qualitative PIV flow study has been done in the tank. The 0.4 $mm$ external diameter rotating needle was not bent. It should be noted that no gas was injected during the following PIV experiments. Water was seeded with DANTEC Dynamics 10 $\mu m$ diameter Hollow Glass Spheres. Illumination was ensured by a laser plan perpendicular to the camera. Single-frame PIV has been processed using $64 \times 64$ interrogation window with 50% overlap.

PIV vectors have been obtained in the region surrounding the needle tip, where velocity is maximum. This work has been done for the 3 cylindrical walls (see Section 4.3.2), under 3 different velocities (8640, 10460 and 11200 $RPM$). Figure (4.10) presents the average velocity field of a set of 1000 images taken with the phantom camera (100 $fps$). The diffuser was rotating at $\omega = 10460$ $RPM$, in a cylindrical tube of diameter $D_{wall} = 142$ $mm$.

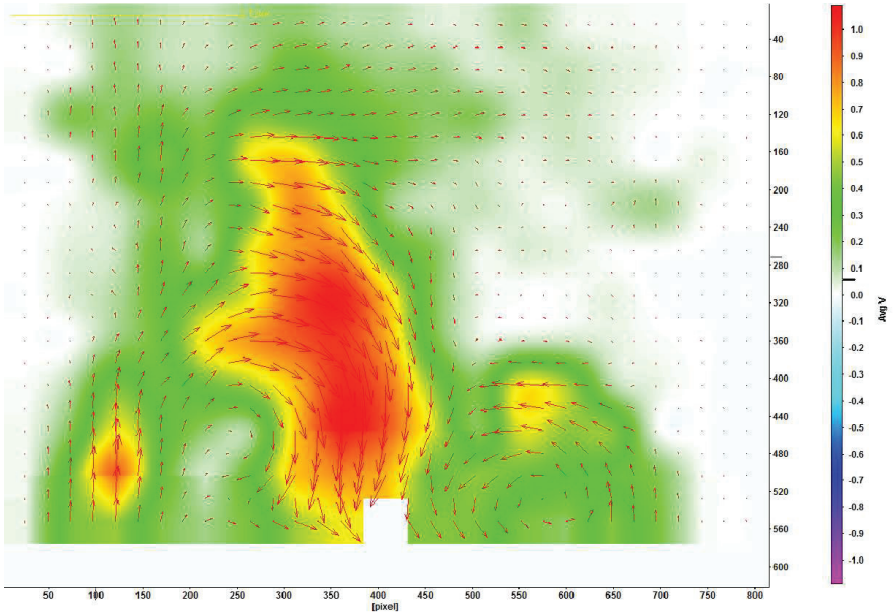


Figure 4.10: PIV flow analysis around a needle rotating at 10460 $RPM$ in a cylindrical tube of diameter 142 $mm$.

Flow rises along the walls and goes down in the center of the cylinder. Eddies are visible in areas located on the sides, below the needle. According to Bernoulli's principle and continuity equations, the high speed rotating needle locally creates low pressure that sucks water down along the axis of rotation. Due to this phenomenon, the system is able to create vortices under certain conditions. Vortex instability disrupts the symmetry of the flow.

| RPM ($rad/s$) | $D_{wall}$ ($mm$) | Water height: 500mm | 450mm | 395mm |
|---|---|---|---|---|
| 8640 | 190 | 10mm | 100mm | full length 85s |
| 10460 | 190 | 25mm | 300mm | full length 35s |
| 11200 | 190 | 20mm | 200mm | full length 35s |
| 8640 | 142 | none | none | full length 37s |
| 10460 | 142 | none | 10mm | full length 30s |
| 11200 | 142 | 45mm | none | full length 30s |
| 8640 | 94 | none | 5mm | full length 105s |
| 10460 | 94 | none | 5mm | full length 75s |
| 11200 | 94 | none | none | 250mm |

Table 4.2: Vortex formation timing.

**Vortex formation**

Depending on water height, wall diameter and needle rotating velocity, vortices may appear. The three walls have a same height of 400 $mm$. Timing and water level tests have been done in order to avoid vortex formation during regular experiments. Table (4.2) reports observed vortices in demineralized water at 24°C, with a straight 0.4 $mm$ external diameter rotating needle, without bubble gas flow. If no vortex appeared after 200 seconds of rotation, the table is filled with "none". When the vortex reaches the needle, it is filled with "full length".

In order to avoid vortex formation, water height has been fixed at 500 $mm$ for the experimental bubble diameter study.

### 4.5.4 Bubble diameter study

Using the Phantom camera mounted with a 45 $mm$ objective and 60 $mm$ extension tubes, bubble diameters have been measured in several configurations. The experimental campaign has been carried out for the 3 different cylindrical walls (see Section 4.3.2), under 3 different velocities (see Section 4.5.3), and with 3 different needles. Schematic view of the experimental set-up is given in Figure (4.12).

As explained in Section 4.3.4, needles have been bent carefully, taking care not to pinch the tube. The needles are beveled, with the tip above when the needle is attached to the system. Needles used have the tip at $r_{bent} = 5\ mm$, 10 $mm$ and 13 $mm$ from the axis of rotation, as represented in Figure (4.13).

Since no micro flow meters were available, the average gas flow rate has been

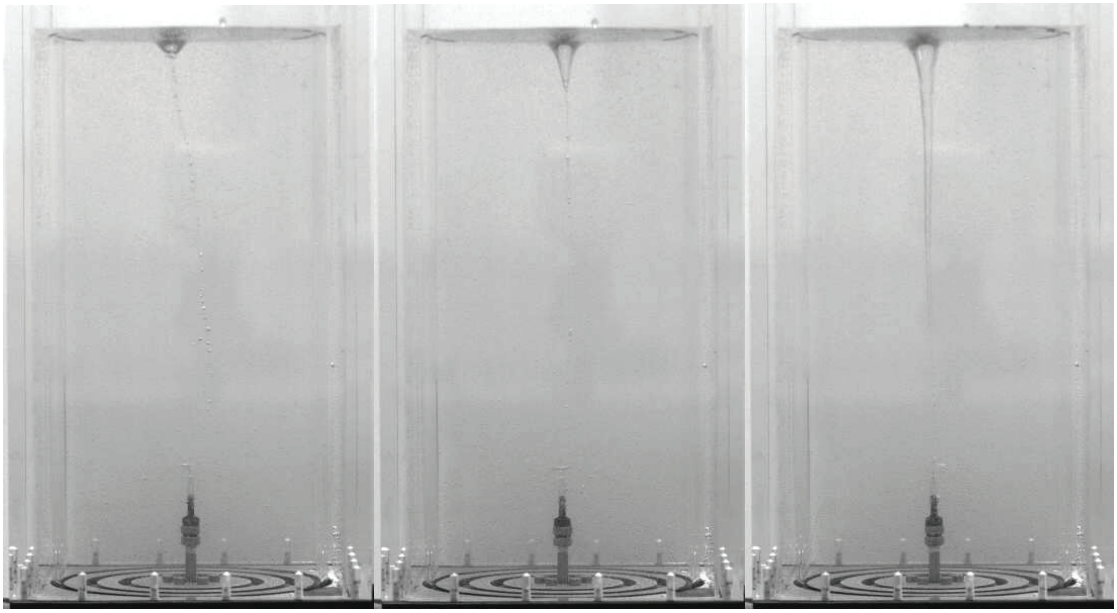

Figure 4.11: Vortex formation.

estimated optically. The method used is based on various sets of images taken at 1500 $fps$, with a resolution of 34 $\mu m/pix$. Bubble volumes $V$ $(m^3)$ were computed from the measured vertical and horizontal diameters, assuming they were axisymmetric:

$$V = \frac{4\pi}{3} \times R_{vertical} \times R_{horizontal}^2$$

where $R_{vertical}$ is the measured vertical radius $(m)$ of the bubble, $R_{horizontal}$ is the measured horizontal radius $(m)$ of the bubble, and it is also the radius of the third dimension assuming the axisymmetry hypothesis.

Knowing the time between each image and the volume of the successive bubbles, the average gas flow rate $Q_{device}$ has been determined using the following formula:

$$Q_{device} = \frac{V}{n_{set} \times \frac{1}{f}}$$

where $f$ is the acquisition frequency $(fps)$, and $n_{set}$ is the number of images in which a same bubble rises through the acquisition window (ranging from 73 to 122). The average gas flow rate has been estimated optically from 7 sets of images at $Q_{device} = 2.8 \pm 0.7$ $L/hour$ (see Graph (4.14)).

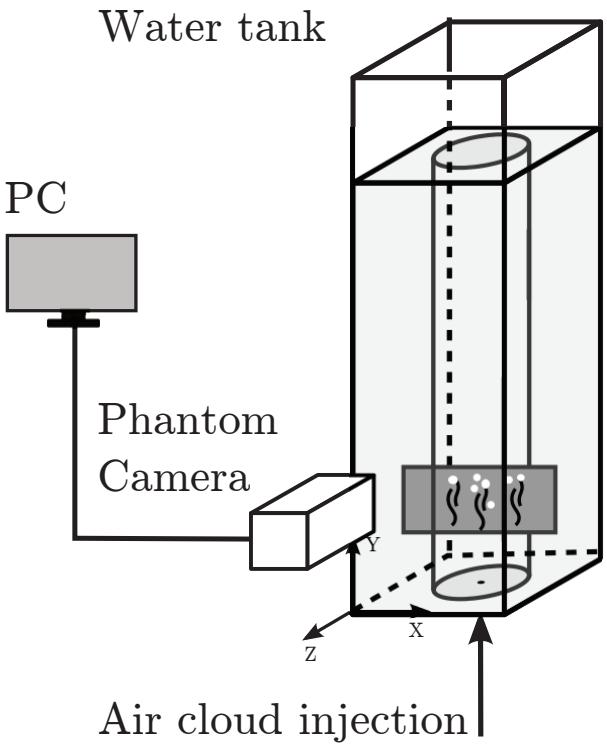


Figure 4.12: Experimental device for bubble diameter study.

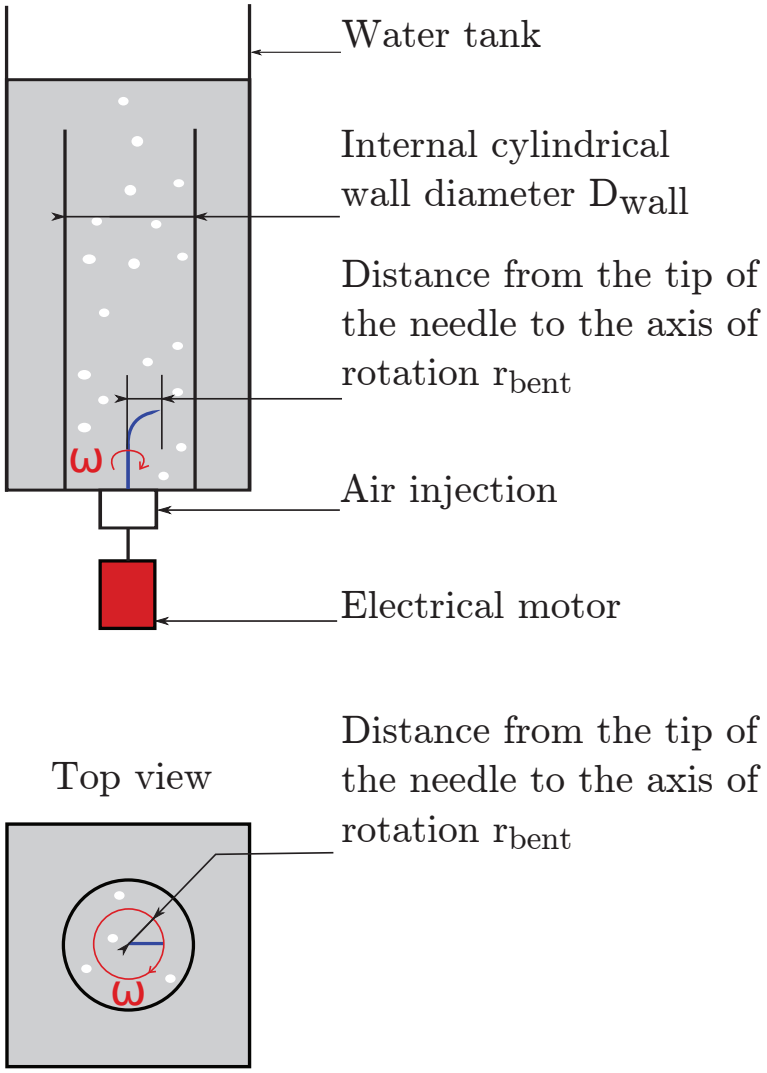


Figure 4.13: Graphical representation of the device. $r_{bent}$ is the distance from the tip of the needle to the axis of rotation.

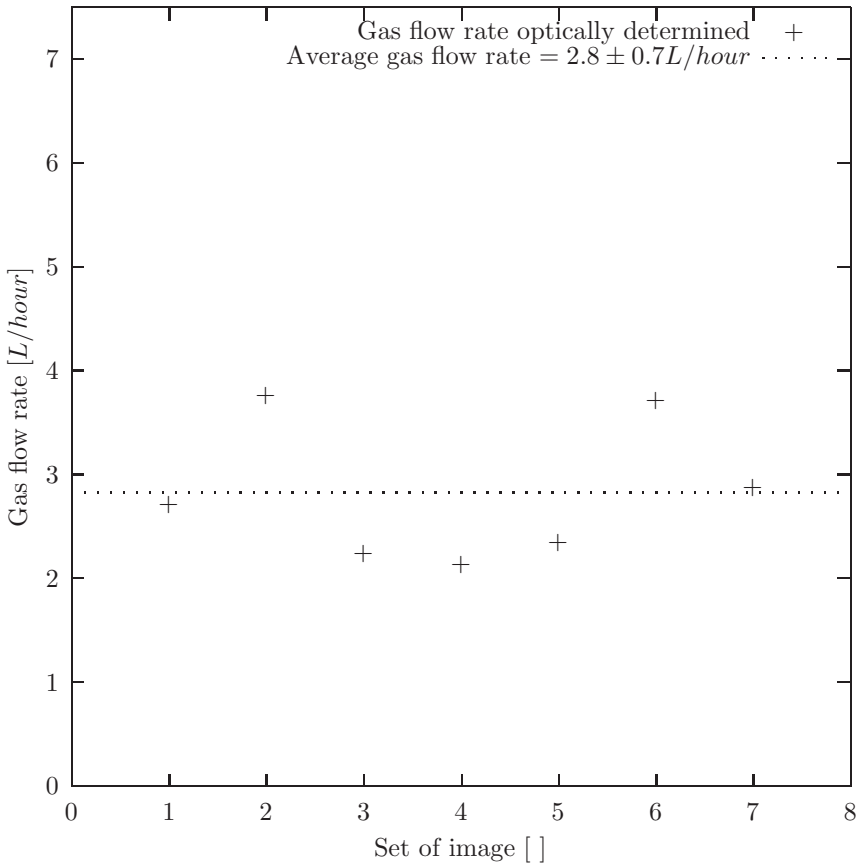


Figure 4.14: Average gas flow rate estimated optically from 7 sets of images.

**Size determination**

Bubble diameters are determined by successive image treatments using GIMP on each selected image. The original image is first sharpened, using the unsharp mask function (80 ; 6.5 ; 0). The next step is the edge detection algorithm using the Sobel operator. The result is then inverted and a threshold (228 over 255 in the example) is fixed for optimal pixel measurements, as described in Figure (4.15). The camera resolution of 34 $\mu m/pix$ led to an error ranging from 2% to $< 14\%$ for smallest bubbles. The mean standard deviation on bubble diameters was found to be 0.432 $mm$.

### 4.5.5 Force equilibrium

As introduced in Section 3.1.1, a bubble is subjected to various forces that can be studied in simplified configurations. The force balance can be studied to determine drag coefficients as in Rastello *et al.* [15]. Tate's law allows for the determination of surface tension $\gamma$ using the surface tension force equilibrium versus gravity.

The case of a bubble generated by the high-speed rotating device, presented in this thesis, is a more complex configuration.

The bubble is fixed to the needle by the surface tension force $T_{tip}$ $(N)$ at the interface between the needle and the bubble $S_{tip}$ $(m^2)$. This contact surface between the bubble and the needle is unknown. It could be optically measured using a camera with very high spatial and temporal resolution.

Weight and buoyancy forces can be determined easily if the bubble diameter is known. Yet, a rough calculation reveals that these two forces are negligible when compared to the other forces (smaller by 3 orders of magnitude). Centrifugal forces $F_{centrigual}$ $(N)$ can be calculated from the rotational velocity and the bubble diameter.

Drag forces $F_{drag}$ $(N)$ are due to fluid resistance:

$$F_{drag} = \frac{1}{2}\rho v^2 S_{ref} C_x$$

where $\rho$ is the density $(kg/m^3)$, $v$ is the relative velocity $(m/s)$, $S_{ref}$ is the reference area $(m^2)$ and $C_x$ is the drag coefficient. Drag coefficient $C_x$ can be found in literature but is usually given for rigid bodies. It is obvious that some encountered configurations implies highly deformed bubbles (see Figure(4.17)), where the rigid body idealization is no longer valid. Drag forces also depend on the speed $v$ of the bubble relative to the water. Needle velocity is known, but the induced flow velocity in the neighbourhood of the bubble is unknown. Therefore, flow velocity field should be determined by PIV in order to obtain drag forces.

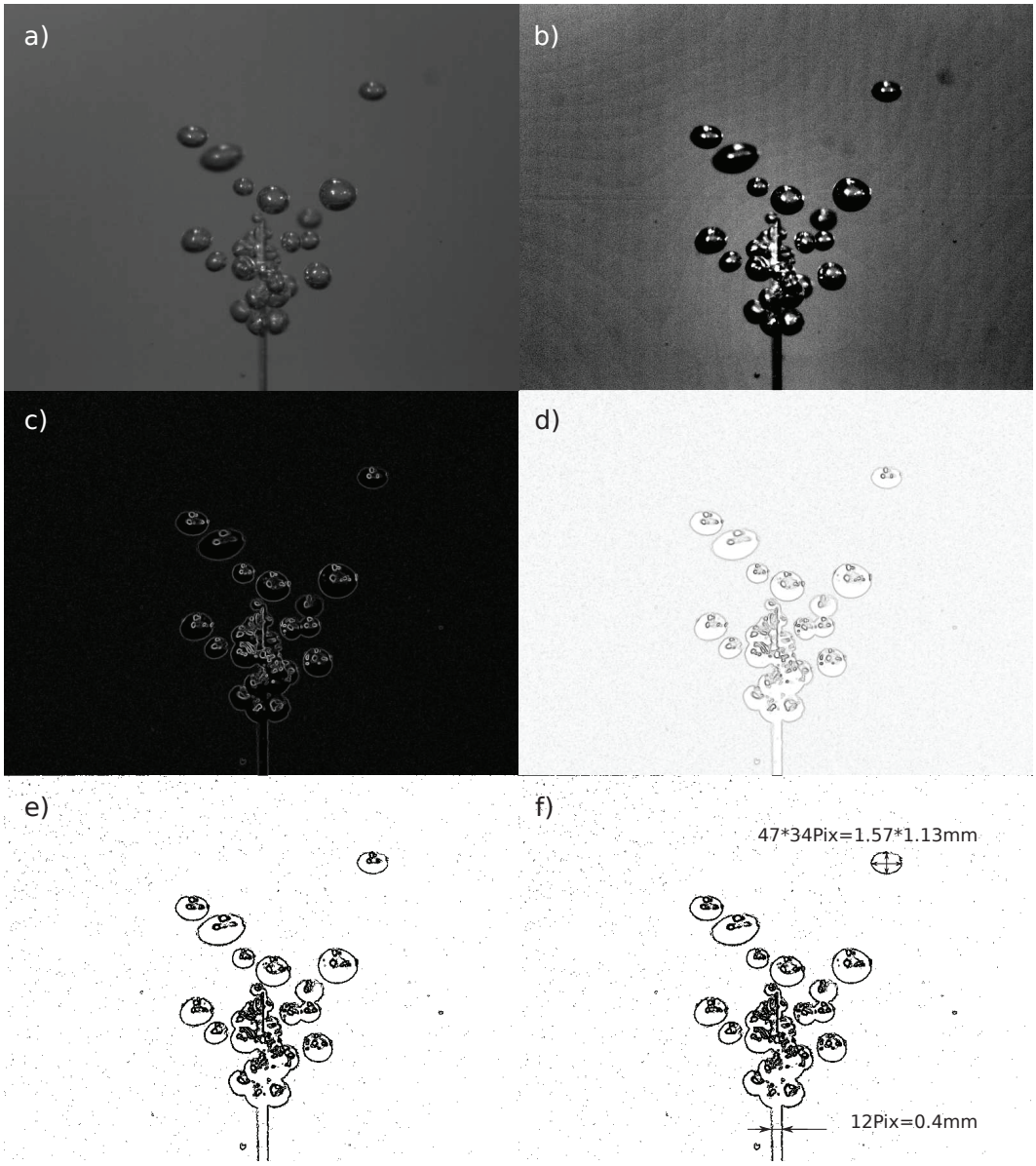


Figure 4.15: Successive image treatments for the bubble diameter determination: a) Original image, b) Sharpening, c) Sobel edge detection, d) Inversion, e) Threshold, f) Measurement.

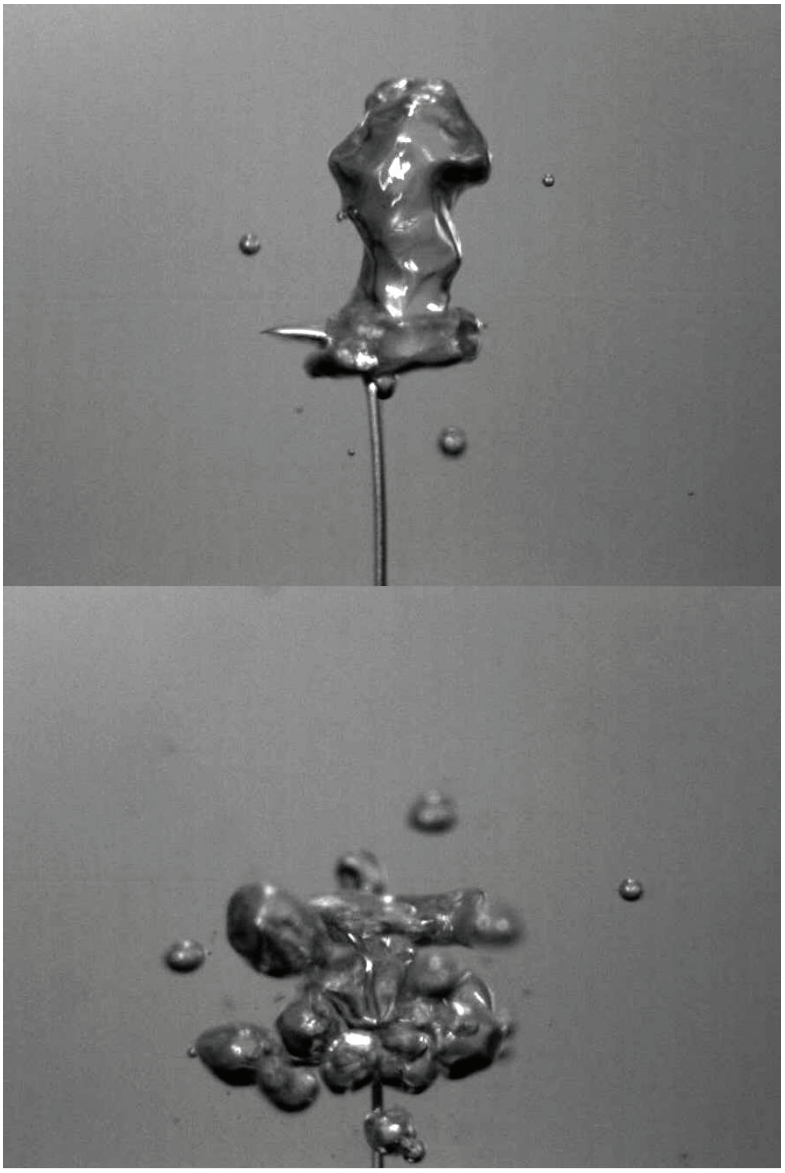

Figure 4.16: Bubble clusters from $r_{bent} = 5\ mm$ needle, rotating at 8640 and 10460 $RPM$, in a 190 $mm$ cylindrical wall.

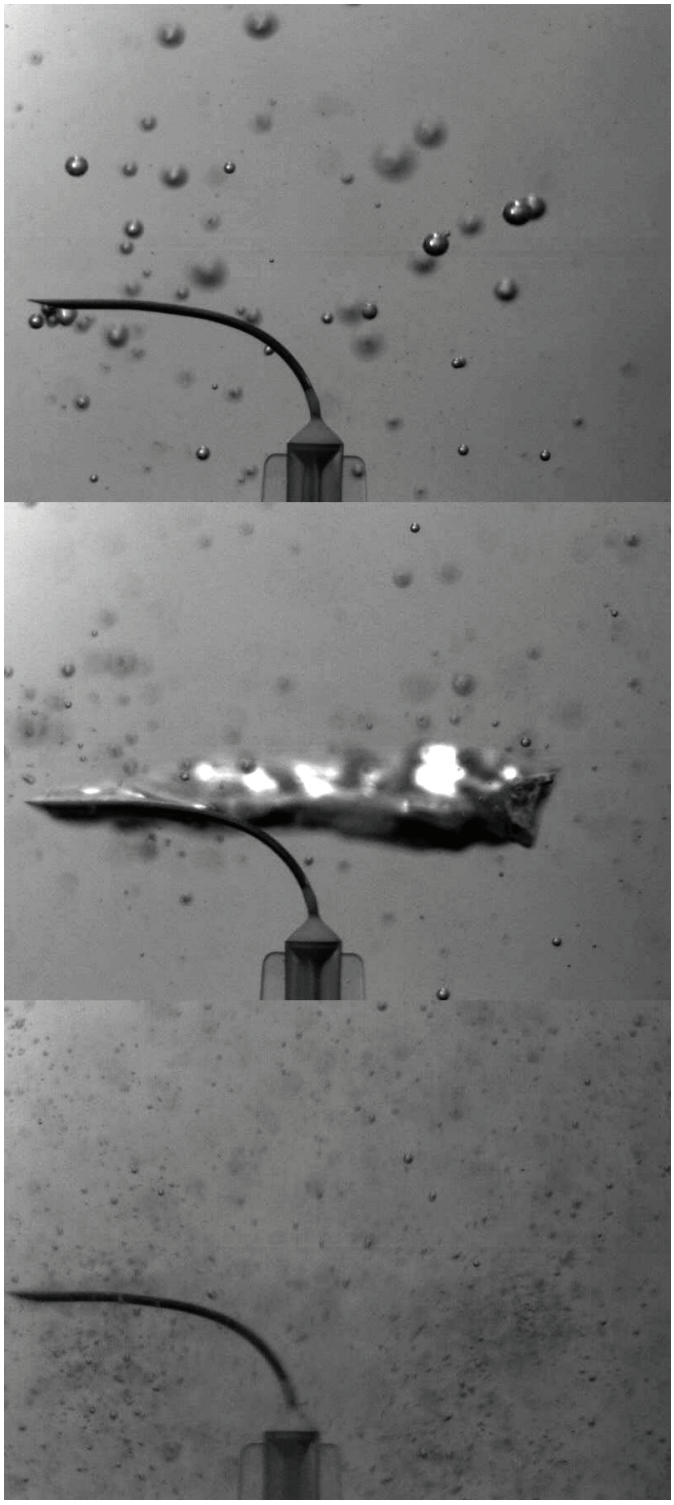

Figure 4.17: Various types of bubbles formed by $r_{bent} = 13\ mm$ needle in the 94 $mm$ cylindrical wall, for increasing rotating velocities (8640, 10460 and 11200 $RPM$).

Drag forces, applied on the projected frontal area of the bubble $S_{ref}$ $(m^2)$ (reference area), create shear forces $F_{shear}$ $(N)$ at the interface between the needle and the bubble $S_{tip}$ $(m^2)$:

$$F_{shear} \approx \frac{S_{ref}}{S_{tip}} \times F_{drag}$$

Top view representation of the forces applied to a bubble generated by the rotating diffuser is pictured in Figure (4.18). A first model could state that the bubble is detached from the needle when the surface tension force at the contact surface between the bubble and the needle is smaller than the centrifugal force plus shearing forces induced by drag forces:

$$T_{tip} < F_{centrigual} + F_{shear}$$

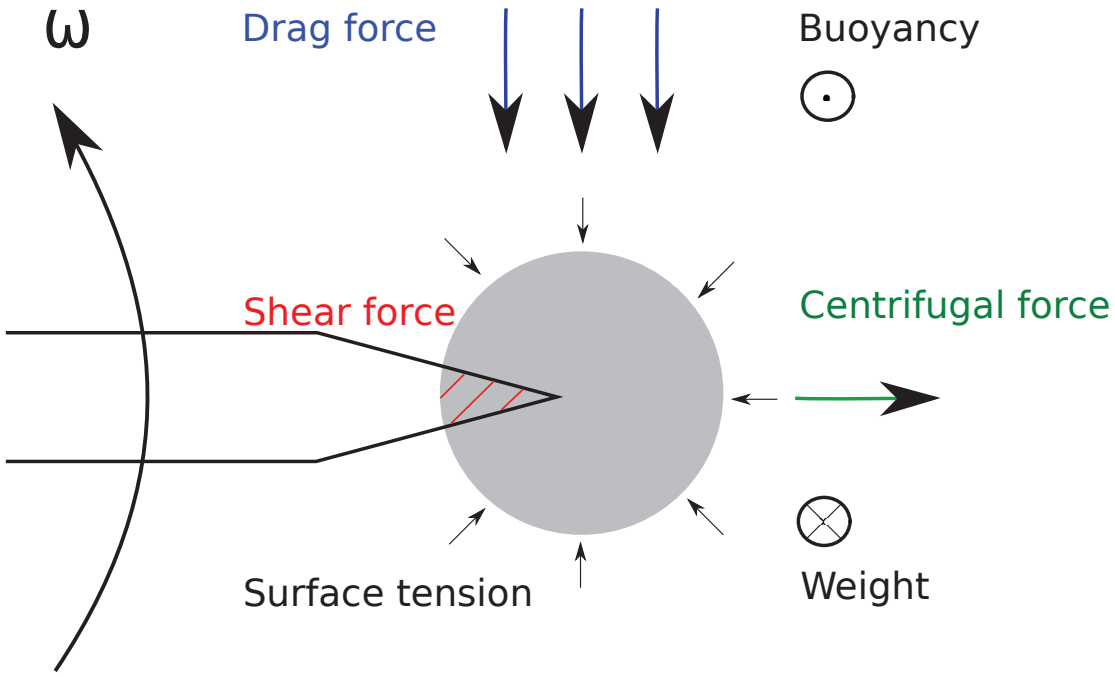


Figure 4.18: Top view representation of the various forces applied to a bubble generated by the rotating diffuser.

Time and equipments have missed for the pursuit of this study. Further investigations should verify forces balance on simplified configurations, and could evaluate the influence other parameters like contamination and viscosity. Along with forces, a system can be characterised by using dimensionless laws, as presented in Section 3.1.2.

### 4.5.6 Dimensionless laws

#### Reynolds and Eötvös numbers

The behaviour of the new MBG has been studied using dimensionless numbers. During the bubble diameter study, 243 bubbles have been measured using the previously presented image treatment. Experimental average bubble diameters have been gathered in Appendix (.2). Depending on the configuration, the standard deviation ranged from 0.166 to 1.042 $mm$. The average standard deviation was 0.432 $mm$. These diameters have been used to calculate the rotational Reynolds $R_\omega$ (see Rastello *et al.* [4]) and Eötvös numbers applied to the rotating device.

In this case, the speed used for rotational Reynolds number is the needle tip velocity $U_{tip}$ $(m/s)$. It corresponds to the product of the rotating velocity $\omega$ $(rad/s)$ with the distance from the tip of the needle to the axis of rotation $r_{bent}$ $(m)$:

$$U_{tip} = r_{bent} \times \omega$$

$$R_\omega = \frac{U_{tip}.D_{bubble}}{\nu}$$

where $U_{tip}$ is the needle tip velocity $(m/s)$, $D_{bubble}$ is the average bubble diameter $(m)$ and $\nu$ is the kinematic viscosity of the liquid $(m^2/\mathrm{s})$.

As defined previously (Section 3.1.2), the Eötvös number is equal to:

$$Eo = \frac{(\rho_l - \rho_g).{D_{bubble}}^2.g}{\gamma}$$

where $\rho_l$ and $\rho_g$ are the liquid and gas densities, $g$ is the gravitational acceleration $(m/s^2)$, and $\gamma$ is the surface tension $(N/m)$.

The curves $Eo = f(R_\omega)$ have been plotted for each bent needle, and each wall diameter in Figure (4.19). For each needle bent ($r_{bent} = 5$ ; 10 and 13 $mm$), a linear relation of the form $Eo = \alpha \times R_\omega - \beta$ has been found. The corresponding fitting coefficients are gathered in Table 4.3. Eötvös numbers $Eo$ appears to increase linearly when rotational Reynolds number $R_\omega$ increases. No outlier measurements was observed. The linear slope decreases when $r_{bent}$ increases, which confirms that the bent of the needle is a significant parameter of the system.

| $r_{bent}$ (mm) | 5 | 10 | 13 |
|---|---|---|---|
| $\alpha$ | $4.1247 \times 10^{-5}$ | $1.70696 \times 10^{-5}$ | $1.36244 \times 10^{-5}$ |
| $\beta$ | $-0.0703216$ | $-0.0470547$ | $-0.0425444$ |

Table 4.3: Fitting coefficient values of $\alpha$ and $\beta$.

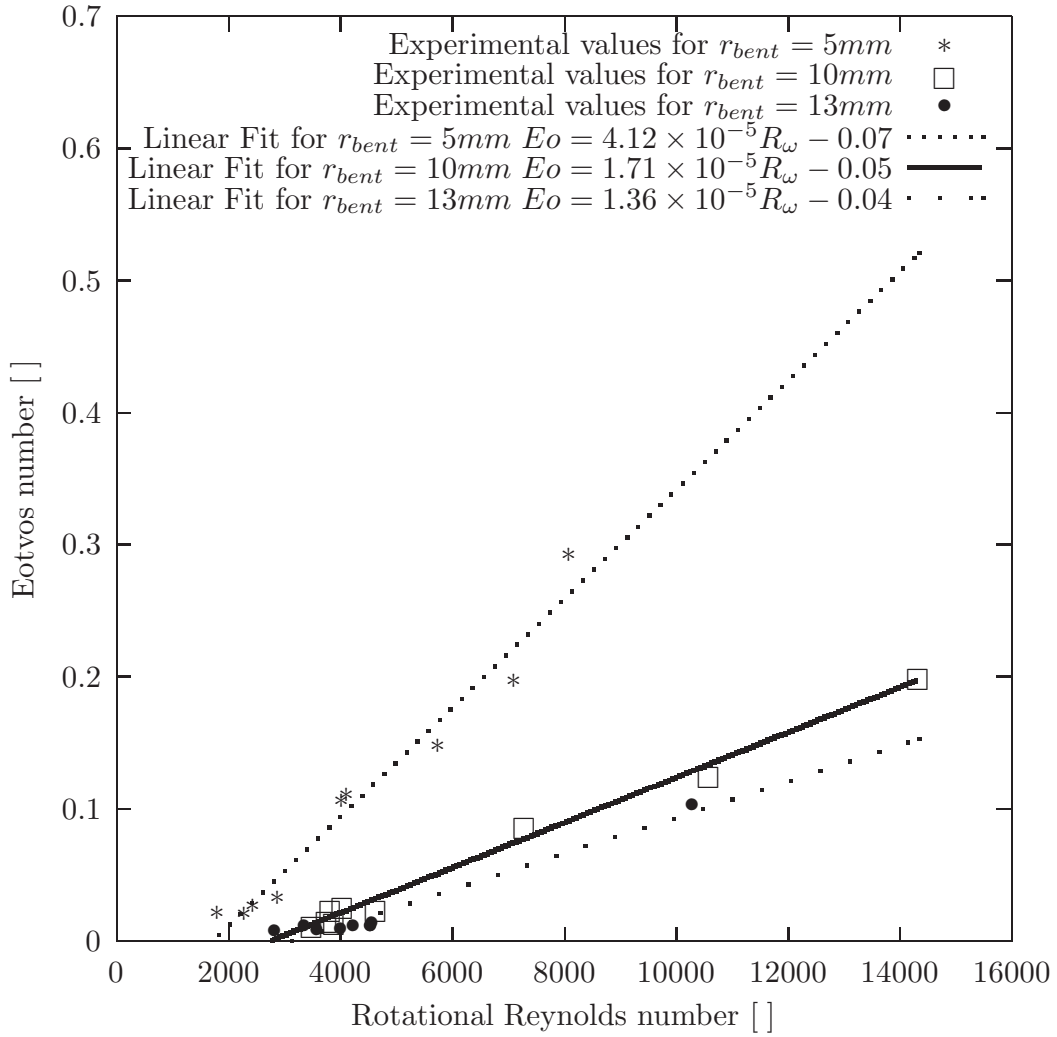


Figure 4.19: Rotational Reynolds and Eötvös number resulting from the mean bubble diameters measured experimentally with the operating rotating device, for the each needle ($r_{bent} = 5$ ; 10 and 13 $mm$). Variables are the rotating velocities $\omega$ and the wall diameters ($D_{wall} = 94$ ; 142 and 190 $mm$). The fitting coefficients are gathered in Table 4.3.

**Eötvös and $\chi$ numbers**

In order to study the influence of the cylindrical wall diameter, a new dimensionless number $\chi$ has been introduced, which is the ratio of the cylindrical wall diameter to the experimental average bubble diameter:

$$\chi = \frac{D_{wall}}{D_{bubble}}$$

$\chi$ ratio versus Eötvös number has been plotted in Figure (4.20), revealing the following power law:

$$\chi = 32.3 \times Eo^{-0.63}$$

One should point out that these points have been obtained by varying 3 different rotating velocities with 3 wall diameters and 3 bent needles. Thus to a given Eötvös number $Eo$ corresponds one value of $\chi = D_{wall}/D_{bubble}$, which indicates a relation between the wall and the bubble diameter. Unfortunately, no data could be found to which we could compare these results. Indeed to our knowledge, similar device do not exist. This is why the present invention has been declared to the intellectual property protection service of the university.

## 4.6 Patent

After experimental testing, the new micro-bubbles system was presented to Lyon Science Transfert (LST). The mission of this organization formed in 2006 is to optimize the transfer of the public research results to the socio-economic world.

If an invention is detected, LST can decide to start maturation (legal, economic and technological). Once the project is protected and well developed, the organization will ensure technological transfer.

The idea of the invention was found in August 2012. Prototype testing has been performed in June and July 2013, and presented to LST in October 2013. INSAVALOR has also been contacted since the tests have been carried out in a laboratory of INSA de Lyon (loi hébergeur). A prior art search for similar patents has been performed in February 2014 by LST. Since related patents are judged non-similar, a Declaration of Invention has been officially signed.

The name of the invention has been registered: "Système rotatif à grande-vitesse de génération de micro bulles ; Application au transfert de masse en milieu diphasique. " Patent drafting has been done in September 2014, and the application N°1459515, entitled "Dispositif de génération de microbulles", has been sent on the $3^{rd}$ of October 2014.

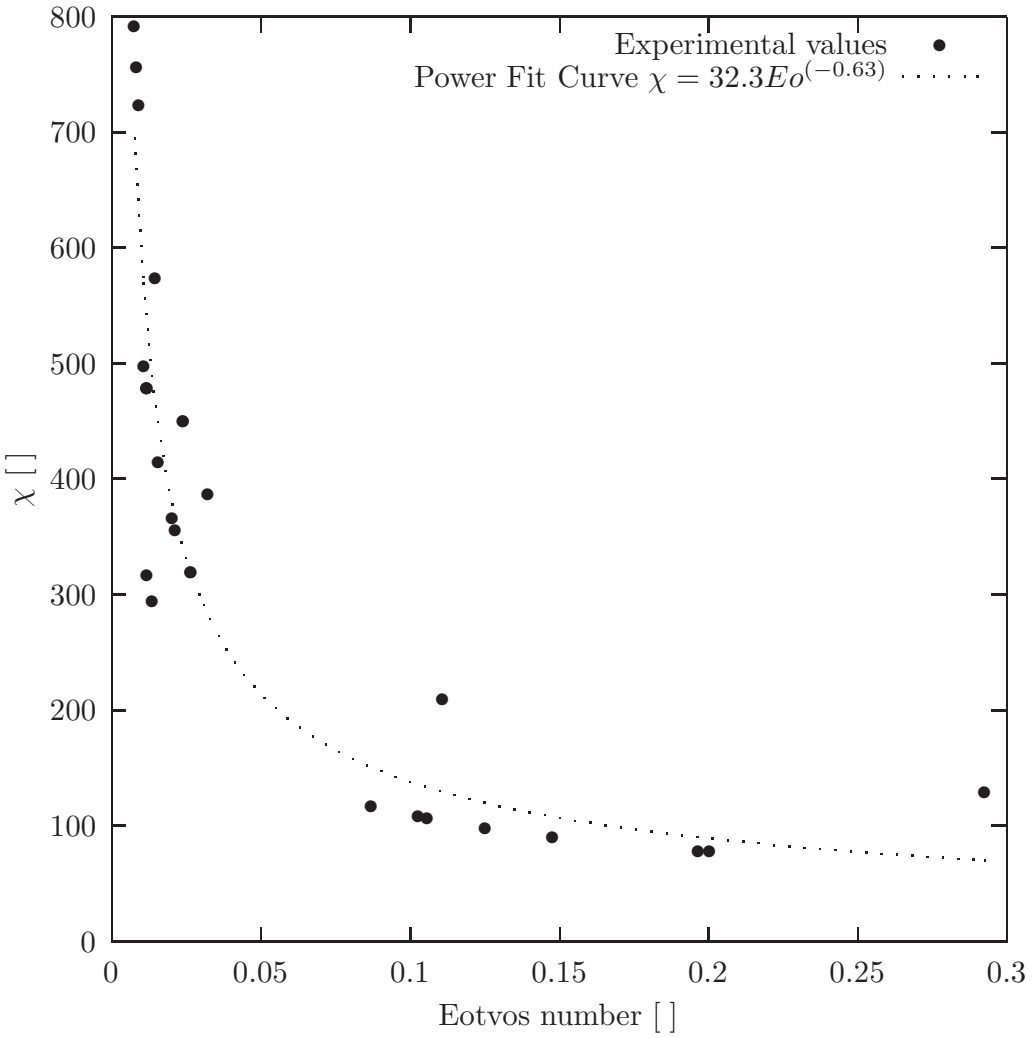


Figure 4.20: $\chi$ ratio versus Eötvös number resulting from the mean bubble diameters measured experimentally with the operating rotating device, for the 3 different needles ($r_{bent} = 5$ ; 10 and 13 $mm$) and the 3 cylindrical walls ($D_{wall} = 94$ ; 142 and 190 $mm$).

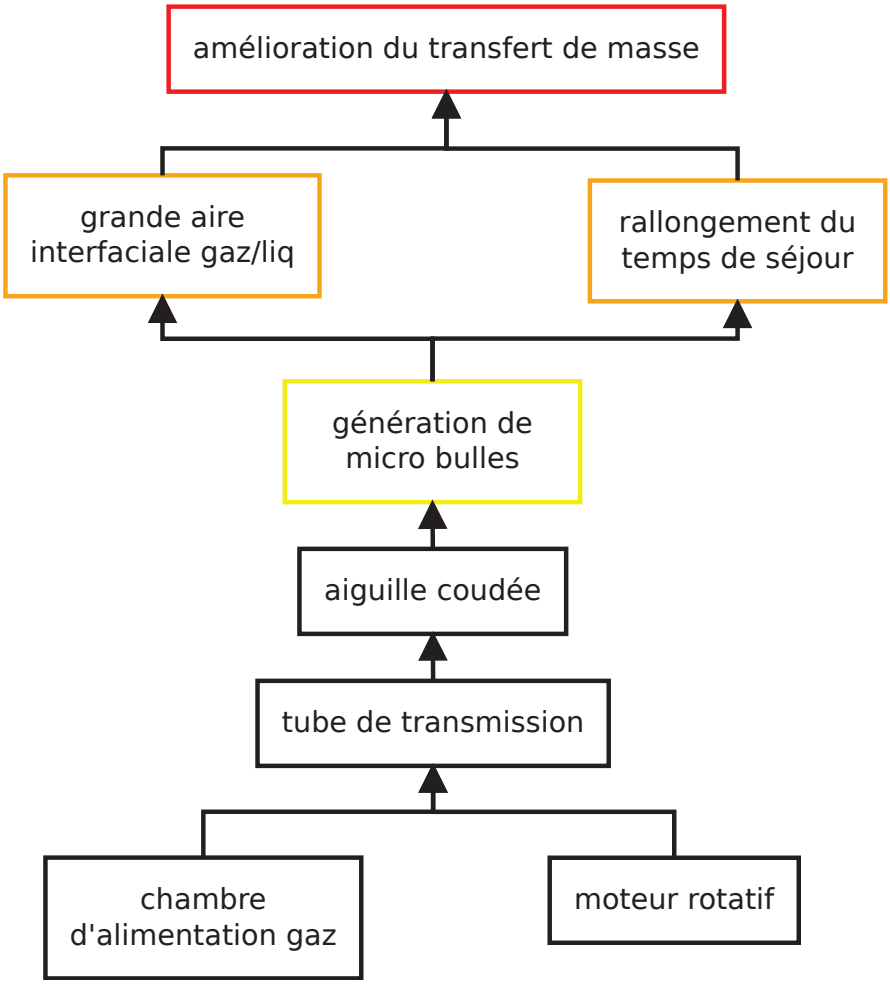


Figure 4.21: New device principles.

## 4.7 Conclusion on the new system

Results of the experimental campaign prove that the device is able to produce bubbles in various range of diameters, using a convenient potentiometer. Under certain conditions, the new prototype system is able to produce micro-bubbles of average diameter $D_{bulle} = 0.252\,mm$, leading to an augmentation of the interfacial gas-liquid area and thus of mass transfer. Dimensionless numbers allowed for the physical characterization of the system. The innovation has been officially declared, and has been used in the experiment described in Chapter (5).

# Bibliography

[1] Basset, J.P., Depeyre, P., Long, J.P.: Construction mécanique, 3GMC - Technologie de construction, documents d'accompagnement. INSA Lyon (2007)

[2] Eriks: Documentation Technique - joints toriques de precision.

[3] FAG: Roulements à billes, à rouleaux et à aiguilles. Publication No.41600 FB (1980)

[4] Rastello, M., Marie, J-L., Grosjean, N., Lance, M.: Drag and lift forces on interface-contaminated bubbles spinning in a rotating flow. Journal of Fluid Mechanics **682** pp 434–459 (2008)

# Part III

# Planar Laser Induced Fluorescence

# Chapter 5

# Concentration measurement taking into account fluorescence extinction variations

*La Fluorescence Induite par Plan Laser (PLIF) permet d'obtenir expérimentalement des coefficients de transfert de masse à partir de la mesure de champs de scalaires. Au cours de ce travail, deux traitements d'image de PLIF prenant en compte les variations de l'extinction de la fluorescence due au pH ont été développés. Le premier traitement a lieu durant la calibration. Il est montré que la méthode proposée doit être appliquée lorsque le produit de la variation du coefficient d'extinction, de la longueur du chemin parcouru par le laser et de la concentration du fluorophore devient grand, comme par exemple pour les expériences dans de grands réservoirs. L'influence des variations du coefficient d'extinction a été évaluée sur une mesure de concentration de $CO_2$ lors d'un cas test dans le sillage d'une bulle en ascension libre dans une colonne d'eau. Le second traitement d'image concerne les cas où le gradient scalaire s'étend sur une large zone. Quand l'étendue de la région de mesure où les variations de pH sont observées augmente, les variations du coefficient d'extinction vont affecter localement l'intensité de la lumière incidente, et donc les mesures. Une correction du traitement d'image prenant en compte les variations de l'atténuation de la lumière incidente a été proposée. La nécessité de cette correction est illustrée par un cas test dans le sillage d'un nuage de bulles en ascension libre dans une colonne d'eau.*

# Abstract

Plan Laser-Induced Fluorescence (PLIF) provides experimental mass transfer coefficients from scalar field measurements. During this work, two data treatments taking into account variations of the fluorescence extinction due to pH have been developed. The first treatment concerns the calibration step. It is shown that the proposed method needs to be implemented when the product of extinction coefficient variations, path length travelled by the laser and fluorescence concentration becomes large as in large tank experiments. The influence of extinction coefficient variations has been evaluated on $CO_2$ concentration measurement for a test case in the wake of a free rising bubble.

The second data treatment has to be applied when the scalar gradient is spread over a large area. When the length in the measurement region over which pH variations are observed increases, variations of the extinction coefficient will affect the local incident light intensity and therefore the measurements. A correction of the data treatment taking into account variations of attenuation of the incident light has been proposed. The need for this correction has been illustrated on a test case in the wake of a cloud of free rising bubbles.


# Nomenclature

### Greek symbols

| | |
|---|---|
| $\delta$ | Diffusive length scale, $[m]$ |
| $\varepsilon$ | Molar extinction coefficient, $[\frac{L}{mol\ m}]$ |
| $\phi$ | Quantum yield of the fluorescence, [ ] |
| $\nu$ | Water kinematic viscosity, $[\frac{m^2}{s}]$ |

### Latin symbols

| | |
|---|---|
| $A$ | Fraction of the available light collected, [ ] |
| $A_{sc}$ | Area of a spherical cap bubble, $[m^2]$ |
| $a$ | Semi-width of a bubble, $[m]$ |
| $C$ | Carbon dioxide molar concentration, $[\frac{mol}{m^3}]$ |
| $c$ | Fluorescein molar concentration, $[\frac{mol}{m^3}]$ |
| $D$ | Carbon dioxide diffusivity in water, $[\frac{m^2}{s}]$ |
| $d_{eq}$ | Equivalent diameter of the bubble, $[m]$ |
| $e$ | Thickness of the laser beam, [mm] |
| $F_{CO_2}$ | Molecular gas flux $F_{CO_2} = K_{L\,CO_2} \times (C_{sat} - C_{CO_2(aq)})$, $[\frac{mol}{s\ m^2}]$ |
| $h$ | Length of the vertical sides of the Region Of Interest (ROI), $[m]$ |
| $I_0$ | Initial light intensity, $[U.A.]$ |

| | |
|---|---|
| $I_e$ | Laser excitation intensity, $[U.A.]$ |
| $I_f$ | Fluoresced intensity, $[U.A.]$ |
| $k_{dehyd}$ | Dehydration rate of $H_2CO_3$, $[\frac{1}{s}]$ |
| $k_{hyd}$ | Hydration rate of $CO_2$ (aq), $[\frac{1}{s}]$ |
| $k_l$ | Mass transfer coefficient, $[\frac{m}{s}]$ |
| $L_d$ | Distance between the diverging lens and the camera field of view, $[m]$ |
| $L_{fluo}$ | Distance traversed by the laser beam in the fluorescent fluid to reach the considered element of the ROI, $[m]$ |
| $L_s$ | Length of the sampling volume along the incident beams, $[m]$ |
| $L_w$ | Width of the camera field of view, $[m]$ |
| $r$ | Coordinate in the downstream direction along a beam of light, $[m]$ |
| $V_b$ | Bubble rising velocity, $[\frac{m}{s}]$ |

**Subscripts**

| | |
|---|---|
| $k$ | Pixel column position along the laser beam, |
| $l$ | Pixel column position along the laser beam, |
| $pH$ | Value of the parameter for a given pH, |
| $ref$ | Value of the parameter for a reference pH before measurements. |

## 5.1 Introduction

This chapter concernes quantitative experimental concentration field measurements of dissolved $CO_2$ in water using Planar Laser Induced Fluorescence (PLIF). $CO_2$ concentration measurements in the wake of free rising bubbles have been carried out. Such measurements could be useful as a validation for numerical simulations of interfacial gas/liquid mass transfer. Those simulations are often applied to free rising bubble test cases. Simulated mass transfer coefficients are then measured and compared to local and mean experimental mass transfer correlations from the literature [6, 7, 10, 30].

In Crimaldi [5], an extensive review of studies using PLIF is presented, reporting various calibration methods and attenuation treatments. Regarding calibration of mass transfer PLIF systems, a first approach found in the literature consists of assuming a linear relationship between re-emitted light intensity and concentration using two known reference points on the image such as in Jirka [14, 15]. Another procedure calibrating quantum yield variations of fluorescence is used by many other authors. Variations of emission intensities are attributed to the concentration of a quencher inhibiting fluorescence as predicted by the Stern-

Volmer relationship. In most studies [1, 6, 21], the linear relationship between the ratio of intensity to reference pH intensity and quencher concentration is obtained from averaged images. However, for large tank experiments, the Stern-Volmer type of calibration should be applied locally because of the important light absorption. Therefore, in the large tank experiment reported by Variano [27], each pixel was calibrated individually from its time averaged intensity. The obtained pixel intensities were then normalised by dividing by their reference pH pixel intensity.

Concerning attenuation of fluorescence with distance, most corrections in the literature are based on the Beer-Lambert law which implies attenuation with an exponential decay along a laser beam [29]. The Optically Thin (OT) criterion is used to characterize systems with a low absorbance of the laser by the fluorophore. In Melton [20], a PLIF experiment has been carried out under OT conditions and variations of fluorescence intensity with distance were approximated by a linear function although deviations were observed. This OT criterion is also evaluated in Roudet [21] and Walker [29] and used as a justification for neglecting attenuation. Attenuation can also be estimated using an exponential fit as in Sarathi [22]. In Jirka [14], the effects of attenuation as a function of length are corrected by fitting an exponential curve through the measured intensities in order to obtain flat-fielded images. An analytical expression is given in Crimaldi [5] for non-collimated laser sheets.

The calibration step can be affected by pH when it is used as a quencher since variations of the extinction coefficient as a function of the pH may be important as reported in several works [19, 29]. Those variations are particularly important while calibrating non-OT systems. However, in the literature and as stated explicitly in [22], attenuation is taken into account separately from calibration, similar to a post-processing step and there is no information concerning the effects of pH on attenuation during the calibration.

This chapter is structured in four parts, starting with the description of a PLIF calibration procedure taking into account extinction coefficient variations. Then a second data treatment will be detailed, taking into account the attenuation in the flow measurement region. An experimental test facility will be described and the first method (Data treatment 1) will be applied to $CO_2$ concentration measurements during its dissolution in the wake of a free rising $CO_2$ bubble. Finally, the need for the second proposed correction (Data treatment 2) will be illustrated on a $CO_2$ concentration measurement in the wake of a dissolving cloud of free rising bubbles.

## 5.2 Correction during calibration step (Data treatment 1)

### 5.2.1 Physicochemical properties

This study is concerned with experimental measurements of $CO_2$ concentration using Planar Laser Induced Fluorescence (PLIF). The $CO_2$ concentration is calibrated against the light intensity emitted by a fluorophore. The fluorescence emission is inhibited when the pH decreases, i.e when $CO_2$ is dissolved in water. The intensity of the laser excitation decreases when it penetrates the fluorescent liquid as it is absorbed by the fluorescent dye. For quantitative PLIF concentration measurements, it is necessary to evaluate the attenuation of the incident light.

For the present experiments, fluorescein sodium ($C_{20}H_{10}Na_2O_5$, CAS : 518-47-8) has been selected as the fluorescent dye due to the strong pH dependence of its absorption and emission properties in aqueous solution. Its complex acid-base chemistry in both ground state and excited state results in four protolytic forms with their own emission spectra [18, 19, 24]. Fluorescein sodium was purchased from MERCK that indicates a maximum absorption at 490-492 $nm$ in a pH 8.0 buffer solution. Calibrations carried out in this work are consistent with the assumption that the sole mechanism responsible for the decrease of the fluorescence with increasing $[H^+]$ is the Stern-Volmer quenching of the excited states by $H^+$. From Guilbault [12], Stern-Volmer quenching is : "commonly called collisional quenching, although collisions are not the only possible mechanism ". The protonation mechanism described here is one of them. As shown in Section 5.2.3, the molar extinction coefficient $\varepsilon$ will be determined locally as a result of the present study. It was found to be around $1.28 \times 10^5$ $L\ cm^{-1}mol^{-1}$.

Particular care was taken to avoid photobleaching as the laser was turned on only during calibration and data acquisition. Photobleaching's effects were checked by performing bench tests under experimental illumination conditions for different fluorescein concentrations homogenised with a magnetic stir bar. Tests show that there is no decrease of the fluorescence signal over the experimental time period. Therefore, it has been concluded that no photobleaching occurred in the experimental data. In the emission spectra, a part of the fluorescence intensity can be reabsorbed. Under the operated experimental conditions and for the length travelled by the re-emitted light between the center pixel of the Region Of Interest (ROI) and the camera, such absorption of fluoresced intensities is negligible as the exponential term in the Beer-Lambert law of absorption (described in the next Section) is close to one (0.982) when calculated as in Simoëns and Ayrault [23]. However, for emission intensity, under the same experimental con-

ditions and for the length travelled from the laser source to the center pixel of the ROI, this exponential term is equal to 0.814 and the attenuation is not considered as negligible. A correction for this attenuation is now proposed.

### 5.2.2 Beer-Lambert law for non-optically thin systems

From Walker [29], considering that no saturation intensity occurred for all present measurements, and considering that intensity attenuation can be neglected along the optical path from the sampling volume to the CMOS camera, the fluorescence intensity recorded can be described by the Beer-Lambert equation (5.1).

$$I_f = I_0\ A\ \phi\ \varepsilon\ L_s\ c\ exp(-\int_{L_{fluo}} \varepsilon\ c\ dr) \tag{5.1}$$

$I_0$ stands for the initial light intensity, $A$ is the fraction of the available light intensity collected, $\phi$ is the quantum yield of the fluorescence, $\varepsilon$ is the molar extinction coefficient, $L_s$ is the length of the sampling volume along the incident beams, $c$ the fluorescein sodium concentration, $L_{fluo}$ is the distance travelled by the laser beam in the fluorescent fluid and $r$ is the coordinate along a beam of light (Figure (5.1)).

Dividing each pixel intensity by a reference intensity $I_{f,ref}$ corresponding to a reference pH and considering that $c$, $A$, $L_s$ and $I_0$ are constants, the following equation (5.2) is obtained:

$$\begin{aligned} \frac{I_f}{I_{f,ref}} &= \frac{\phi\ \varepsilon\ exp(-\int_{L_{fluo}} \varepsilon\ c\ dr)}{\phi_{ref}\ \varepsilon_{ref}\ exp(-\int_{L_{fluo}} \varepsilon_{ref}\ c\ dr)} \\ &= \frac{\phi\ \varepsilon}{\phi_{ref}\ \varepsilon_{ref}} exp\left(c\int_{L_{pH\neq pH_{ref}}} (\varepsilon_{ref}-\varepsilon)dr\right) \end{aligned} \tag{5.2}$$

For each pixel of the recorded image, considering that the length over which the reaction is observed ($L_{pH\neq pH_{ref}}$) is small, the integral is negligible and the following relationship (equation 5.3) is obtained for the intensity variations as a function of pH :

$$\frac{I_{f,pix}}{I_{f,ref,pix}} \approx \frac{\phi\ \varepsilon}{\phi_{ref}\ \varepsilon_{ref}} \tag{5.3}$$

Therefore $(\phi\varepsilon)/(\phi_{ref}\varepsilon_{ref})$ needs to be calibrated as a function of pH. For a fixed concentration of fluorescein sodium, background images are acquired for different pH values and divided by the same reference as used previously, giving :

$$\frac{I_{f,pH,pix}}{I_{f,ref,pix}} = \frac{\phi_{pH}\varepsilon_{pH}}{\phi_{ref}\varepsilon_{ref}} exp\left(c\int_{L_{fluo}}(\varepsilon_{ref}-\varepsilon)dr\right) \tag{5.4}$$

Equation (5.4) shows that a variation of $(\varepsilon_{ref}-\varepsilon)$ induces an exponential variation of $\frac{I_{f,pH,pix}}{I_{f,ref,pix}}$. If $L_{fluo}c(\varepsilon_{ref}-\varepsilon)$ is not negligible, molar extinction coefficient variations have to be taken into account for each pixel during the calibration of $(\phi\varepsilon)/(\phi_{ref}\varepsilon_{ref})$ as a function of pH. Since $L_{fluo}c(\varepsilon_{ref}-\varepsilon)$ can not be measured directly, a method for molar extinction coefficient determination from background images at known and fixed concentration is thus presented in the following section.

### 5.2.3 Extinction coefficient variation calibration

Extinction coefficient evolution as a function of pH has been determined from homogeneous background images acquired for uniform concentrations of $CO_2$ in the fluid, obtained after mixing during a sufficient time. Within the Region Of Interest (ROI) which has been approximated to a laser beam, ratios of intensities at different positions along the laser beam can be expressed using equation (5.1). If the intensity at one position along the laser beam was taken as the intensity of a pixel column of the ROI, the ratio of intensities received by two pixel columns can be written as follows:

$$\frac{I_{f,k}}{I_{f,l}} = exp(-\varepsilon c L_{k,l}) \tag{5.5}$$

with k and l being the index position of pixel columns.

The part of intensity decreasing due to the diverging lens geometry shown in Figure (5.1) can be corrected by adding a supplementary attenuation term as done in equation (5.7).

Assuming no fluorescent dye and a constant thickness of the laser sheet, and considering light flux conservation, the ratio of intensities (per unit area) received by two pixel columns k and l can be determined geometrically :

$$\frac{I_k}{I_l} = \frac{h_k}{h_l} = \frac{L_d + L_w}{L_d} \tag{5.6}$$

where $I_k$ and $I_l$ are the light intensities received by the pixels of two pixel columns k and l, belonging to the ROI, of respective height $h_k$ and $h_l$. $L_w$ is the width of the camera observation area, and $L_d$ is the distance between this area and the diverging lens, as shown in Figure (5.1).

From equations (5.5) and (5.6) we obtain :

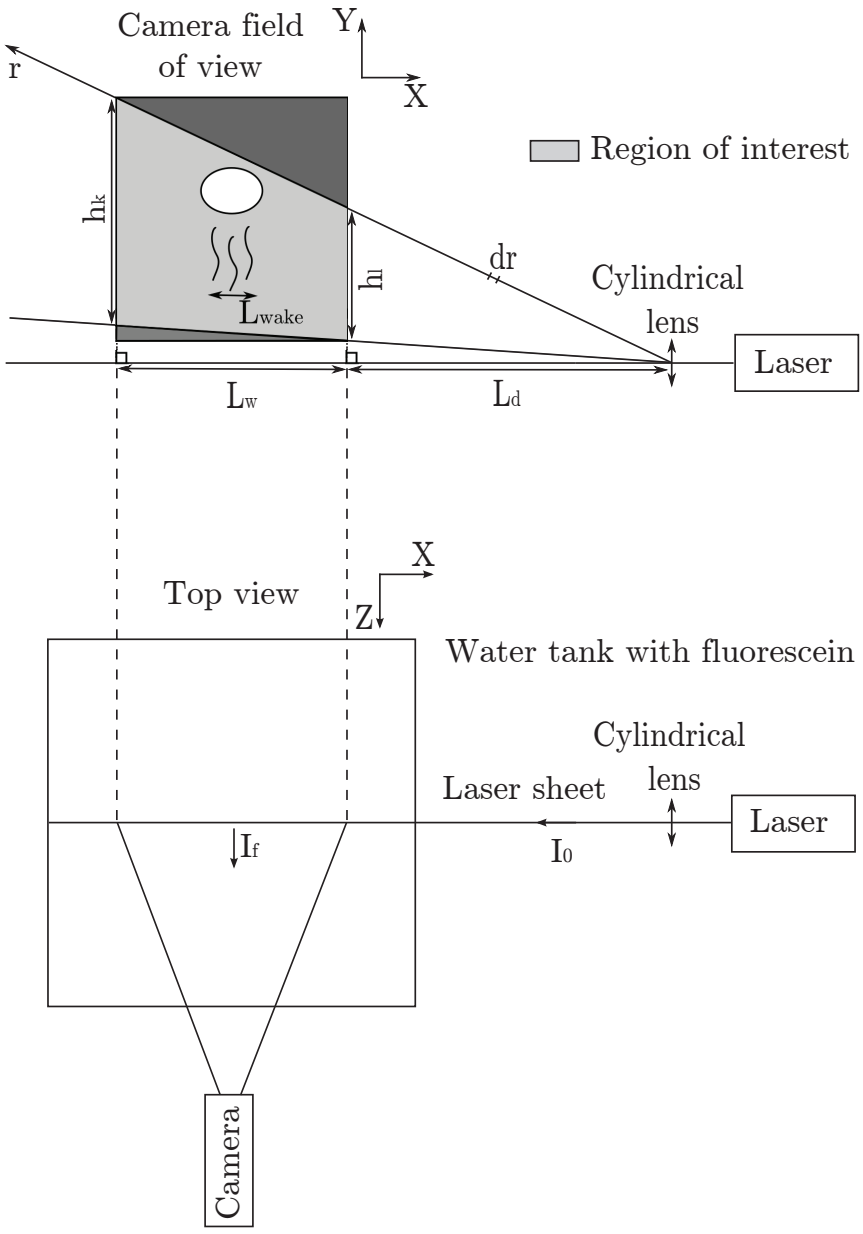


Figure 5.1: Schematic view of the camera observation area and of the Region Of Interest in which the $CO_2$ concentrations have been measured. On this representation, positions k and l are on the borders of the field of view, therefore the distance $L_{k,l}$ between two columns is maximal.

$$\varepsilon = -\frac{ln\frac{I_{f,k}}{I_{f,l}}}{cL_{k,l}} - \frac{ln(1+\frac{L_w}{L_d})}{cL_{k,l}} \tag{5.7}$$

This geometrical contribution has been taken into account in equation (5.7). As it is a constant for any pair of pixel columns, it has no influence on the extinction coefficient variations ($\varepsilon_{ref} - \varepsilon$) as a function of pH.

The influence of the distance $L_{k,l}$ between two columns on the measurements scatter during the determination of the non-corrected $\varepsilon$ is shown in Figure (5.2). For a given pH during calibration, as the amplitude of the extinction increases with the length travelled by the laser beam, the scattering of the measured extinction coefficient diminishes with the distance between two pixel columns used for its determination.

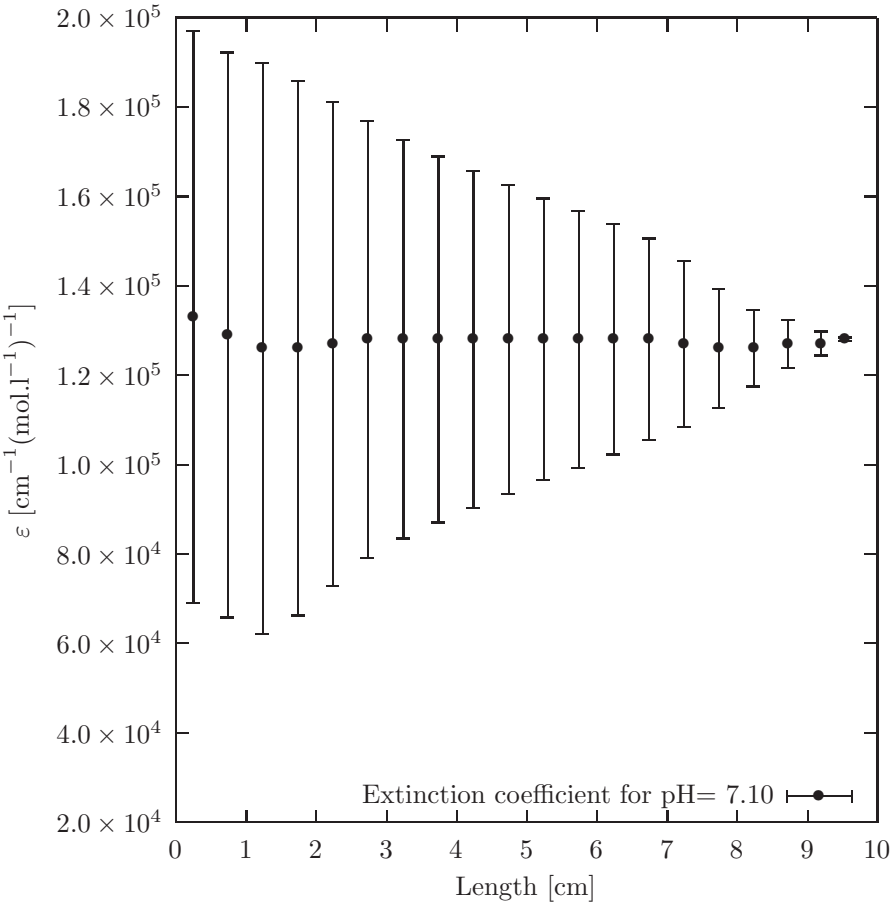


Figure 5.2: Standard deviation of the non-corrected extinction coefficient $\varepsilon$ measurements, for a given pH during calibration.

The global data acquisition and data treatment procedures from the acquired fluorescence signal to $CO_2$ concentration maps are presented in Figures (5.3) and (5.4). The presented extinction coefficient variation calibration corresponds to step 2.a). In step 2.b), the corrected Sterm-Volmer calibration is then established for each pixel, and intensities are converted to pH values by interpolation (step 2.c)). The final step 2.d) is the conversion from pH maps to $CO_2$ maps.

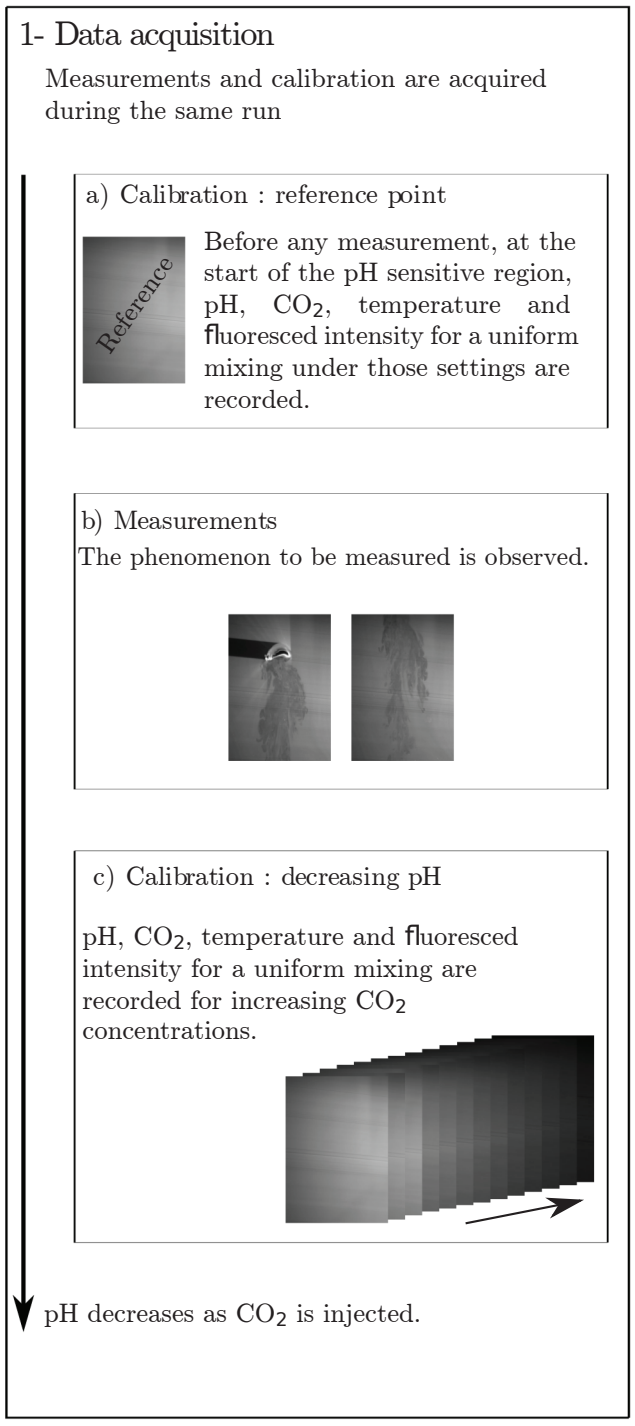


Figure 5.3: Data acquisition procedures.

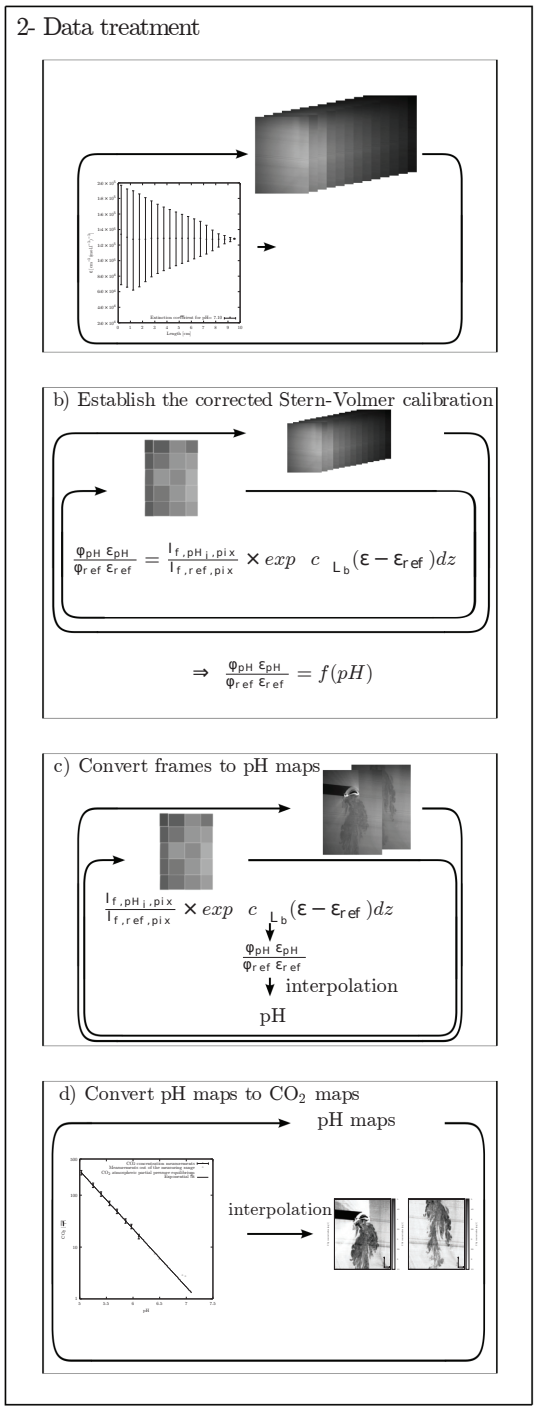


Figure 5.4: Data treatment procedures.

## 5.3 Correction in the measurement region (Data treatment 2)

### 5.3.1 Concerned situations

When the OT criterion is not applicable and more precisely when $L_{fluo}\, c\, (\varepsilon_{ref} - \varepsilon)$ is not negligible, it has been shown that it was necessary to take into account attenuation during the calibration step. The procedure proposed in the previous section suggests establishing an attenuation-corrected calibration for each pixel. Using this calibration, the need for a post-treatment correction of attenuation and its corresponding induced errors is removed.

However the proposed procedure is limited to situations where $(\int_{L_{pH \neq pH_{ref}}} c\, (\varepsilon_{ref} - \varepsilon) dr)$ is negligible (see equation 5.2). When the length travelled by the incident laser in the measurement region increases (see Figure (5.5)), variations of the incident light attenuation induced by pH variations will also become significant and therefore the approximation used will no longer be valid. A supplementary correction for such situations is necessary.

The PLIF data treatment proposed now considers PLIF data obtained following the experimental procedure described previously, for which extinction coefficient variations as a function of pH are measured and taken into account during the calibration. For theses corrections to be applied, it is similarly considered that no saturation intensity occurred and that intensity attenuation can be neglected between the sampling volume and the camera [29]. Therefore the fluorescence intensity recorded can be described by the Beer-Lambert equation (5.1), leading to equation (5.2).

For each pixel of the recorded image, if the length over which the reaction is observed ($L_{pH \neq pH_{ref}}$) is not negligible, then it is necessary to evaluate the contribution of the exponential term $exp(c \int_{L_{pH \neq pH_{ref}}} (\varepsilon_{ref} - \varepsilon) dr)$ in order to obtain the local ratio of $(\phi\, \varepsilon)/(\phi_{ref}\, \varepsilon_{ref})$.

### 5.3.2 Additional correction

It is possible to evaluate the contribution of this exponential term when the laser sheet is collimated. If pH variations do not affect the incident light before entering the measurement region, then pH can be determined for the first pixel array reached by the incident light. The extinction coefficient, which has been calibrated as a function of pH following the experimental procedure described in Section 5.2, can be evaluated for the first pixel array.

It is then possible to evaluate the exponential term for the first pixel array and to take it into account in order to find the $(\phi\, \varepsilon)/(\phi_{ref}\, \varepsilon_{ref})$ ratio. From this ratio,

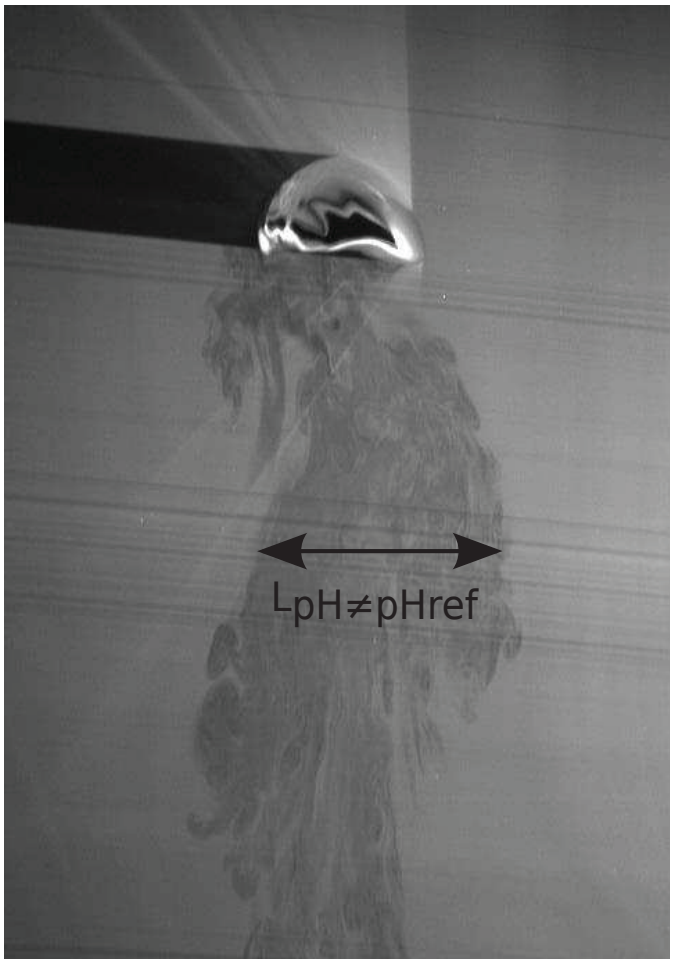


Figure 5.5: Area where pH variations are observed. If this area becomes significant, the second correction is necessary.

the corresponding pH value is obtained for the second pixel array and the process can be repeated for the next pixel array. The implementation of an experimental setup that will be used to illustrate the interest of this second proposed correction is described in the Section 5.5.

## 5.4 Application of Data treatment 1

A correction taking into account fluorescence extinction variations during the calibration step has been presented in Section 5.2. The need for this correction has been evaluated on a test case in the wake of a free rising $CO_2$ bubble. In this case,

pH variations remained local and the exponential term $exp(c\int_{L_{pH\neq pH_{ref}}}(\varepsilon_{ref}-\varepsilon)dr)$ has been neglected. The related experimental setup will first be described. The $CO_2$ concentration field obtained using the proposed correction will then be compared to non-corrected results.

### 5.4.1 Experimental setup

**Bench characteristics**

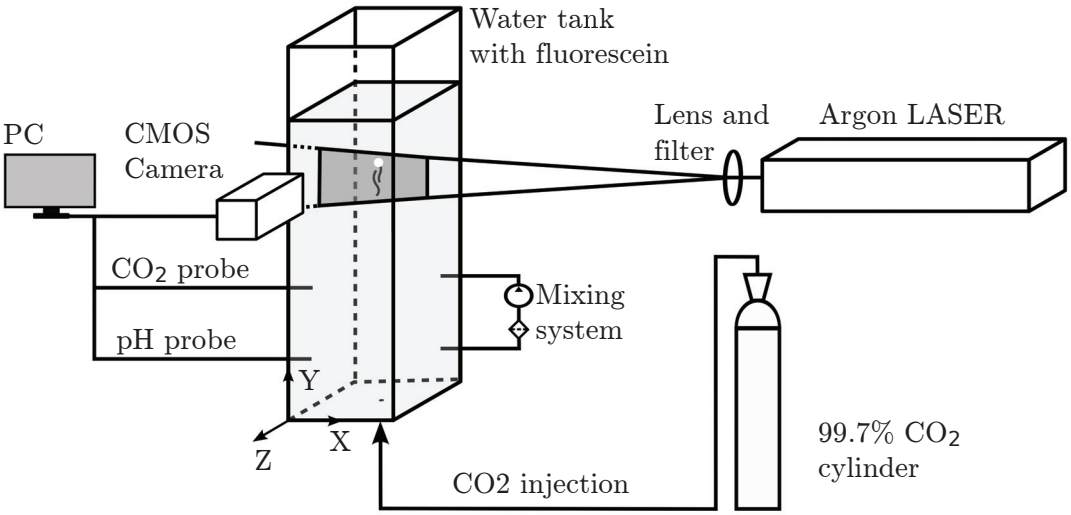


Figure 5.6: Schematic view of the Planar Laser Induced Fluorescence experimental set-up used for $CO_2$ concentration measurements in the wake of a free rising $CO_2$ bubble dissolving into an aqueous solution of fluorescein sodium illuminated by an argon laser plane.

The 99.7% pure $CO_2$ gas bubble rises in the middle of a transparent tank having a $0.27 \times 0.27\ m^2$ square section. The tank is filled with 45 litres of demineralized water (total hardness $< 17.8\ ppm = 1.56\ \mu S/cm$) containing $5 \times 10^{-7} \pm 0.1\%\ mol/L$ of dissolved fluorescein sodium. This concentration has been chosen in order to maximize the image dynamic range, without reaching saturation.

The PLIF experimental setup described in Figure (5.6) uses a $4\ W$ Argon-Ion laser mounted with a $488\ nm$ bandpass filter, a wavelength in the fluorescein sodium's excitation spectra. The output power after filtering is $0.3\ W$. A cylindrical lens is used to obtain a sheet of light from a beam of width $e = 1.4\ mm$ at

$\frac{1}{e^2}$ intensity points (manufacturer specification). A posteriori measurement of the width of the mark left by the laser sheet on a photosensible paper allows for the confirmation of this value.

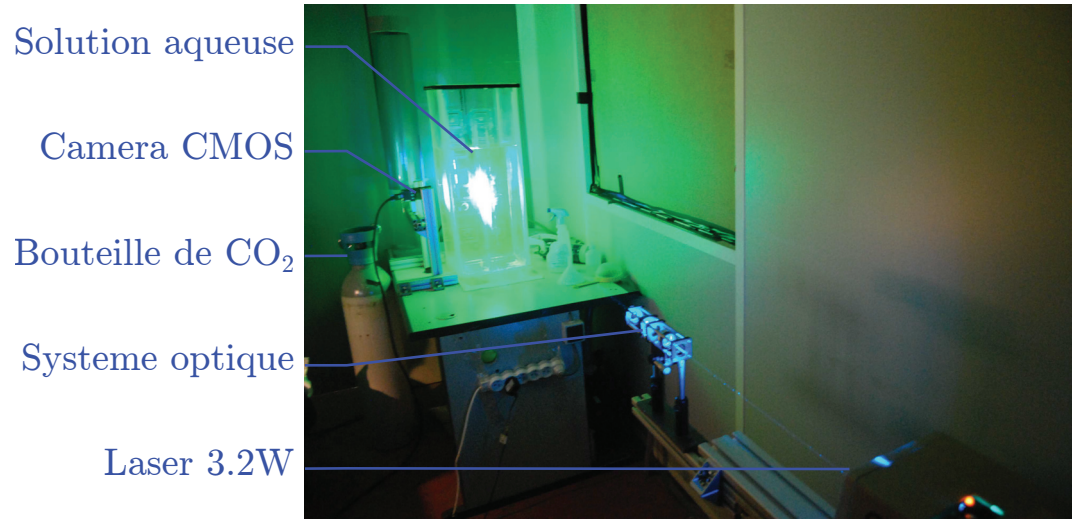


Figure 5.7: Picture of the PLIF experimental setup.

A CMOS camera (described later) connected to a computer allows for the recording of fluorescence intensities and associated variations due to pH gradients in the plane crossed by the laser sheet. Those gradients are induced by the reaction of water with the dissolved $CO_2$ in the bubble wake.

The reference pH was recorded for each bubble rising just before the bubble was released. It was obtained with a METLER-TOLEDO pH-meter which has a resolution of 0.01pH. The pH reference is reached when the water solution is in equilibrium with the atmosphere. Atmospheric composition variations lead to pH references with an average value of 7.02 and a standard deviation of 0.12. In this pH range the fluorescein sodium is highly sensitive to pH changes, as used in Stöhr [25] for qualitative mass transfer investigation behind a free rising bubble, without quantitative concentration measurements of dissolved $CO_2$.

### Acquisition system

Images of rising bubbles along the laser sheet are recorded using a Dalsa Falcon 1.4M100 HG CMOS 8-bit camera mounted with a 16 $mm$ high resolution and low distorsion lens. A vertical binning leads to a resolution of $480 \times 688$ with a scale of 0.1 $mm$ per pixel vertically and 0.2 $mm$ per pixel horizontally. The camera acquisition was set at a frequency of 100 frames per second and with an exposure

time of 1 $ms$. About 25 frames were recorded for a single rising bubble. Images were acquired under a very low external parasite light since the gray level of the camera was null when there was no fluorescein sodium in the water tank. The received light intensity was too low for the available filter to be placed between the camera and the laser sheet.

It should be noted that fluorescence is an inelastic and isotropic radiation process with emission independent of the direction and therefore independent of the position of the CMOS camera [16, 29]. Considering that fluorescein sodium is relatively temperature insensitive [9], the variation of two degrees observed during the experiment has been neglected (associated error is $< 0.8\%$).

### Bubble velocity

Influence of surfactants on the motion and mass transfer from bubbles moving in a liquid were discussed in Clift, Grace and Weber [4]. The main effect is to reduce the mobility of all or part of the interface resulting in a different rising velocity than the clean water case. This can be used to specify the water quality as in Stöhr [25].

For the actual study, velocities have been measured 300 $mm$ above the bubble injection nozzle where stationary rising velocity has been reached [8]. Results have been compared to data reported in Clift, Grace and Weber [4] as shown in Figure (5.8) and found to be close to those obtained for pure water conditions. In order to obtain results comparable to [4], the gas used for this water investigation was atmospheric air.

From [17], considering that the ratio of the bubble diameter to the distance between the bubble and the closest wall is smaller than 0.125, tank wall effects on rising velocity can be neglected.

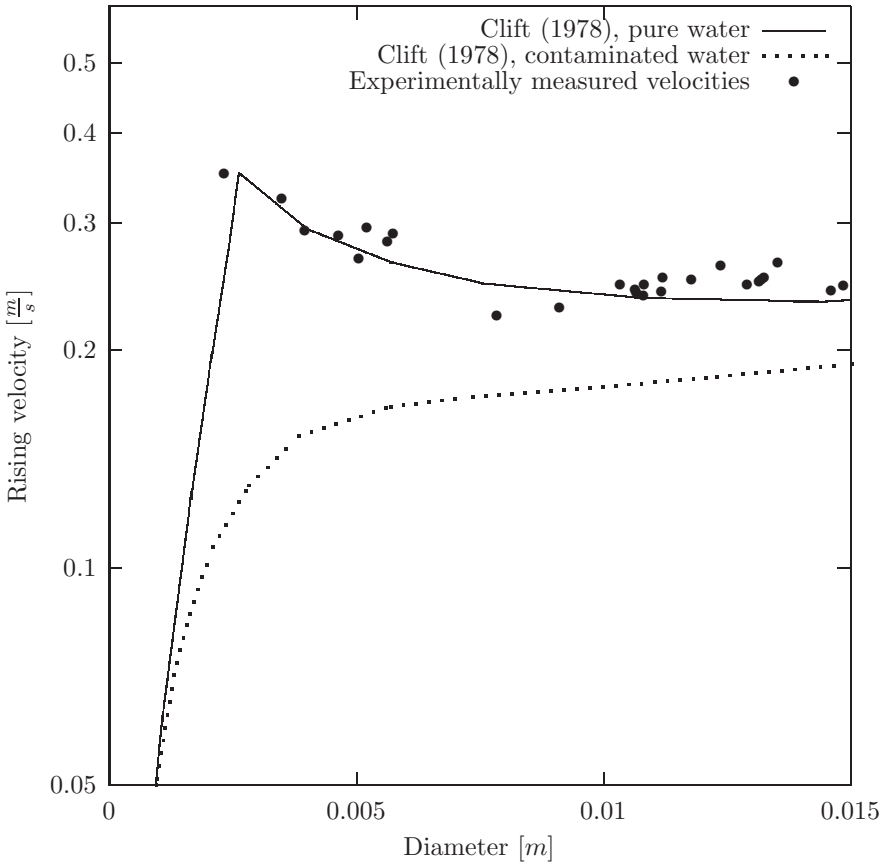


Figure 5.8: Specification of the influence of surfactants in the medium comparing experimentally measured rising air bubble velocities with data from the literature (Clift, [4]) for contaminated and pure water.

### 5.4.2 Application of PLIF to a free rising bubble wake

Using the previously described experimental setup, $CO_2$ concentration fields have been obtained using the correction proposed in Section 5.2, called here Data Treatment 1 and with a calibration taking into account fluorescence extinction variations. $CO_2$ concentration evolution as a function of pH in the medium is presented in Figure (5.11). These concentrations have been measured with a Metler Toledo $CO_2$ InPro 5000 probe. Above the probe operating limit of 14.7 $mg/L$, the error is about 10%, as indicated by the manufacturer's specification.

These measurements show that the $CO_2$ concentration is exponentially increasing as pH is decreasing and it can be noticed that this curve tends to the theoretical $CO_2$ concentration in equilibrium with the atmosphere (filled triangle). Following this observation, an exponential curve has been fitted through the calibration data and used over the entire PLIF measuring range, from pH 5 to 7.

The influence of the molar extinction coefficient variations as a function of pH on pixel intensity calibration expressed in equation (5.4) are shown in Figure (5.9), in the case of dissolved $CO_2$ concentration measurement in the wake of a free rising gas bubble. The correction is compared to the so called Stern-Volmer relationship corresponding to the calibration of intensities $\frac{I}{I_0}$ without correction for extinction coefficient variations.

As attenuation is decreasing with decreasing pH [19], non-corrected background images would result in overestimated calibrated pixel intensities as a function of pH.

Same results are presented differently in Figure (5.10), where $\frac{\phi_0 \varepsilon_0}{\phi \varepsilon}$ is given as a function of $[H^+]$, revealing the linear relationship predicted by Stern-Volmer.

It can be noted that the linear relationship predicted by the non-corrected Stern-Volmer relationship is only valid for a pH ranging from about 6 to 7, as illustrated in Figure (5.10).

Using the proposed corrected correlations (5.7) relating pixel intensities to pH, the acquired images are firstly transformed to pH levels and then to $CO_2$ concentrations levels using the calibration depicted in Figure (5.11).

Acquired images and $CO_2$ processed images are presented in Figure (5.12, A and B). Black areas appear to the left of the bubble when it shadows the laser light. $CO_2$ concentration variations in Figure (5.12, C) were obtained by subtracting the computed $CO_2$ concentration field obtained for an homogeneous concentration (5.12, B, t = 0s) from the $CO_2$ concentration field computed for different frames. The average initial $CO_2$ concentration was 1.3 $mg/L$ In Figure (5.12, D) a comparison is done between two calibrations taking or not taking into account extinction coefficient variations (see Section 5.2.2). Concentration variation profiles of horizontal and vertical sections are also plotted in Figure (5.13).

As can be seen in these figures, the simple and corrected calibrations differ

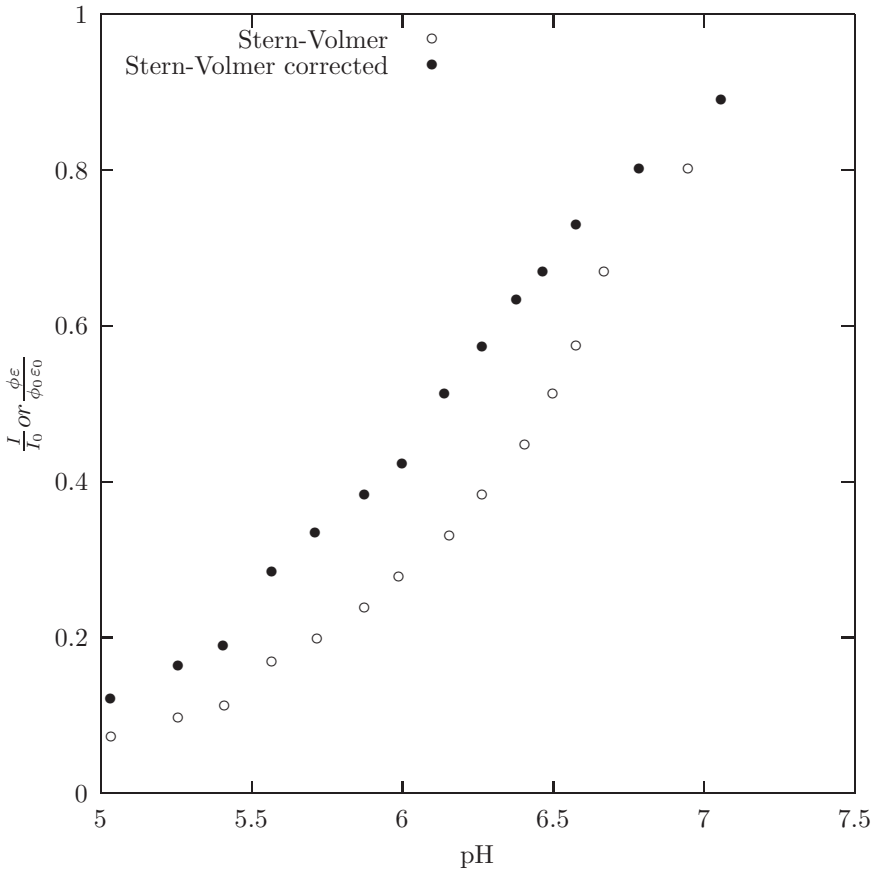


Figure 5.9: Example, for the central column of the image, of extinction coefficient variations effects on the calibration of $\frac{\phi\varepsilon}{\phi_0\varepsilon_0}$, with increasing pH.

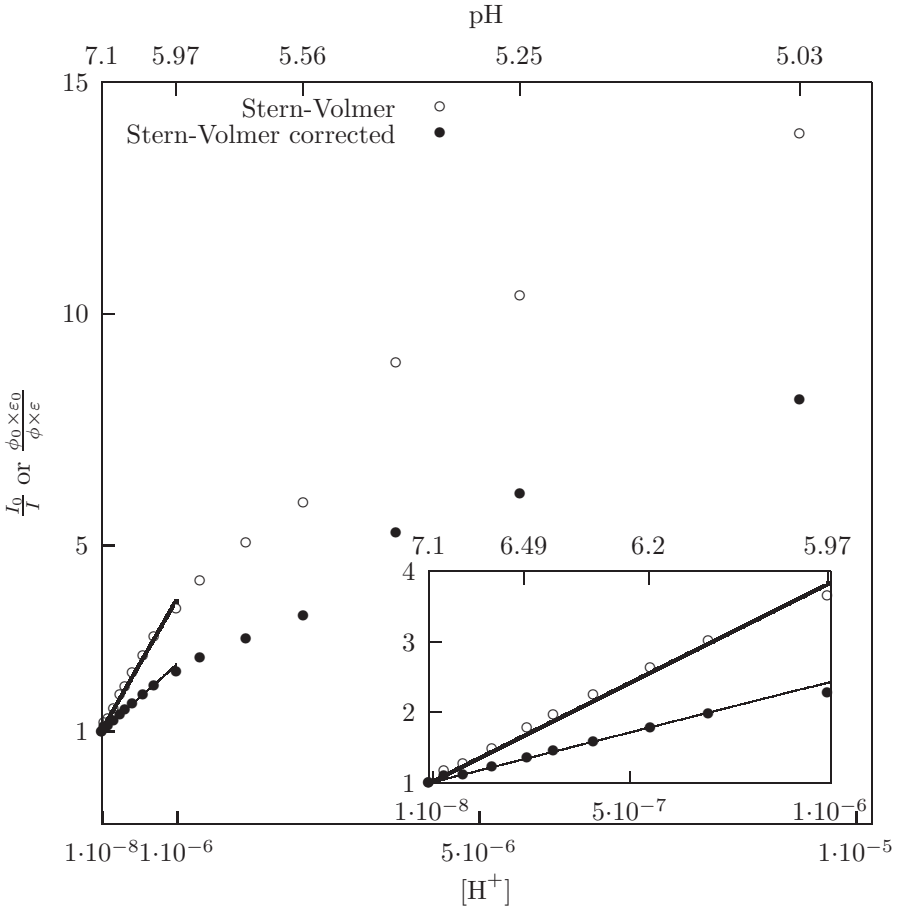


Figure 5.10: Example for the central column of the image of extinction coefficient variations effects on the calibration of $\frac{\phi_0 \varepsilon_0}{\phi \varepsilon}$ with Stern-Volmer linear relationship.

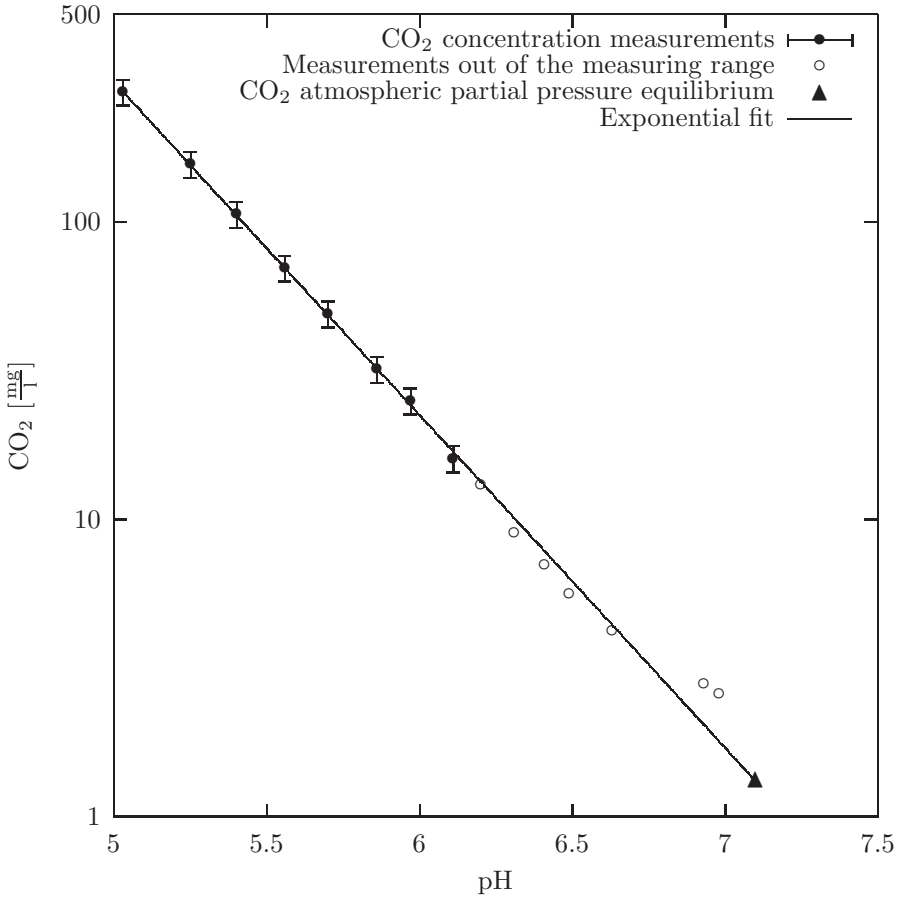


Figure 5.11: Calibration of $CO_2$ concentration as a function of pH in the tank using a Metler Toledo $CO_2$ InPro 5000 probe and pH equilibrium with atmosphere to complete the PLIF measuring range. Empty dots correspond to measurements below the manufacturer's specification operating limit of 14.7 $mg/L$.

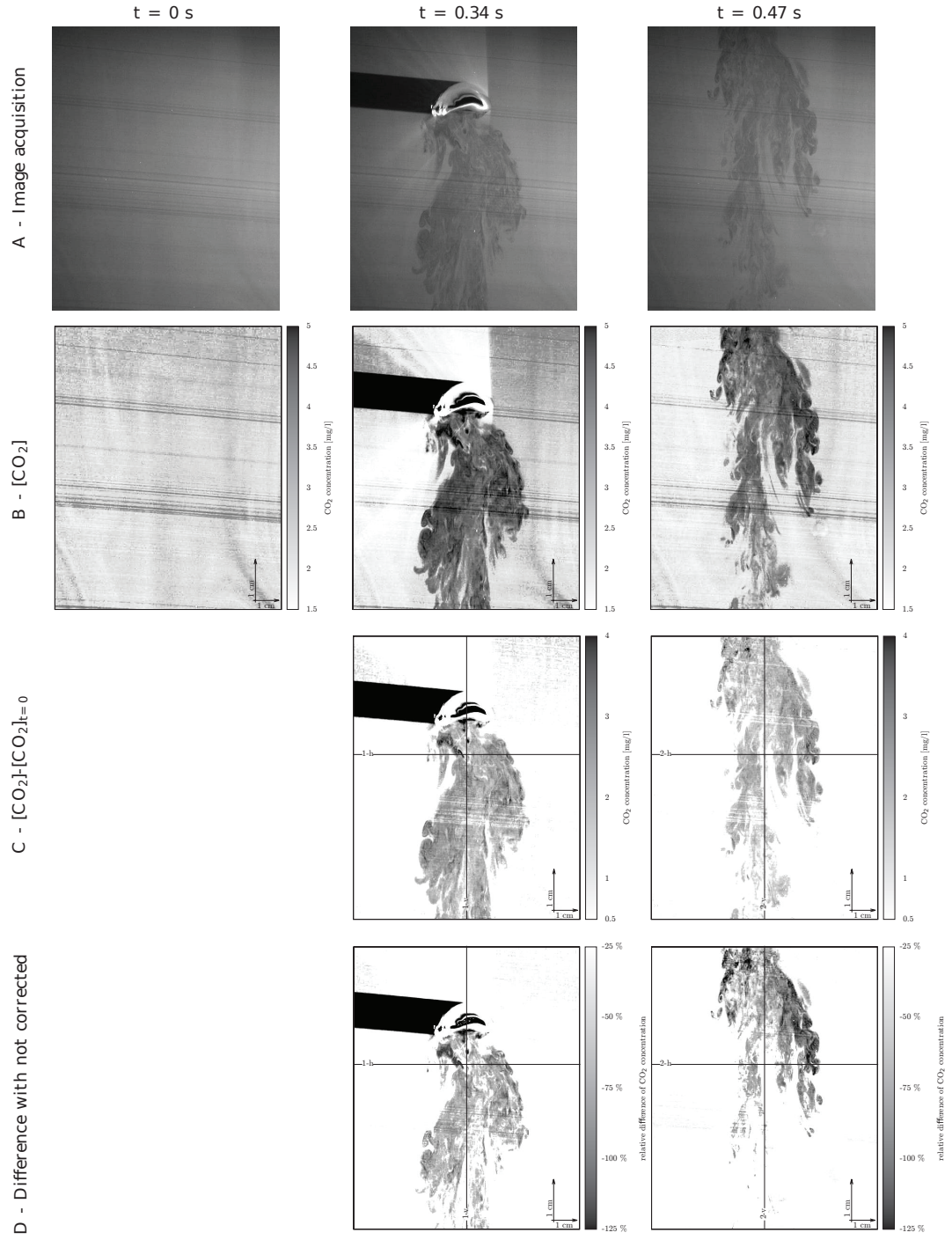


Figure 5.12: Example of application of the calibration on rising bubble images in raw A resulting in the transformed $CO_2$ concentration images in raw B. Subtracting the computed $CO_2$ concentration field obtained for an homogeneous concentration (raw B, t = 0s), $CO_2$ concentration increase maps are presented in raw C. Maps of the relative difference with a non-corrected calibration are presented in raw D.

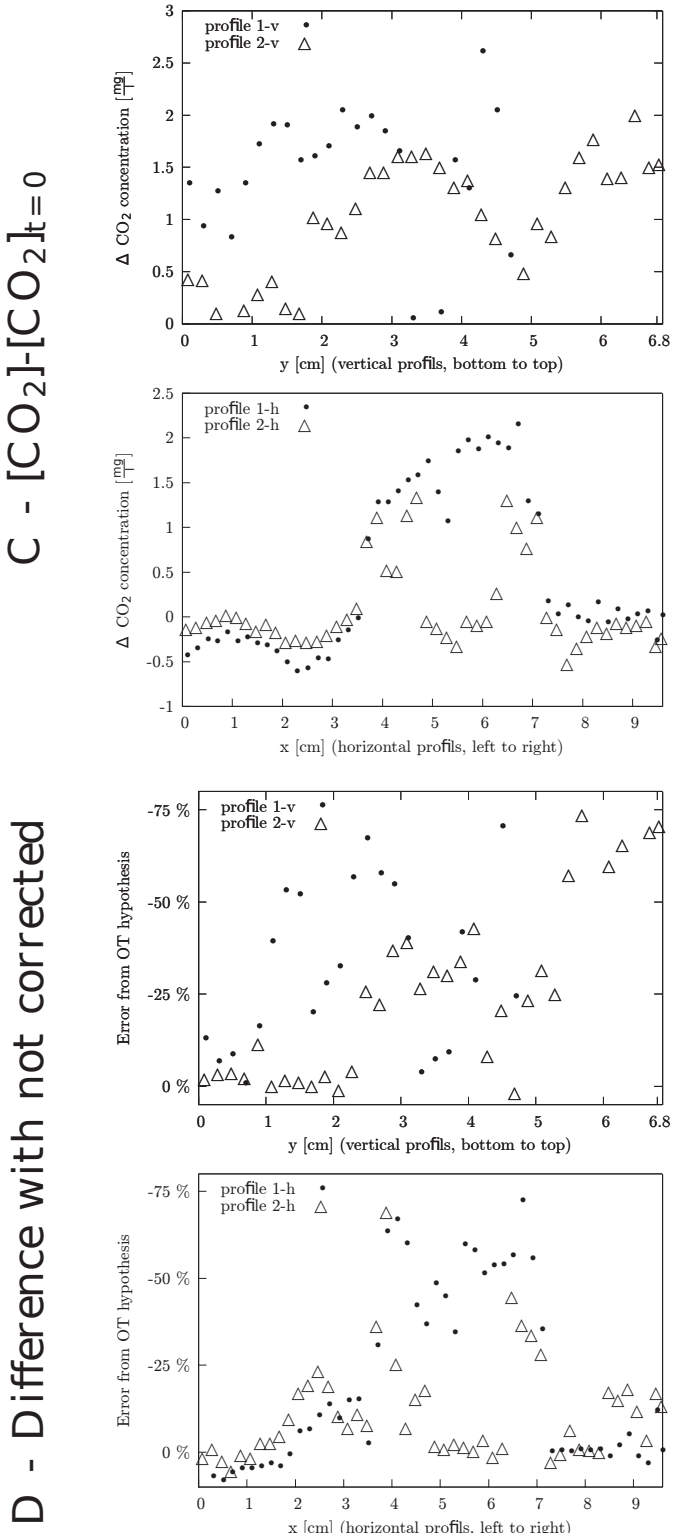


Figure 5.13: $CO_2$ concentration profiles from Figure (5.12) are presented in raw C. Profiles of the relative difference with a non-corrected calibration are presented in raw D.

most where the extinction coefficient variations are larger, that is to say in the bubble wake. The particular measurement application exhibits relative differences of concentration up to 125% in the bubble wake for the highest $CO_2$ concentrations.

The initial goal of this thesis concerns mass transfer in bubble columns. Therefore after the study of a simplified configuration of a single rising bubble, it is relevant to observe the dissolution of a bubble swarm, where pH variations occur on a large area. This case has been used to illustrate the interest of the second data treatment.

## 5.5 Illustration of the need for the second data treatment

The implementation of an experimental setup that will be used to illustrate the interest of the second proposed correction will now be described. In this case, the length over which pH variations are observed is significant, thus $(c\int_{L_{pH\neq pH_{ref}}}(\varepsilon_{ref}-\varepsilon)dr)$ can no longer be neglected. Qualitative results have been obtained, showing that extinction coefficient variations in the measurement region can affect measurements. This situation requires the proposed correction taking into account fluorescence extinction variations in the measurement region, and called here Data treatment 2.

### 5.5.1 Experimental setup

This experiment aims at creating a large scalar gradient area. Variations of $CO_2$ concentration are observed in the wake of a 99.7% pure $CO_2$ gas bubble cloud rising in the middle of a transparent tank with a square cross-section of 210 *mm* side. An overview of the experimental setup is described in Figure (5.14).

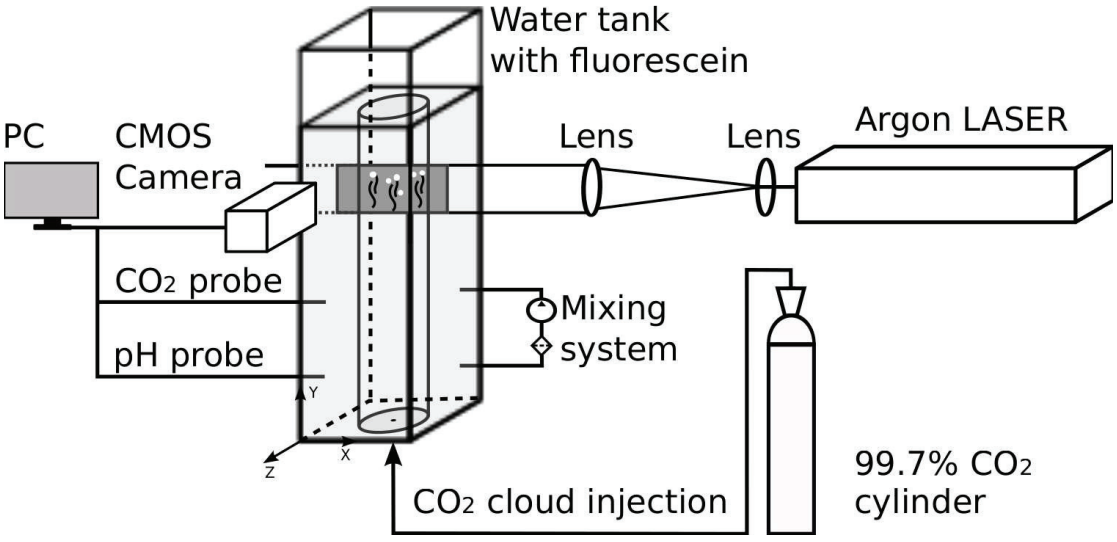


Figure 5.14: Schematic view of the Planar Laser Induced Fluorescence experimental set-up used for $CO_2$ concentration measurements. $CO_2$ concentration is observed in the wake of a free rising $CO_2$ bubble swarm dissolving into an aqueous solution of fluorescein sodium illuminated by an argon laser plane.

The bubble swarm is rising within a 94 *mm* inner diameter cylindrical tube

placed in the middle of the water tank. Before each experiment, the liquid surrounding the tube is agitated so that the pH and $CO_2$ concentration are homogeneous. As represented in Figure (5.15), the tube delimits the flow region (inside) and the control region (outside).

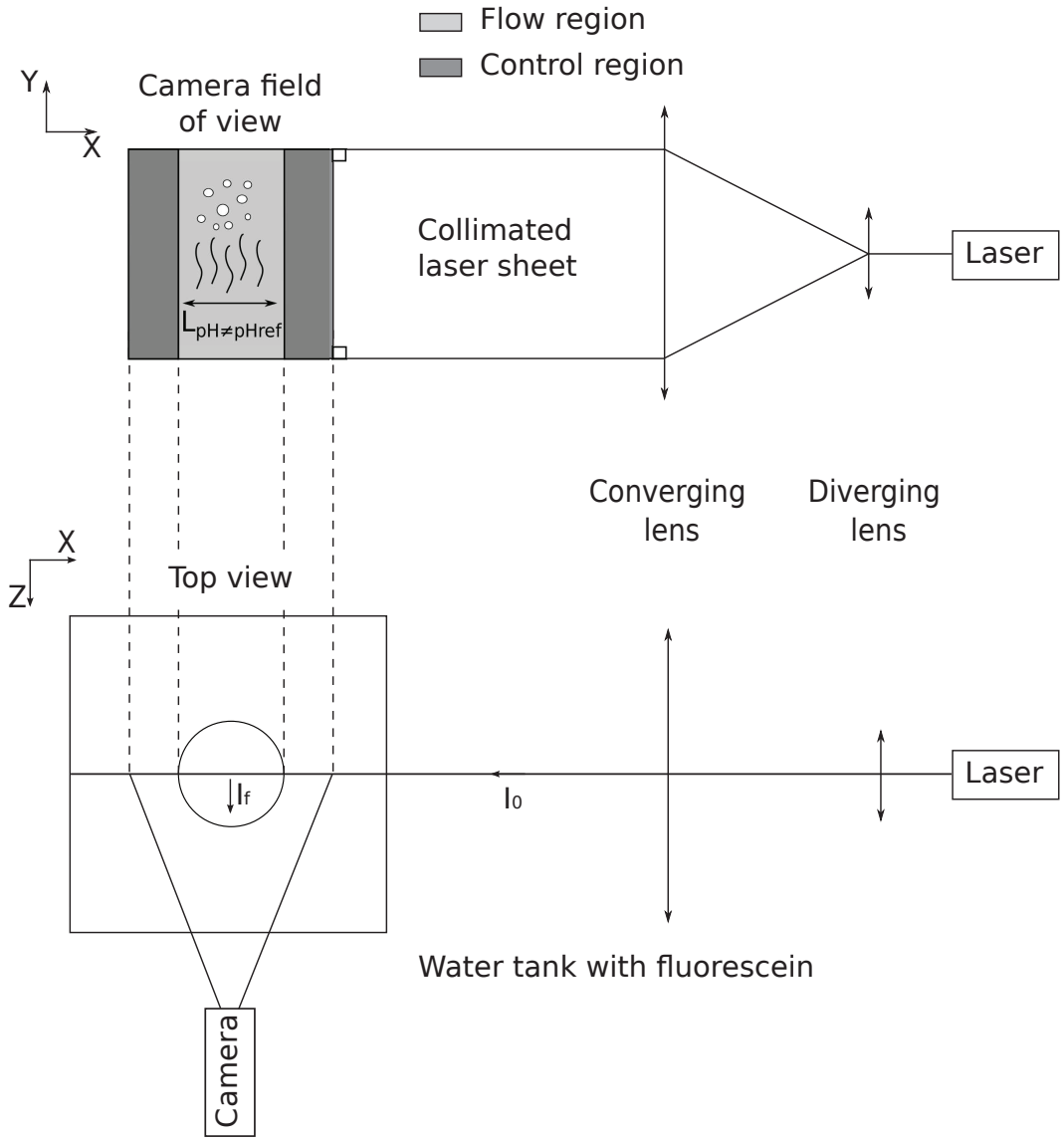


Figure 5.15: Schematic view of the camera observation area. The cylinder bounds the control region with a known and homogeneous $CO_2$ concentration and the flow region in which the $CO_2$ concentrations are observed.

The tank is filled with 22 litres of demineralized water (total hardness $<$

17.8 $ppm = 1.56\ \mu S/cm$) containing $5 \times 10^{-7} \pm 0.1\%\ mol/L$ of dissolved fluorescein sodium. As previously, fluorescein sodium ($C_{20}H_{10}Na_2O_5$, CAS: 518-47-8) has been selected as the fluorescent dye due to the strong pH dependence of its absorption and emission properties in aqueous solution.

As in Section 5.4, a 4 $W$ Argon-Ion laser, mounted with a 488 $nm$ bandpass filter, is used for the excitation of the fluorescein sodium dye. One cylindrical lens and one spherical lens (300 $mm$ focal, 80 $mm$ in diameter) are used to obtain a collimated sheet.

Re-emitted fluorescence intensity variations induced by pH variations in the laser sheet are recorded using a Dalsa Falcon 1.4M100 HG CMOS 8-bit camera set at a frequency of 500 frames per second. Those variations are induced by the reaction of water with the dissolved $CO_2$ in the wake of the bubble swarm.

### 5.5.2 Application to the wake of a free rising bubble swarm

Image acquisition, calibration and treatment are identical to those described in Section 5.3. First a reference pH frame has been recorded just before the bubble cloud was released, then the phenomenon has been measured, and finally, pH, $CO_2$ concentration and frames with a homogeneous concentration were recorded for increasing $CO_2$ concentrations.

In Figure (5.16), it is qualitatively shown that variations of attenuation within the measurement zone can affect PLIF intensity measurements. The average 8-bit grayscale values in 4 control regions are indicated in the white dashed boxes of $165 \times 75\ pix^2$. A reference picture with homogeneous pH and $CO_2$ concentration in both the flow and the control region is shown in picture A). The free rising bubble swarm used to vary the pH is shown in image B) while it is crossing the flow region. The effect of attenuation variation in the flow region can be seen in picture C): the flow region with a lower pH will result in a lower attenuation of the laser. The control region, $R_C$, on the right side of image C) has indeed a higher intensity than the one in the control region, $R_A$, on the right side of the reference image A) while the pH and $CO_2$ concentration has remained the same. The average 8-bit grayscale value in the control region $R_C$ is 158.8, while it is only 147.7 in the control region $R_A$. Thus, in this case, a correction for variations of extinction coefficient with pH is shown to be necessary while the observed dimensions are of the order of 100 $mm$.

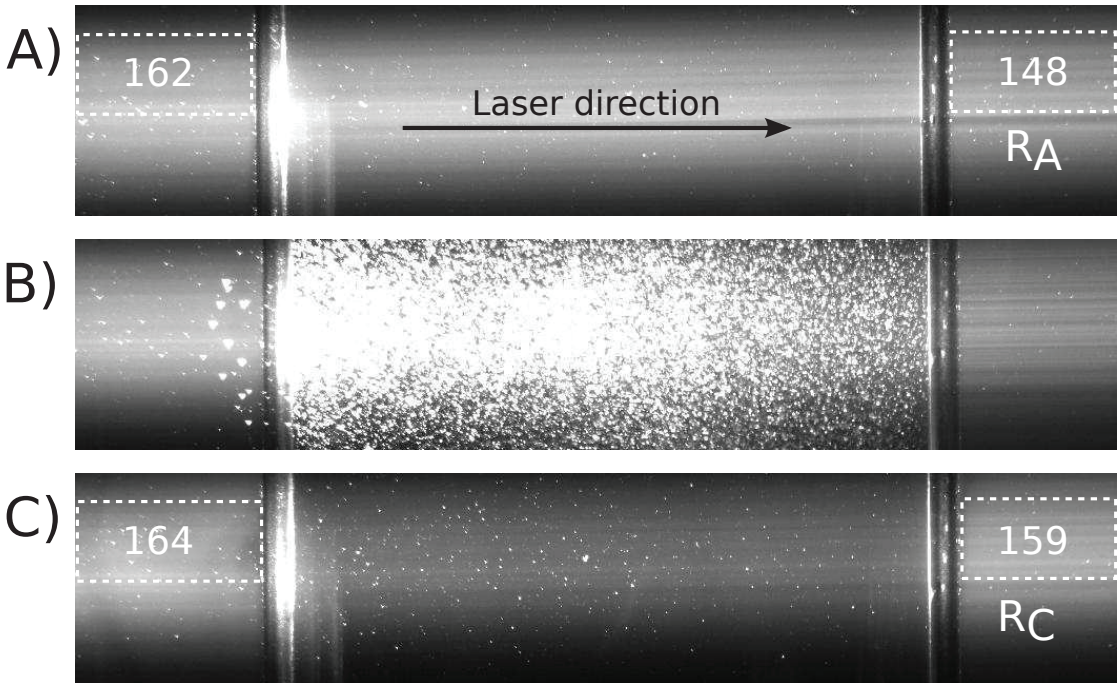


Figure 5.16: Illustration of a situation where the proposed data treatment procedure is necessary. In picture A), pH and $CO_2$ concentrations are known and homogeneous in both the flow and the control region. In image B), the free rising bubble swarm is captured while it goes through the flow region. In picture C), the effect of extinction coefficient variations in the flow region can be observed: the control region, $R_C$, on the right side is less attenuated than in the control region, $R_A$, on the right of image A).

## 5.6 Experimental determination of $k_l$ coefficient

A quantitative analysis of mass transfer has been done from the PLIF measurements carried out in Section 5.4.2.

The studied bubble has been considered as a spherical cap of width 2.18 $cm$ and height 0.625 $cm$, rising at $23.5 \pm 0.5$ $cm/s$. Concentrations measured in the wake of the observed bubble vary between about 1 to 3.5 $cm/s$ as can be seen in Figure (5.12, C).

From the mass transfer correlation for spherical cap bubbles reported in Calderbank and Lochiel [3], mass transfer coefficients for the observed bubble are theoretically estimated to be between 0.025 and 0.029 $cm/s$.

From our work, the experimental mass transfer coefficient $k_l$ in the bubble wake is predicted to be 0.017 $cm/s$, using the following equation:

$$k_l = \frac{[CO_2] \times \pi \times a^2 \times V_b}{\Delta C \times A_{sc}}$$

where $[CO_2]$ is the measured concentration (chosen value: 2.5 $mg/L$), $\Delta C$ is the $CO_2$ concentration gradient (estimated to be $1.45 \pm 0.01$ $g/L$ using the same approach as in [26]), $A_{sc}$ stands for the spherical cap area ($8.69 \pm 0.05$ $cm^2$) [3], $a$ is the semi-width of the bubble ($1.09 \pm 0.02$ $cm$), and $V_b$ is the rising velocity of the bubble computed optically from the acquisition frequency and the spatial calibration.

While a non-corrected calibration would result in smaller mass transfer coefficient $k_l$, the proposed concentration measurement still disagrees with the prediction of Calderbank and Lochiel [3] by a factor of 1.6. As pictured by the red squares in Figures (5.17) and (5.18), experimentally determined $k_l$ and $k_l a$ values are slightly lower than reported results from [3].

Frossling's model [11] for rigid interface (i.e. contaminated medium) leads to $k_l$ theoretical value of 0.014 $cm/s$ using formula 5.8:

$$k_l = c\sqrt{\frac{V_b}{d_{eq}}} D^{\frac{2}{3}} \nu^{-\frac{1}{6}} \tag{5.8}$$

where $c \approx 0.6$ (from Vasconcelos *et al* [28]), $d_{eq}$ is the equivalent diameter of the bubble (1.73 $cm$), $D$ is the carbon dioxide diffusivity in water (0.16 $m^2/s$) and $\nu$ is the water kinematic viscosity ($10^{-6}$ $m^2/s$).

Since the experimental conditions where found to be close to those obtained for pure water (see Figure (5.8)), the interface should be mobile and the corresponding model is based on Higbie's [13] theory for mobile interface. This leads to the penetration model solution 5.9 of Bird, Stewart and Lightfoot [2]:

$$k_l = 1.13\sqrt{\frac{V_b}{d_{eq}}} D^{\frac{1}{2}} \tag{5.9}$$

giving a $k_l$ value of 0.017 $cm/s$, which is exactly the value determined from the experimental procedure of this work. This suggests that experiments where carried out in pure water.

These encouraging results confirm that PLIF optical technique is suitable for mass transfer studies. The proposed procedure leads to mass transfer coefficients in accordance with known theoretical models. The interfacial area $a$ can be determined by measuring void fraction and bubbles average diameter. Finally, the product $k_l \times a$ can be computed, giving the global mass transfer in bubble columns.

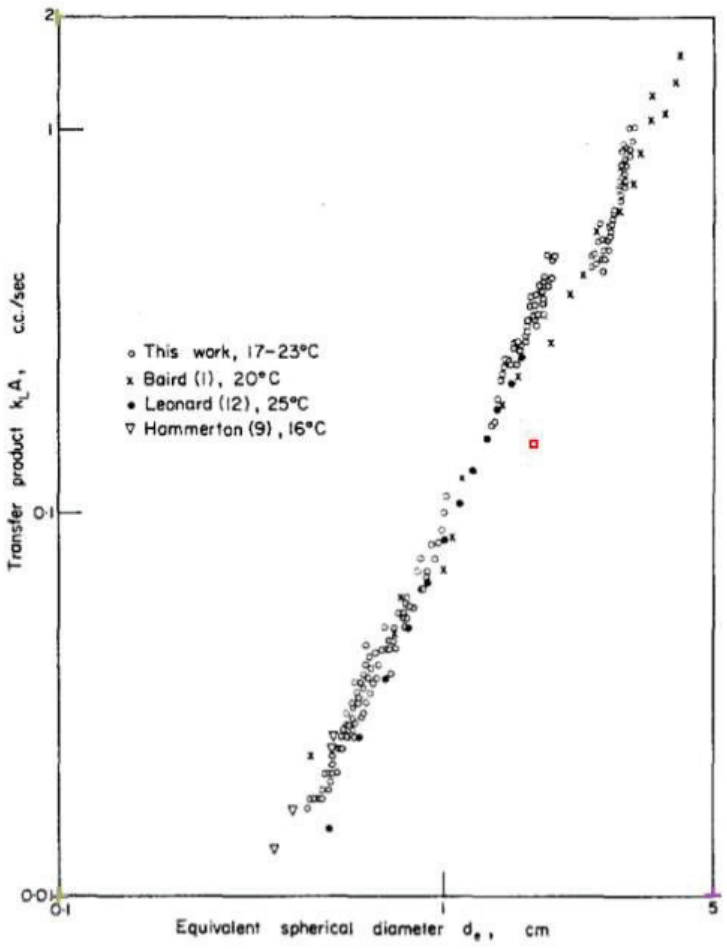


Figure 5.17: Mass transfer product $k_l a$ for carbon dioxide bubbles in water from Calderbank and Lochiel [3]. Result of the present work is in red square.

## 5.7 Conclusion

Two PLIF data treatments taking into account variations of the fluorescence extinction coefficient due to pH have been developed, allowing for more precise scalar field measurements.

A correction for attenuation during PLIF calibration taking into account the extinction coefficient variations with pH has first been presented. An application to dissolved $CO_2$ concentration measurements in the wake of a free rising bubble has been shown, demonstrating the error that may be induced if extinction coefficient variations with pH during calibration are not taken into account. This

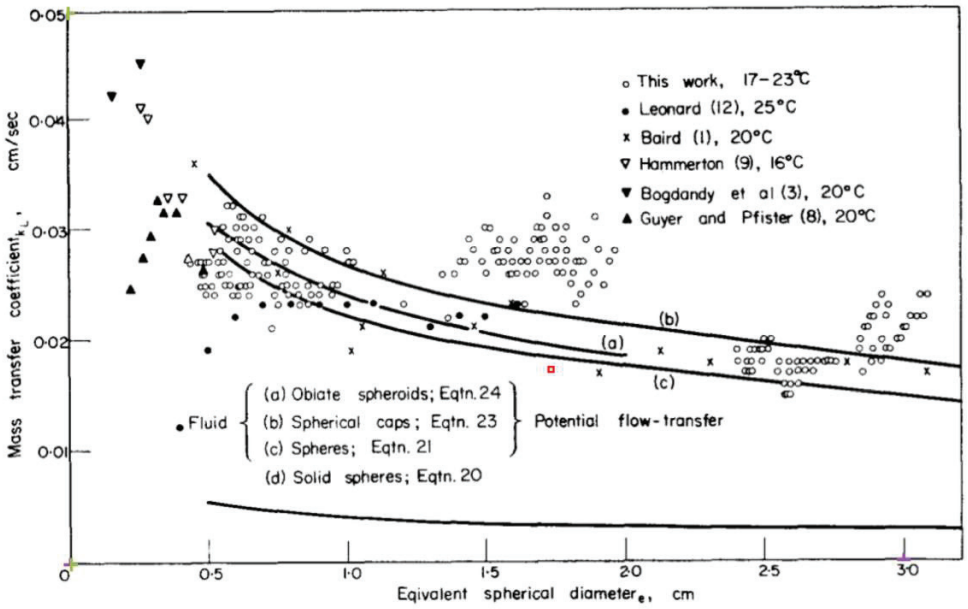


Figure 5.18: Transfer coefficient for carbon dioxide bubbles in water from Calderbank and Lochiel [3]. Result of the present work is in red square.

proposed correction method should be applied when the product $L_{fluo}c(\varepsilon_{ref} - \varepsilon)$ is not negligible. It allows for the PLIF to be used for a wider range of parameters, for example higher fluorescein sodium concentrations and larger distances in the liquid for large tank experiments.

A second complementary PLIF correction taking into account variations of the fluorescence extinction due to pH variations in the measurement region has been presented. This proposed correction method should be applied when the length of the measurement region becomes significant (i.e. when $(c\int_{L_{pH\neq pH_{ref}}}(\varepsilon_{ref} - \varepsilon)dr)$ cannot be neglected). Correcting these extinction coefficient variations in the measurement region allows for the PLIF method to be used for wider measurement regions. The interest of this correction has been illustrated on a benchmark with a control region where pH is known. It has qualitatively been shown that extinction coefficient variations in the measurement region can affect measurements even if the measurement region is only of the order of 100 $mm$. The need for the proposed correction can be evaluated very efficiently using a similar experiment confining pH variations within the measurement region.

# Bibliography


[1] Asher, W., Litchendorf, T.: Visualizing near-surface concentration fluctuations using laser-induced fluorescence. Experiments in Fluids **46**(2), 243–253 (2009)

[2] Bird, R. B., Stewart, W. E., Lightfoot, E. N.: Transport phenomena. New York: Wiley 537–542(1960)

[3] Calderbank, P.H., Lochiel, A.C.: Mass Transfer Coefficients, Velocities and Shapes of Carbon Dioxide Bubbles in Free Rise Through Distilled Water. Chemical Engineering Science **19**(7), 485–503 (1964)

[4] Clift, R., Grace, J., Weber, M.: Bubbles, drops, and particles, vol. 3. Academic press New York (1978)

[5] Crimaldi, J.: Planar laser induced fluorescence in aqueous flows. Experiments in Fluids **44**(6), 851–863 (2008)

[6] Dani, A.: Transfert de masse entre une bulle et un liquide: simulations numériques directes et fluorescence induite par nappe laser. Thesis of Institut National des Sciences Appliquées (INSA) de Toulouse (2007)

[7] Deshpande, K., Zimmerman, W.: Simulation of interfacial mass transfer by droplet dynamics using the level set method. Chemical Engineering Science **61**(19), 6486–6498 (2006)

[8] Fdhila, R., Duineveld, P.: The effect of surfactant on the rise of a spherical bubble at high reynolds and peclet numbers. Physics of Fluids **8**, 310 (1996)

[9] Feuerstein, D.L., Selleck, R.E.: Fluorescent tracers for dispersion measurements. J. Sanit. Eng. Div. Am. Soc. Civ. Eng **89**, 1–21 (1963)

[10] Figueroa-Espinoza, B., Legendre, D.: Mass or heat transfer from spheroidal gas bubbles rising through a stationary liquid. Chemical Engineering Science **65**(23), 6296–6309 (2010)

[11] Frossling, N.: Ubber die verdunstung fallenden tropfen (Evaporation of falling drops). Gerlands Beitage zur Geophysik, (52) 170–216 (Griffith (1960) Mass transfer from drops and bubbles. Chemical Engineering Science, **12** 198–213)(1938)

[12] Guilbault, G. G.: Practical Fluorescence: Theory, Methods and Techniques. New York: M.Dekker (1973)

[13] Higbie, R.: The rate of absorption of a pure gas into a still liquid during a short time of exposure. Transactions of the American Institute of Chemical Engineers, **31** 365–389 (1935)

[14] Jirka, G.: Application of LIF to investigate gas transfer near the air-water interface in a grid-stirred tank. Experiments in Fluids **37**(3), 341–349 (2004)

[15] Jirka, G., Herlina, H., Niepelt, A.: Gas transfer at the air-water interface: experiments with different turbulence forcing mechanisms. Experiments in Fluids **49**(1), 319–327 (2010)

[16] Karasso, P., Mungal, M.: PLIF measurements in aqueous flows using the nd: YAG laser. Experiments in Fluids **23**(5), 382–387 (1997)

[17] Krishna, R., Urseanu, M.I., Van Baten, J.M., Ellenberger, J.: Wall effects on the rise of single gas bubbles in liquids. International communications in heat and mass transfer **26**(6), 781–790 (1999)

[18] Leonhardt, H., Gordon, L., Livingston, R.: Acid-base equilibriums of fluorescein and 2', 7'-dichlorofluorescein in their ground and fluorescent states. The Journal of Physical Chemistry **75**(2), 245–249 (1971)

[19] Lindqvist, L.: A flash photolysis of fluorescein. Arkiv for Kemi **Band 16**(nr 8), 60 (1960)

[20] Melton, L., Lipp, C.: Criteria for quantitative PLIF experiments using high-power lasers. Experiments in Fluids **35**(4), 310–316 (2003)

[21] Roudet, M.: Hydrodynamique et transfert de masse autour d'une bulle confinée entre deux plaques. Thesis of Institut National des Sciences Appliquées (INSA) de Toulouse (2008)

[22] Sarathi, P., Gurka, R., Kopp, G., Sullivan, P.: A calibration scheme for quantitative concentration measurements using simultaneous PIV and PLIF. Experiments in Fluids **52**(1), 247 (2012)

[23] Simoens, S., Ayrault, M.: Concentration flux measurements of a scalar quantity in turbulent flows. Experiments in Fluids **16**(3-4), 273–281 (1994)

[24] Sjöback, R., Nygren, J., Kubista, M.: Absorption and fluorescence properties of fluorescein. Spectrochimica Acta Part A: Molecular and Biomolecular Spectroscopy **51**(6), L7–L21 (1995)

[25] Stöhr, M., Schanze, J., Khalili, A.: Visualization of gas-liquid mass transfer and wake structure of rising bubbles using pH-sensitive PLIF. Experiments in Fluids **47**(1), 135–143 (2009)

[26] Valiorgue, P., Hajem, M. El, Vassilev, A., Botton, V., Hadid, H. Ben: Elongated gas bubble dissolution under a turbulent liquid flow. Chemical Engineering and Processing: Process Intensification **50**(8),854–858 (2011)

[27] Variano, E.A. and Cowen, E.A.: Quantitative Imaging of CO2 Transfer at an Unsheared Free Surface, in Transport at the air-sea interface : measurements, models and parametrizations, edited by Garbe, C., Handler, R., Jöhne, B. Springer Verlag (2007)

[28] Vasconcelos, J.M.T., Rodriguesa, J.M.L., OrvalhoaS, C.P., Alvesa, S.S., Mendesb, R.L., Reis, A.: Effect of contaminants on mass transfer coeffcients in bubble column and airlift contactors. Chemical Engineering Science **58**,1431–1440 (2003)

[29] Walker, D.: A fluorescence technique for measurement of concentration in mixing liquids. Journal of Physics E: Scientific Instruments **20**, 217 (1987)

[30] Wylock, C., Larcy, A., Colinet, P., Cartage, T., Haut, B.: Direct numerical simulation of bubble-liquid mass transfer coupled with chemical reactions: Influence of bubble shape and interface contamination. Colloids and Surfaces A: Physicochemical and Engineering Aspects, Volume 381, p130–138 (2011)

# Conclusion

Gas-liquid mass transfer has been investigated and improvements have been proposed to enhance exchange capabilities in vertical bubble columns. It is essential to understand the phenomena and parameters involved before scale up.

This Ph.D report is composed of five chapters gathered in three parts dealing successively with bubble columns, Micro-Bubble Generators, and Planar Laser-Induced Fluorescence.

In the first chapter, after an introduction to the main features and applications of bubble columns, the physic of mass transfer and contamination have been discussed from a theoretical point of view, and limitations of the study have been defined.

As described in chapter two, columns have a large amount of parameters that influence the physical phenomena involved. An experiment of desaturation has been carried out to quantify the improvement of the gas-liquid exchange when the column of the LMFA is in operation. Gas-liquid mass transfer was found to be much faster due to the larger exchange surface resulting from the presence of small bubbles injected into the column. In addition, gas circuit has been modified for a closed-loop study, similar to the functioning of a set of columns in series, and an associated theoretical model has been implemented. These works highlight the importance of the gas-liquid interfacial area for mass transfer.

Chapter three describes the various physical phenomena that apply to bubbles, and the associated dimensionless numbers. A State of the Art Micro-Bubble Generators(MBG) has been exposed and since no satisfactory solution has been found, a new MBG has been designed.

An innovative high-speed rotating MBG has been presented in chapter 4. Experimental works attest that the prototype can produce micro-bubbles of average diameter $D_{bubble} = 0.252\ mm$. Performances have been characterized using rotational Reynolds, $\chi$ and Eötvös dimensionless numbers. The invention has been officially declared (patent pending). The installation of such device in bubble columns should lead to a significant increase in gas-liquid interfacial area, and therefore mass transfer.

The last chapter aims at improving data treatment methods for Planar Laser-

Induced Fluorescence (PLIF), which enables to obtain experimentally mass transfer coefficient $k_l$ through concentration measurements. Two PLIF data treatments taking into account variations of the fluorescence extinction coefficient due to pH have been developed.

The first presented correction takes into account variations of the fluorescence extinction due to pH during the calibration step, and has been evaluated on $CO_2$ concentration measurement in the wake of a free rising bubble. It allows for the PLIF to be used for a wider range of parameters, for example higher fluorescein sodium concentrations and larger distances in the liquid for large tank experiments.

The second proposed correction should be applied when the length in the measurement region over which pH variations are observed increases: variations of the extinction coefficient will affect the local incident light intensity and therefore the measurements. It has qualitatively been shown that extinction coefficient variations in the measurement region can affect measurements even if the measurement region is only of the order of $100mm$. The need for this correction has been illustrated in the wake of a cloud of free rising bubbles.

# Appendix

## .1 Amon Planar Laser-Induced Fluorescence (PLIF) software

### .1.1 Applications

A PLIF treatment software named Amon has been implemented using Matlab(C). The graphical user interface (GUI), pictured in Figure (19), enables the user to transform one PLIF image using a set of PLIF calibration images and their respective scalar values (e.g. pH, temperature, $CO_2$ concentration, etc.).

This tool has been developed during this thesis, but can now be used freely in the laboratory. Students in their final year of research master generally have PLIF lab works. They could use this software to plot images easily.

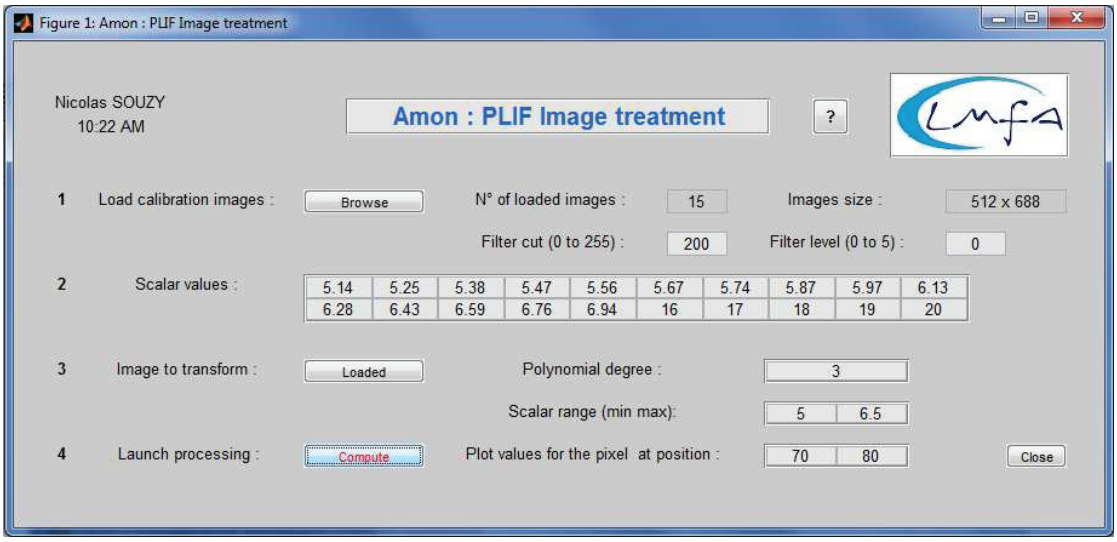


Figure 19: The graphical user interface of Amon.

## .1.2 Computation

From a mathematical perspective, the program collects the greyscale values of each pixel of the loaded images in a 3D matrix of size:

$$L_{img} \times W_{img} \times N_{call}$$

where $L_{img}$ is the loaded image length, $W_{img}$ is the loaded image width, and $N_{call}$ is the number of loaded calibration images.

Step 1: the user selects the calibration images by clicking on Browse. All loaded images must be in .jpg format and have the same pixel dimensions. Calibration images must be loaded with monotonically changing values (increasing or decreasing magnitude order). A filter can be applied to smooth out calibration images: if the grey level of a pixel is over the threshold, then its value will be replaced by the average value of the surrounding pixels. A filter level of 0 will not modify the original image. Filter 1 will calculate the value of pixel (i,j) using the values of the pixels from i-1 to i+1 and j-1 to j+1 (3x3 matrix). Filter level can be used up to level 5 which will use the values of the pixels from i-5 to i+5 and j-5 to j+5 (11x11 matrix) to calculate an average value, resulting in a highly blurred image (see Figure (20). The size and the number of loaded calibration images are indicated on the GUI.

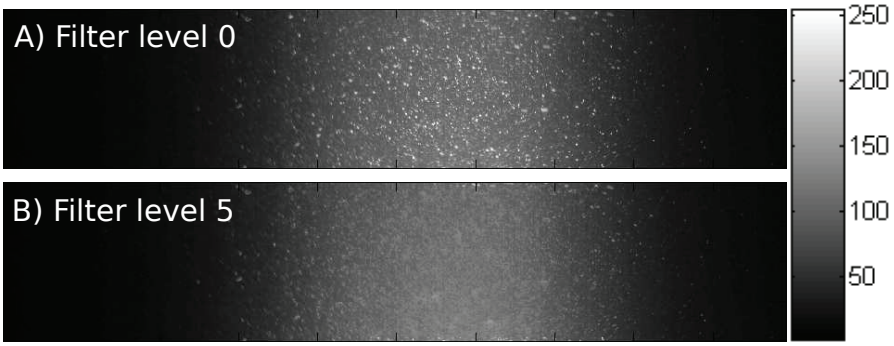


Figure 20: Comparison of filter levels. Picture A is the original calibration image without modification, i.e. filter level 0. Setting a filter level of 5 results in the blurred image B.

In step 2, scalar values must be entered, with scalar number i corresponding to loaded calibration image number i. It is possible to enter up to 20 scalars ($N_{call} \leq 20$). If $N_{call}$ images are loaded, only the first $N_{call}$ scalar values will be used by the program. Scalar values are gathered in a vector that will be used in step 4.

Step 3 consists in loading the image to transform (one only). The greyscale values of each pixel of the loaded image are saved in a $(L_{img} \times W_{img})$ matrix. It is possible to select the degree of the polynomial function that will be used for interpolation. The user can select the min–max range of the color bar.

When step 1, 2 and 3 are completed, the user can start step 4 and launch computation. For each pixel, a polynomial is created with 'polyfit' function, using the scalar vector and the greyscale value of the pixel through all the calibration images. Therefore, a polynomial is associated to each pixel, relating $N_{call}$ greyscale values to $N_{call}$ scalar values. These polynomials are then applied to each pixel of the image to transform, using the 'polyval' function. Based on the calibration set, the interpolation function of a pixel links its greyscale value to one scalar value. The result is a transformed image matrix. This matrix is a scalar map taking into account the specific evolution of each pixel. Before computing, one can choose the degree of the polynomial that will be used for interpolation. It is also possible to plot the greyscale value of a specific pixel (at chosen position (i,j)) through all the calibration images, allowing for the verification of the monotonic evolution.

## .1.3 Polynomial degree for interpolation

A higher degree for the polynomial function will result in a better fit between greyscale and scalar values. Though, this will also propagate errors due to non-homogeneous images. For example, if calibration images contain reflecting particles (PIV tracers), a lower polynomial degree will smooth out light intensity irregularities and may give better scalar maps. The result for 3 different polynomial degrees are presented in Figure (21). In this case dissimilarities are not obvious, yet computation time is significantly longer for higher degrees. Thus, the software user should first launch processing using linear interpolation (first degree), and increase polynomial degree only if needed.

## .1.4 User manual

A number of recommendations are available in a user manual that can be displayed by clicking on the help button:

### 1->Load calibration images

Choose the calibration images by clicking on Browse. All loaded images must be in .jpg format and have the same pixel dimensions. Calibration images must be loaded with monotonically changing values (increasing or decreasing magnitude order). A filter can be applied to smooth out calibration images: if the grey level of a pixel is over the threshold, then its value will be replaced by the average

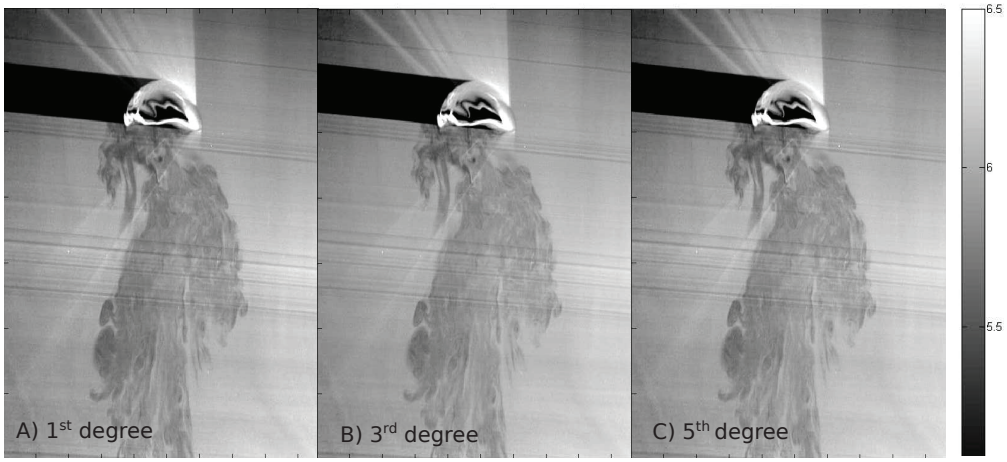


Figure 21: Set of transformed images: picture A results from a linear interpolation, image B and C were computed using $3^{rd}$ and $5^{th}$ degree polynomial interpolation.

value of the surrounding pixels. A filter level of 0 will not modify the original image, while a filter level of 5 will use the 11x11 surrounding pixels to calculate an average value, resulting in a highly blurred image.

**2->Scalar Values**

Enter scalar values by increasing or decreasing magnitude order (20 maximum), in accordance with loaded calibration images.

**3->Image to transform**

You can only transform one image at a time. It is possible to select the degree of the polynomial function that will be used for interpolation. The user can select the min/max range of the color bar.

**4->Launch processing**

Click on Compute to launch computing and display the transformed image. Greyscale values versus calibration number of a pixel at position (i,j) will also be plotted, in order to verify the monotonic evolution.

## .1.5 Test and limits of the software: application to simultaneous PLIF and PIV experiments

In order to study the link between flow and mass transfer (see Section 1.3), simultaneous PLIF and PIV imaging experiments have been carried out. The observed phenomenon is a set of free rising bubbles regularly released by a Labmda Vit-Fit syringe pump. ROI was illuminated by an argon laser (see Section 4.5.1), and single-frame recording has been done by the Falcon camera as described in Section 5.4.1. The medium has been seeded with 10 $\mu m$ DANTEC Dynamics Hollow Glass Spheres (HGS), and contained sodium fluorescein as described in Section 5.2.1.

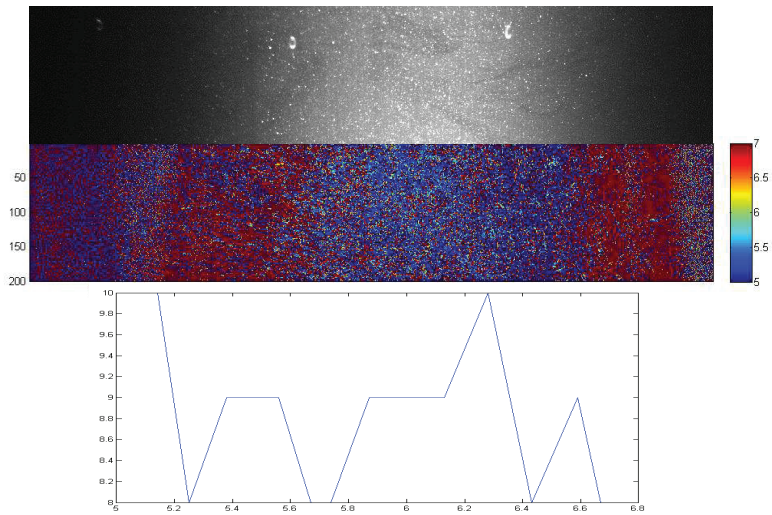


Figure 22: Original and transformed images containing reflecting particles for PIV. Interpolation has been done with $3rd$ degree polynomial, and filter level 5 has been applied to pixels over 200 light intensity.

Figure (22) presents an image where fluorescence extinction in the wake of the bubbles is visible. The medium is seeded with reflecting particles for PIV. The set of calibration images also contain HGS. A filter of level 5 has been applied to smooth greyscale values. Threshold has been fixed at 200 (255 is white), and interpolation has been done with $3rd$ degree polynomial. Nonetheless, intensity non-uniformities lead to a non-monotonic evolution of greyscale values for a pixel through the set of calibration images, as shown in the graph of Figure (22). Polynomial interpolation is distorted, resulting in a senseless transformed image.

Thus, it seems essential to capture homogeneous calibration images to achieve PLIF treatment. An optical system including a filter removing HGS reflections should give better results.

# .2 Experimental mean bubble diameters (m)

| $D_{wall} = 100\ mm$ | $r_{bent} = 5\ mm$ | $r_{bent} = 10\ mm$ | $r_{bent} = 13\ mm$ |
|---|---|---|---|
| $\omega = 904\ rad/s$ | 0,0008883467 | 0,0008061226 | 0,0008750898 |
| $\omega = 1095\ rad/s$ | 0,0010499392 | 0,0009660159 | 0,0003203148 |
| $\omega = 1172\ rad/s$ | 0,0012109743 | 0,0012220696 | 0,0002974352 |
| $D_{wall} = 150\ mm$ | $r_{bent} = 5\ mm$ | $r_{bent} = 10\ mm$ | $r_{bent} = 13\ mm$ |
| $\omega = 904\ rad/s$ | 0,0004003935 | 0,0004461528 | 0,0002859954 |
| $\omega = 1095\ rad/s$ | 0,0004461528 | 0,0003431944 | 0,0002974352 |
| $\omega = 1172\ rad/s$ | 0,0003889537 | 0,0002974352 | 0,0002974352 |
| $D_{wall} = 200\ mm$ | $r_{bent} = 5\ mm$ | $r_{bent} = 10\ mm$ | $r_{bent} = 13\ mm$ |
| $\omega = 904\ rad/s$ | 0,0009094113 | 0,0004232731 | 0,0002402361 |
| $\omega = 1095\ rad/s$ | 0,0014768749 | 0,0004232731 | 0,0002516759 |
| $\omega = 1172\ rad/s$ | 0,000491912 | 0,0003317546 | 0,0002631157 |

Table 1: Mean bubble diameters (m)

| $D_{wall} = 100\ mm$ | $r_{bent} = 5\ mm$ | $r_{bent} = 10\ mm$ | $r_{bent} = 13\ mm$ |
|---|---|---|---|
| $\omega = 904\ rad/s$ | 0,000423 | 0,000733 | 0,000474 |
| $\omega = 1095\ rad/s$ | 0,000579 | 0,000677 | 0,000260 |
| $\omega = 1172\ rad/s$ | 0,000532 | 0,000683 | 0,000423 |
| $D_{wall} = 150\ mm$ | $r_{bent} = 5\ mm$ | $r_{bent} = 10\ mm$ | $r_{bent} = 13\ mm$ |
| $\omega = 904\ rad/s$ | 0,000313 | 0,000427 | 0,000262 |
| $\omega = 1095\ rad/s$ | 0,000262 | 0,000264 | 0,000484 |
| $\omega = 1172\ rad/s$ | 0,000286 | 0,000265 | 0,000332 |
| $D_{wall} = 200\ mm$ | $r_{bent} = 5\ mm$ | $r_{bent} = 10\ mm$ | $r_{bent} = 13\ mm$ |
| $\omega = 904\ rad/s$ | 0,000811 | 0,000484 | 0,000166 |
| $\omega = 1095\ rad/s$ | 0,001042 | 0,000332 | 0,000267 |
| $\omega = 1172\ rad/s$ | 0,000396 | 0,000265 | 0,000230 |

Table 2: Standard deviation of the bubble diameters (m)

## .3 Drafts of the new MBG

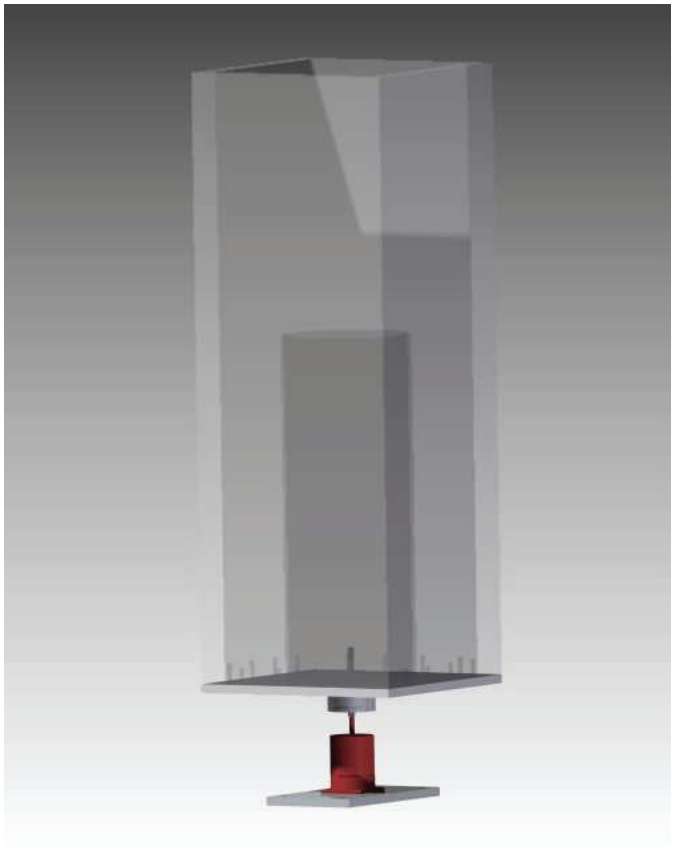

Figure 23: Drafts: Global view.

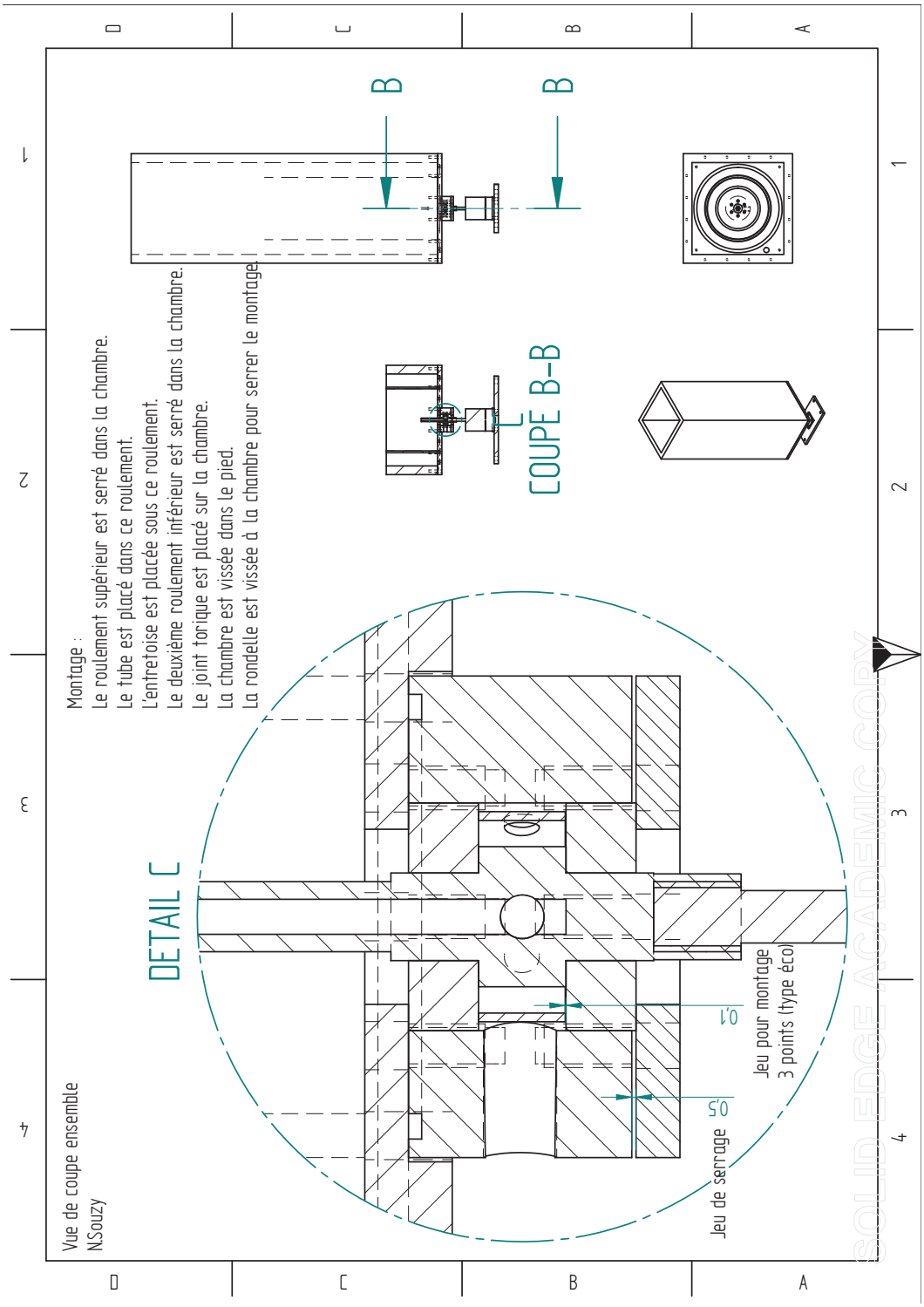


Figure 24: Drafts: Sectional view.

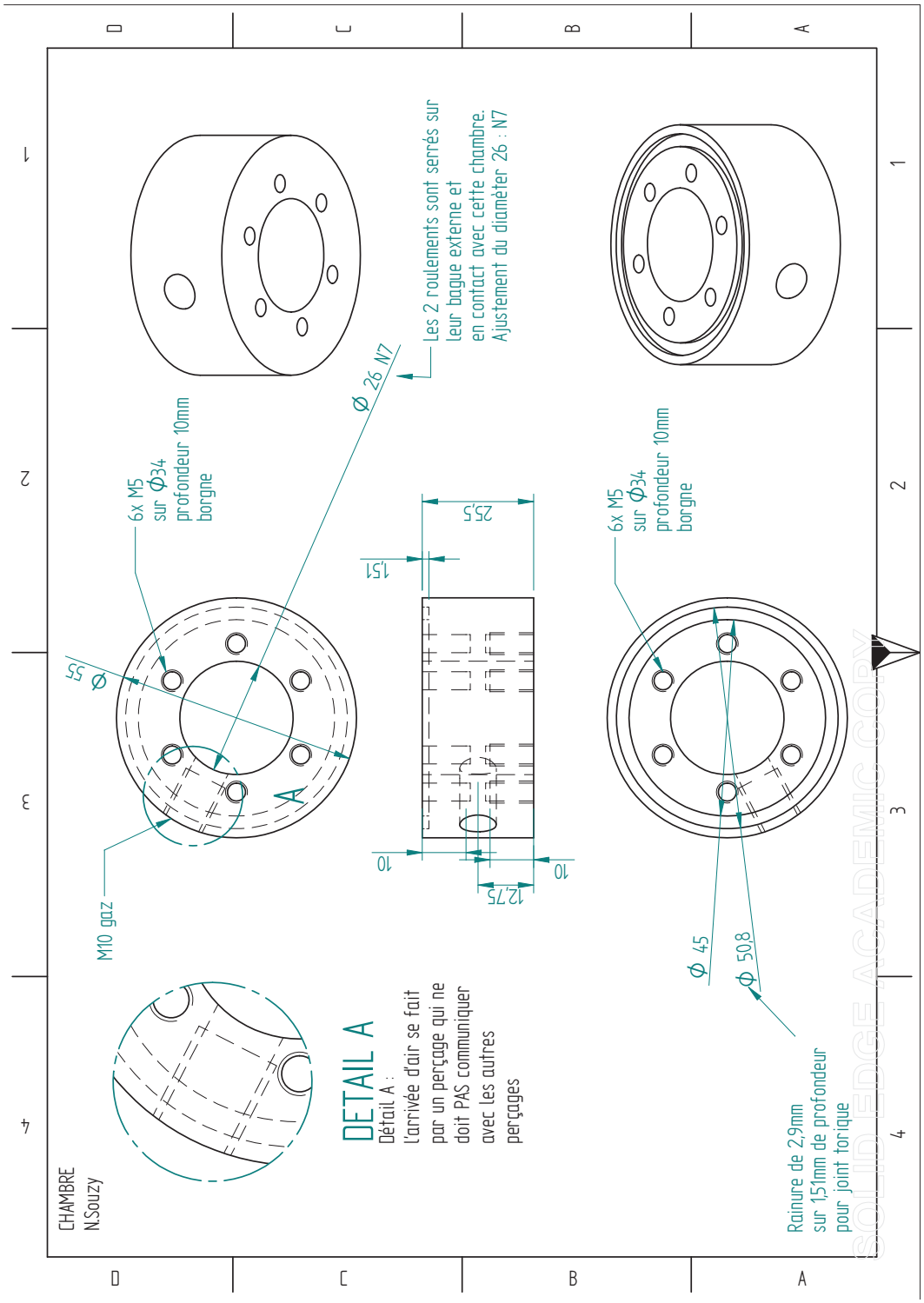


Figure 25: Drafts: Chamber.

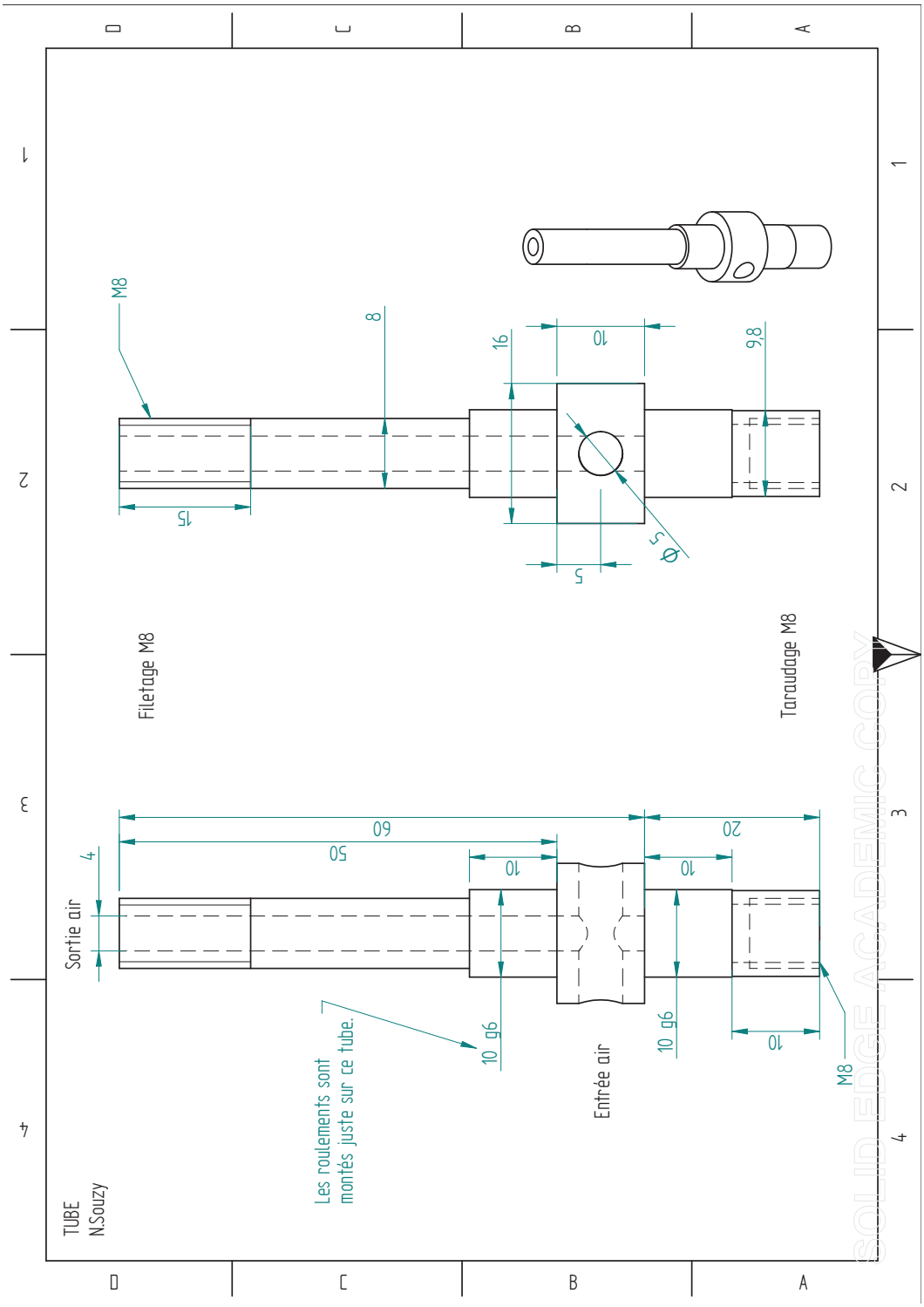


Figure 26: Drafts: Tube.

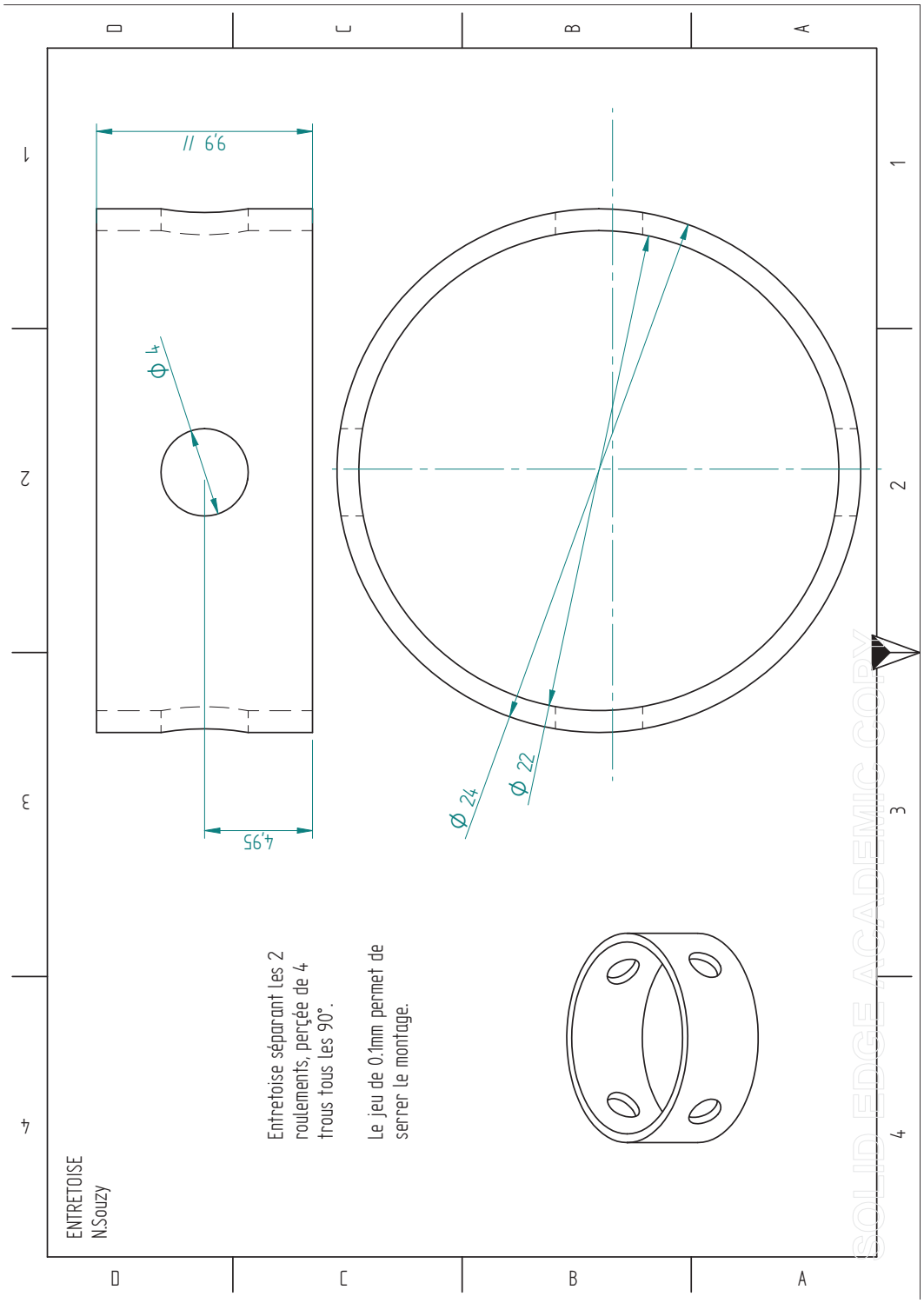


Figure 27: Drafts: Brace.

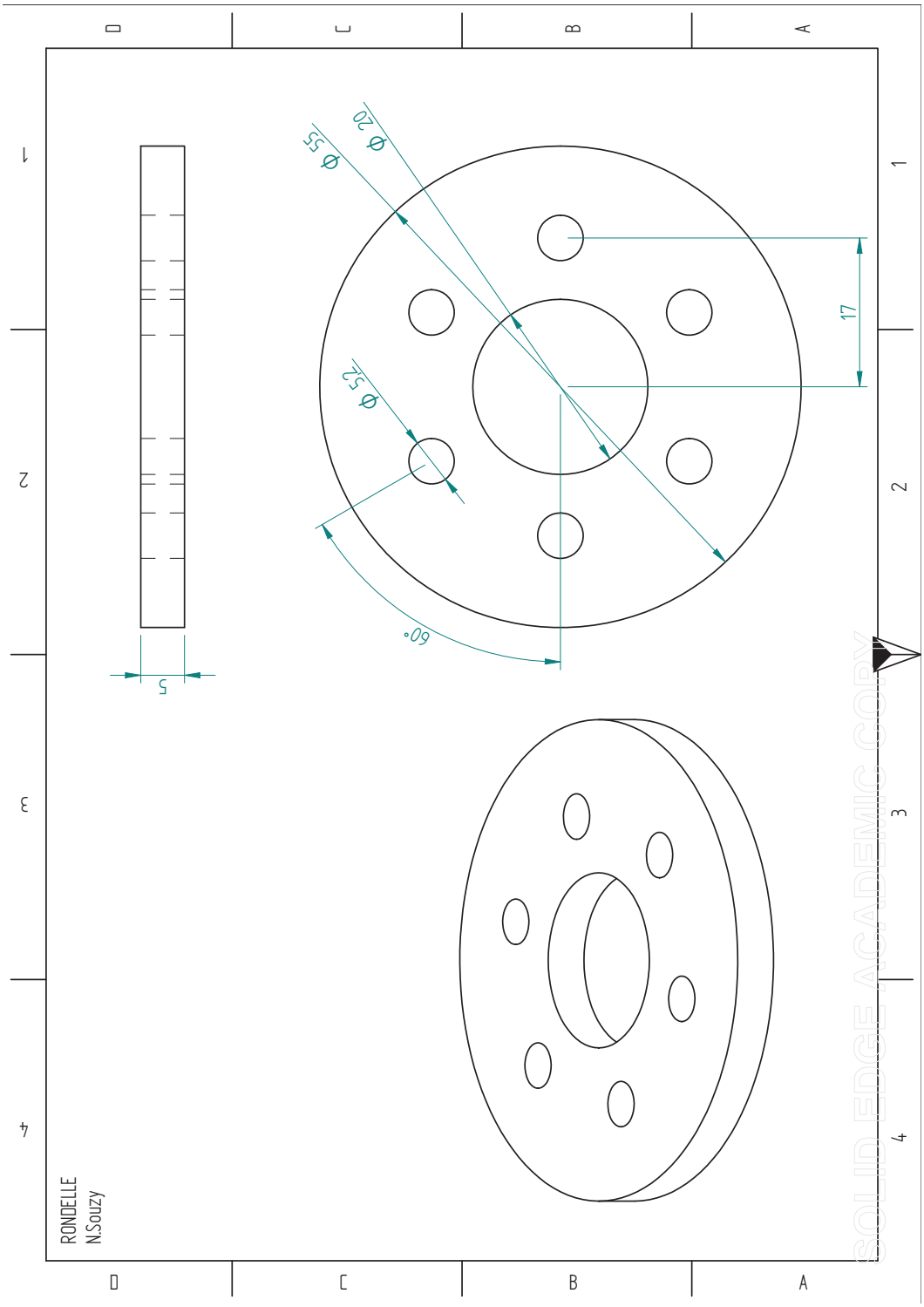


Figure 28: Drafts: Slice.

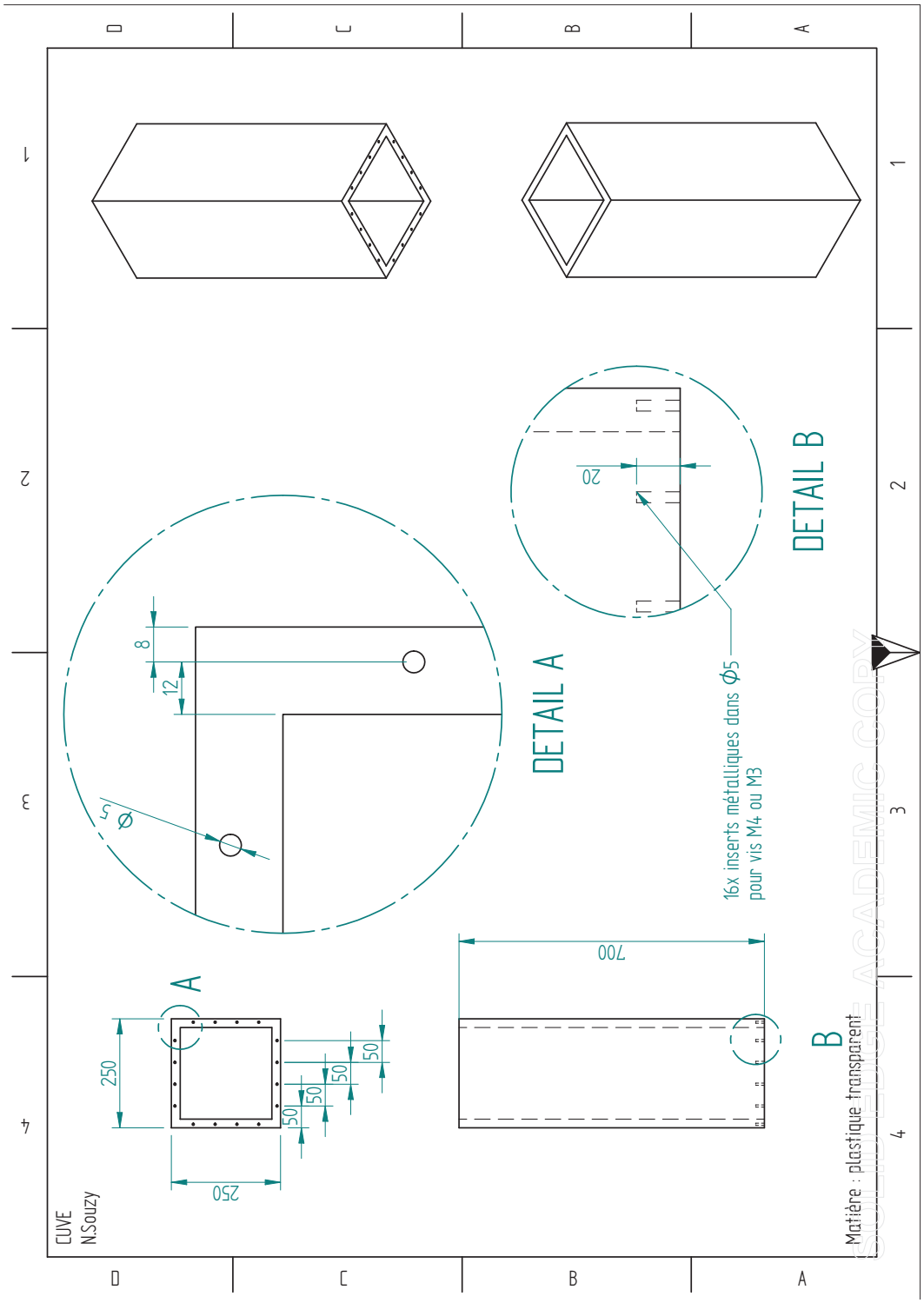


Figure 29: Drafts: Tank.

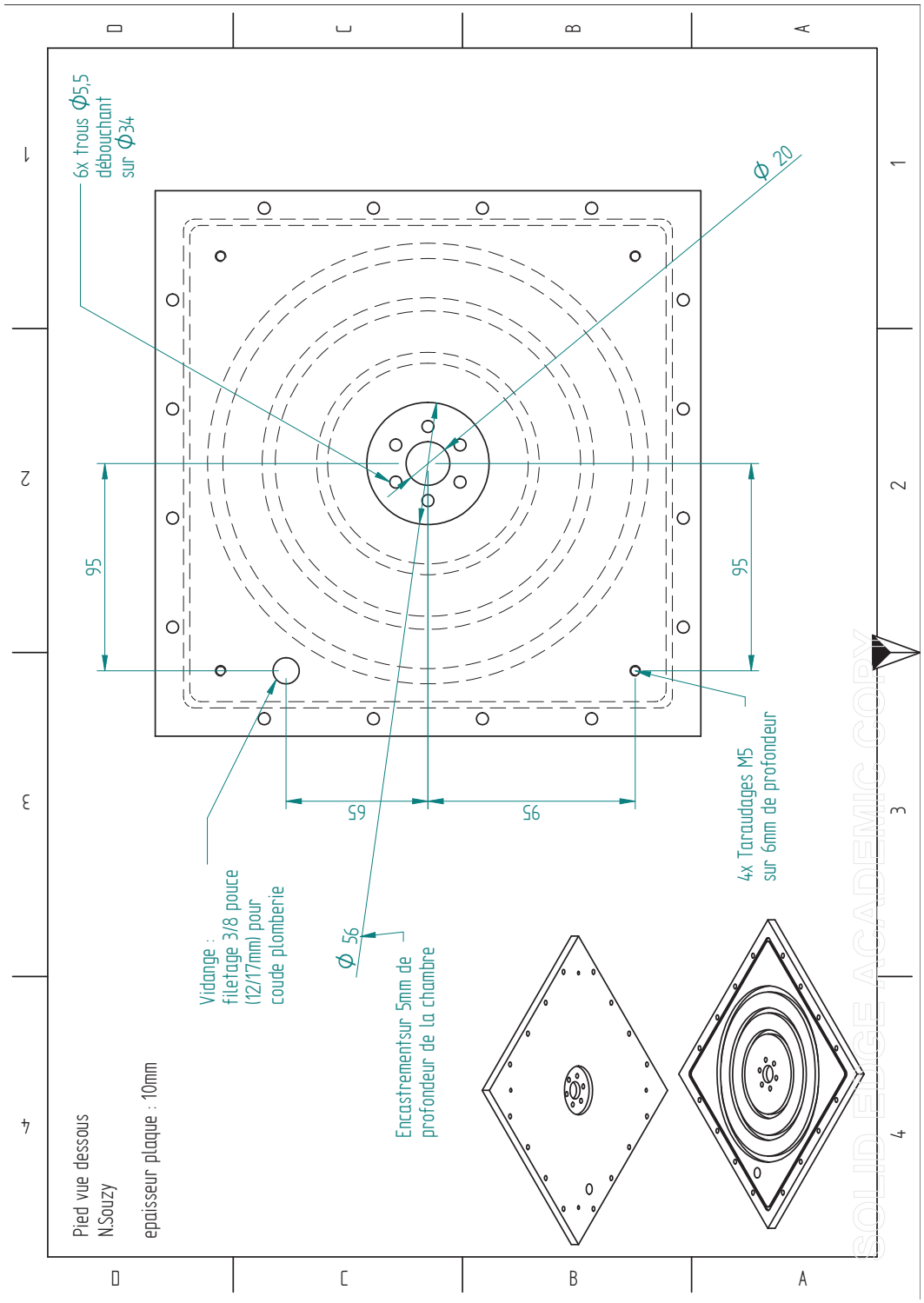


Figure 30: Drafts: Base, downward view.

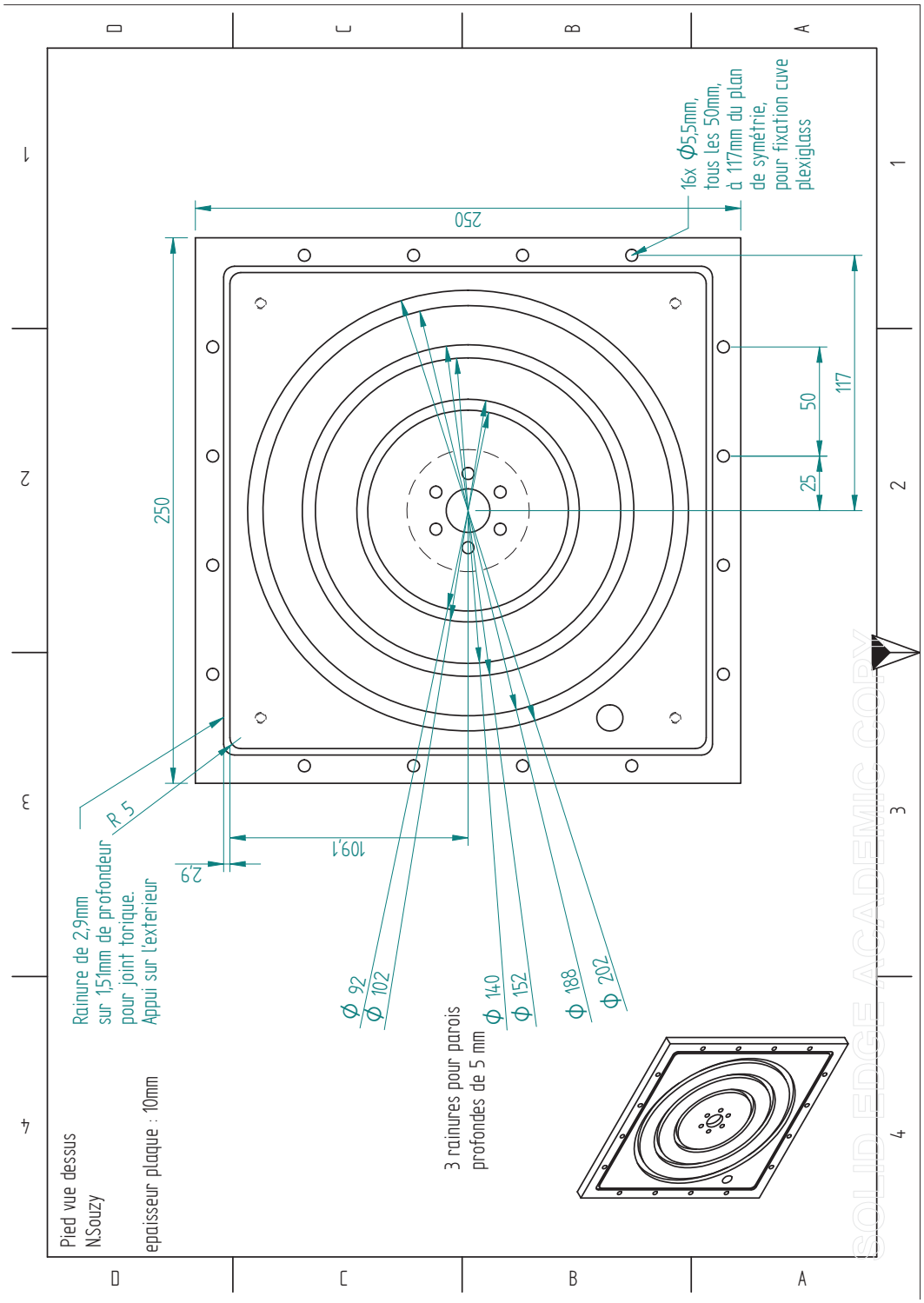


Figure 31: Drafts: Base, upward view.